Talmi, Y. and R.W. Simpson, 1980, Appl. Opt. **19**, 1401.
Timothy, J.G., 1981, Rev. Sci. Instrum. **52**, 1131.
Timothy, J.G. and R.L. Bybee, 1977, Rev. Sci. Instrum. **48**, 292.
Timothy, J.G. and R.L. Bybee, 1978, Rev. Sci. Instrum. **49**, 1192.
Timothy, J.G., G.H. Mount and R.L. Bybee, 1979, SPIE Space Opt. **183**, 169.
Tomboulian, D.H., 1965, NASA Goddard Space Flight Center (Greenbelt, MD) Technical Note **D-2917**.
Van Hoosier, M.E., J.-D.F. Bartoe, G.E. Brueckner, N.P. Patterson and R. Tousey, 1977, Appl. Opt. **16**, 887.
Walton, J.T., G.S. Hubbard, E.E. Haller and H.A. Sommer, 1979, IEEE Trans. Nucl. Sci. vol. NS-26, No. **1**, 335.
Wiza, J.L., 1979, Nucl. Instrum. Methods, **162**, 587.
Young, A.T., 1974, Methods Exp. Phys. **12A**, ed., N.P. Carleton (Academic Press, New York).

CHAPTER 6

TRANSPORT, DISPERSION AND DETECTION OF ELECTRONS, IONS AND NEUTRALS

E.H.A. GRANNEMAN and M.J. VAN DER WIEL
FOM-Institute for Atomic and Molecular Physics, Kruislaan 407, 1098 SJ Amsterdam, The Netherlands

Contents

Contents continued overleaf

Handbook on Synchrotron Radiation, Vol. 1, edited by E.E. Koch

Contents continued

1. Introduction

In a large fraction of the experiments using synchrotron radiation, especially those in the fields of atomic, molecular and surface physics, the interaction between matter and radiation is studied by investigating the creation of charged and neutral particles. Parameters such as the energy of the particle, its charge state, mass and the direction in which it is emitted with respect to target and light beam orientation give specific information on the underlying physical processes. Therefore in many cases the major part of the experimental effort is concentrated on the measurement of some or all of the above mentioned parameters.

This chapter gives guidelines for the design of the apparatus used in such experiments; it treats practical lens systems for efficient transport of particles, analysers for energy, mass and momentum and detectors for charged and neutral particles. The purpose of this chapter is to provide the reader with sufficient information and basic understanding to enable him to make a "first order" design of a complete system suitable for his experiment. Therefore all (sub)sections start with a qualitative explanation of the operation of the various devices and systems after which a number of useful formulae and tables are given on the basis of which a choice can be made between alternative possibilities. Besides that, practical information is given on matters such as energy and transmission calibration of systems, the choice of materials and the shielding of stray magnetic fields. Most (sub)sections are concluded with a short list of references in which more detailed information on the particular components can be found. These lists are by no means complete. For more complete lists of references the reader is referred to review papers mentioned in the beginning of the sections.

Because the ion (electron) optical properties of lenses and analysers are better understood with some knowledge on phase space theory we start with a short section on Liouville's theorem (sect. 2). Throughout the chapter relativistic and space charge effects are ignored.

Section 3 deals with particle transport in lens systems. Because during the last few years much tabular information on lens parameters has become available, we pay relatively much attention to the use of these tables for the design of practical lens systems.

Section 4 treats some ten different types of the most commonly used energy (mass, momentum) analysers. For other, less commonly used types the reader is referred to a number of review papers mentioned in the beginning of that section.

Detectors for charged and neutral particles are treated in sect. 5. Special attention is paid to multichannel detection techniques.

Owing to the fact that synchrotron radiation in general is elliptically polarized, in a large number of photoemission processes spin-polarized electrons are emitted; therefore a discussion on the transport and analysis of spin-polarized electrons is in order (sect. 6).

When one not only measures the rate at which a certain type of particle is produced, but also its time correlation with another particle produced in the same photon impact process, more detailed information on the physical process can be obtained. Therefore a description of coincidence techniques in general and the arrangement of coincidence detection systems are presented in sect. 7.

2. Liouville's theorem

The position and velocity of a particle travelling through space is fully characterized by one point in the so-called phase space, first introduced by Liouville (1838). This phase space is a six-dimensional space, three coordinates giving the position of the particle; the remaining three the velocity, or better, the momentum. An ensemble of particles in this way gives rise to a cloud of points in this phase space. For such an ensemble we can state the following: the trajectory of each of the particles in real space as well as in phase space is fully known once the original positions in phase space and the nature of the forces acting on the particles are known. Now Liouville's theorem states that the density of points in phase space remains constant under the action of conservative forces. A force is conservative if the total work done on the particle only depends on its initial and final positions; i.e., all forces on charged particles due to stationary electric and magnetic fields are conservative. For the remainder of this chapter we will limit ourselves to stationary fields.

If we concentrate on beam-like ensembles then, depending on the symmetry, the number of relevent coordinates in phase space usually decreases. For cylindrical and for rectangular symmetry the beam can be characterized by one (r, p_r) and by two independent (x, p_x) and (y, p_y) two-dimensional subspaces, respectively. For each of these three subspaces Liouville's theorem holds independently, i.e., if for instance for cylindrical symmetry at a certain moment in time or for a given z position all particles of a beam are contained within a certain area in the (r, p_r) phase space, this area will remain constant for the forces mentioned above.

Frequently we are not directly interested in the position and momentum (r, p_r) of the particle but more in the particle trajectory, i.e., the position and direction coordinates (r, α_r) where α_r is defined as $\alpha_r = \arctan(p_r/p_z)$. The area taken by the beam particles in the (r, α_r) space is not constant however; one can prove that it increases inversely proportional to the square root of the energy of the particles. This can be seen easily: if for instance one accelerates the particle in the z-direction to a higher energy, the radial momentum p_r remains the same; however, the axial momentum p_z increases and consequently α_r decreases. The area in the (r, α_r) space multiplied by the square root of the energy (divided by a factor π) is called the emittance (normalized emittance). This quantity is an invariant of the beam. If the number of particles emitted per unit source area and unit solid angle is constant then the phase space diagram is a parallellogram with a homogeneous density of phase space points. In actual beam physics the phase figure often is an ellipse, see sect. 3.2.3 and Wollnik (1976). We will now give a few examples of how this theorem can be used.

Assume an object at position O is imaged at position I by means of a lens, see fig. 1. In sect. 3 we will go into how a lens works and what it looks like. All particles leaving the object (length l_0) within an opening angle α_0 are focussed at the image (length l_i) within an angle α_i. If the energies of the particles at the object and image are E_0 and E_i, respectively, the before-mentioned invariance of the emittance leads to:

$$l_0 \alpha_0 E_0^{1/2} = l_i \alpha_i E_i^{1/2} . \tag{1}$$

In this we have assumed implicitly that $\tan\alpha \approx \alpha$. This form of Liouville's theorem is also known as Lagrange's law. Note that this law does not involve the average angle θ_B of the particle trajectories with the optical axis. Also this angle θ_B is sometimes rather confusingly called the opening angle of the beam. To avoid possible confusion we shall call α_0 and α_i pencil angles and θ_B a beam angle. In fig. 1 the (r, α_r) phase space diagrams are given for various positions of the optical

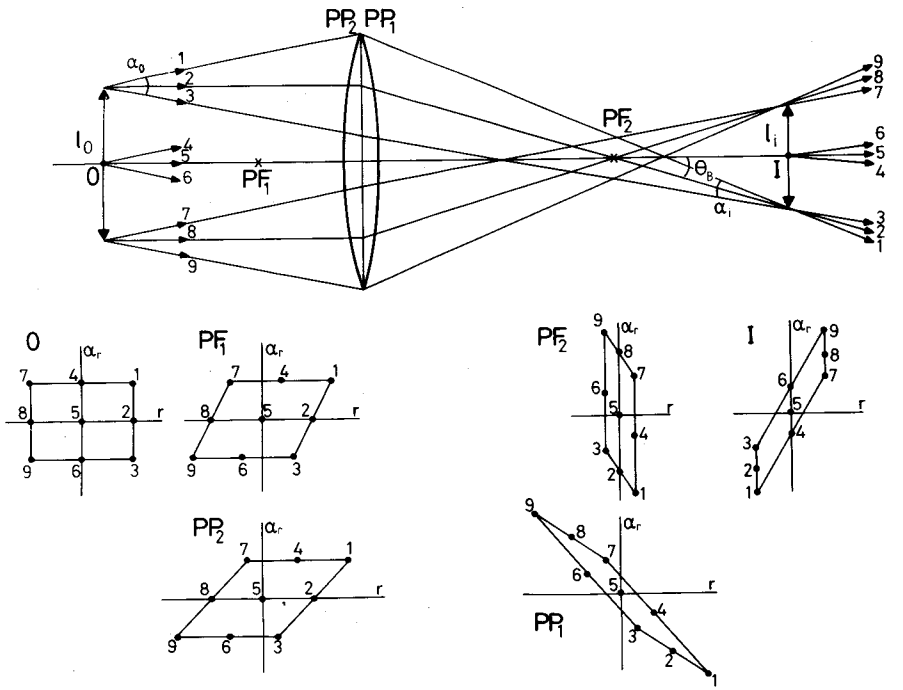

Fig. 1. A particle source (height l_0) at position O is imaged (height l_i) at position I by means of a lens. From every point of the source particles are emitted within a cone with opening angle α_0. The numbers 1–9 indicate characteristic particle trajectories. Phase space diagrams representing the radial coordinates (r) and the direction of propagation of the beam particles (α_r) are shown for various axial positions: the source and image planes, the focal planes PF_1 and PF_2 and the principal planes PP_1 and PP_2. The lens is accelerating and is assumed to be "thin", i.e., PP_1 and PP_2, generally located right and left of the lens symmetry plane, respectively, coincide (see sect. 3) θ_B is the so-called beam angle.

system. Because in the figure the energy E_i is assumed to be larger than E_0, the area in phase space at the image side of the lens is smaller than at the object side. Note that the beam angle is zero at the object position. By a suitable choice of lenses, this angle can always be made zero again. In that case the phase space

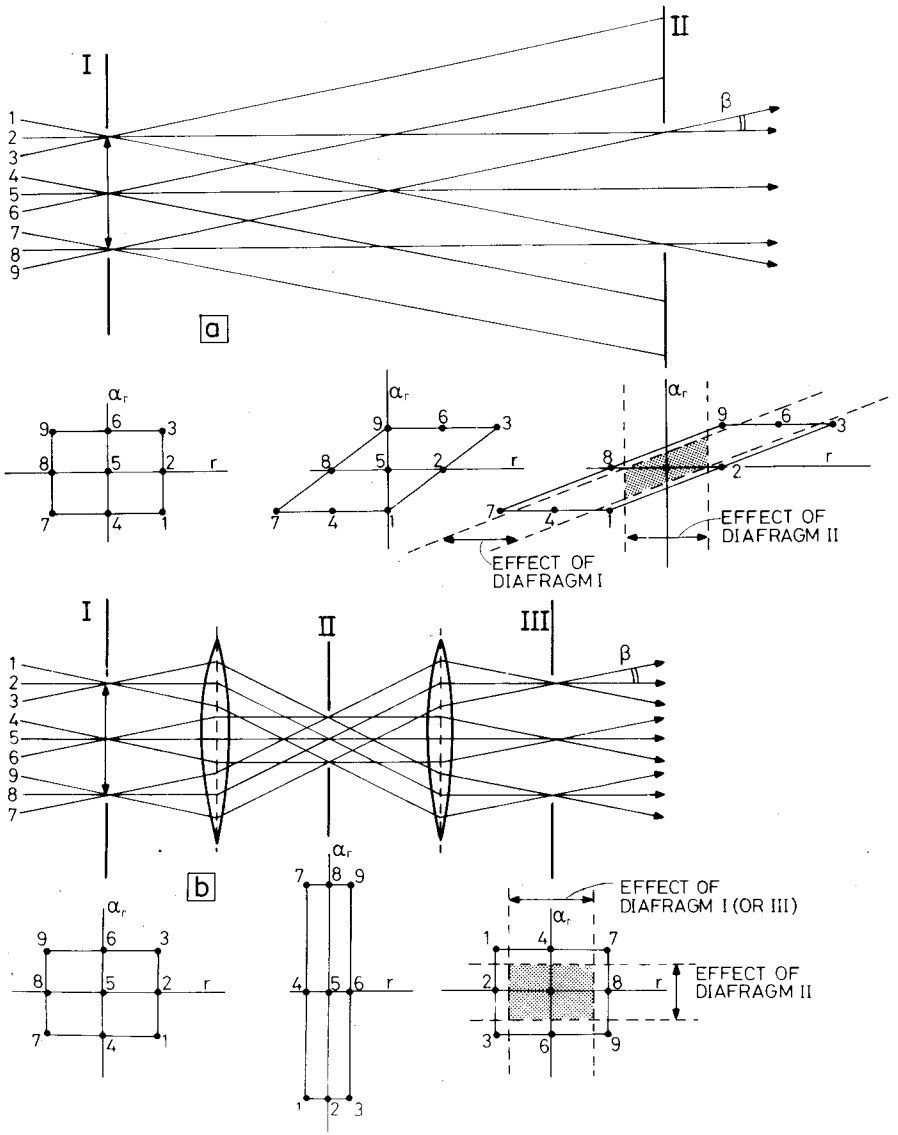

Fig. 2. Two possible ways of particle beam collimation by which a certain required opening angle (β) and beam size are obtained. (a) Collimation by means of two diaphragms placed at a suitably chosen distance from each other. (b) Collimation by means of a combination of diaphragms and lenses. The focal planes of the first lens coincide with the apertures I and II and those of the second with apertures II and III. A comparison of the two shaded areas directly shows that the second method of collimation is more efficient than the first one. (Under the general assumption that the number of particles per unit area is constant.)

diagram has a rectangular shape. For an optimal design it is essential to consider the phase space diagram at various points of an optical system; e.g., at the entrance of an energy analyser it is often preferable to reduce the beam angle to zero (sect. 4).

As a second illustration of this theorem we will discuss the collimation of beams (fig. 2). In some cases it is necessary to limit the emittance of the beam, i.e., either its divergence or its linear dimensions. Of course by a suitable choice of optics these two are interchangeable. In particular this can be done by placing a set of two diaphragms at a sufficiently large distance (fig. 2(a)). However, this method is not very efficient in the sense that more particles are cut away than is strictly necessary. A more elegant way is to make use of a set of two lenses of which the focal planes coincide (telescope). The source is placed in the focal plane of the first lens. It will be clear from the figure that a diaphragm at the common focal plane (position II in fig. 2(b)) controls the divergence of the beam without changing its diameter, while diaphragms at the source or at the position of the image of the source (positions I and III in fig. 2(b), respectively) control the diameter without affecting the divergence. As will be clear from the comparison of the areas of the two shaded phase space diagrams (fig. 2(a) and (b)) the method of collimation of fig. 2(b) is to be preferred above that of fig. 2(a).

Finally we will show how one can quickly estimate which fraction of the total number of particles produced in some physical process will be accepted by an arbitrary electron (ion) optical device, assuming ideal transport. Take for instance the following case: one is interested in determining the energy distribution of photoelectrons produced by a 1 mm diameter light beam impinging on a solid surface. Photoelectrons are assumed to be emitted isotropically over a solid angle of 0.5 sr* ($\alpha_0 \approx 45°$ in fig. 1) and their excess energy is about 1 eV. The energy analyser one wants to use has an acceptance solid angle of 0.03 sr ($\alpha \simeq 5°$) and an entrance aperture with diameter 1 mm. The electron energy in the analyser is 0.25 eV. In this case the emittance of the "beam" leaving the surface is equal to $0.125\,\pi$ (sr mm^2 eV) and the acceptance of the analyser is $1.875 \times 10^{-3}\,\pi$ (sr mm^2 eV). In the ideal situation where there is no degradation of beam quality during transport from surface to analyser, only 1.5% of the total number of electrons produced in the process is accepted.

3. Charged particle transport

3.1. Introduction

Between physical process and particle analysis/detection some form of particle transport is required. For this purpose electron (ion) lenses are used. An ideal lens is a device which exerts a force on a particle proportional to the distance r between the particle and the optical axis of the system. The optical axis or plane usually coincides with the symmetry axis (plane) of the lens. Consequently an

*sr stands for steradian.

ideal lens is capable of focussing all particles from a point source (or slit) at the entrance side of the lens into a point (slit) image at the exit side, independent of the initial angle of the particles with respect to the optical axis. Usually lenses are not ideal, i.e., the force is only linear with r in a limited region around the optical axis. Therefore particles leaving the source with large opening angles or more generally entering the lens at large r are imaged with aberrations.

In the following we shall first treat the general properties of lens systems in the paraxial approximation, i.e., the excursions of the particle trajectories with respect to the optical axis are assumed to be small enough to make aberrations negligible (sect. 3.2). In sect. 3.3 various types of one- and two-dimensional lenses will be treated. Section 3.4 deals with aberrations and in sect. 3.5 some practical lens systems are discussed. For the choice of materials we refer to sect. 4.8. Note that to a large extent the general properties of lenses mentioned in these sections also apply to the dispersive elements (sect. 4).

3.2. *Lenses, paraxial approximation*

3.2.1. *Characteristic lens parameters and ray tracing*

Although the following is probably familiar to most readers we briefly go through the basic ideas of lens parameters and ray tracing.

The focussing properties of lenses and dispersive elements can be characterized by a set of four numbers, two focal and two principal lengths, defining four points on the optical axis. The planes through these points, perpendicular to the optical axis are called the focal and principal planes, respectively. Knowledge of these four points (planes) suffices to trace the asymptotic trajectory of a particle once its initial position and angle with respect to the optical axis are known. In fig. 3(a) the focal points and principal planes (PF_1, PF_2 and PP_1, PP_2, respectively) are shown. Note that the definitions of focal and principal distances are only meaningful in the paraxial limit.

The asymptotic trajectories of particles entering and leaving the lens can be found as follows;

(a) A particle entering the lens at the object side, going through the focal point PF_1 is assumed to follow an asymptotic straight line trajectory up to the principal plane PP_1 where this trajectory is refracted such that it leaves the lens parallel to the optical axis (fig. 3(a)).

(b) A particle entering the lens parallel to the optical axis is assumed to follow an asymptotic straight line trajectory up to the principal plane PP_2, where this trajectory will be refracted such that it leaves the lens through the image side focal point PF_2 (fig. 3(a)).

(c) Trajectories, parallel at the entrance side, cross each other in the same point of the focal plane (PF_2-plane).

(d) In passing from one principal plane to the other there is unit linear magnification.

The first two rules permit one to locate the position and size of the image (fig. 3(a)) while the third rule enables one to trace an arbitrary particle trajectory

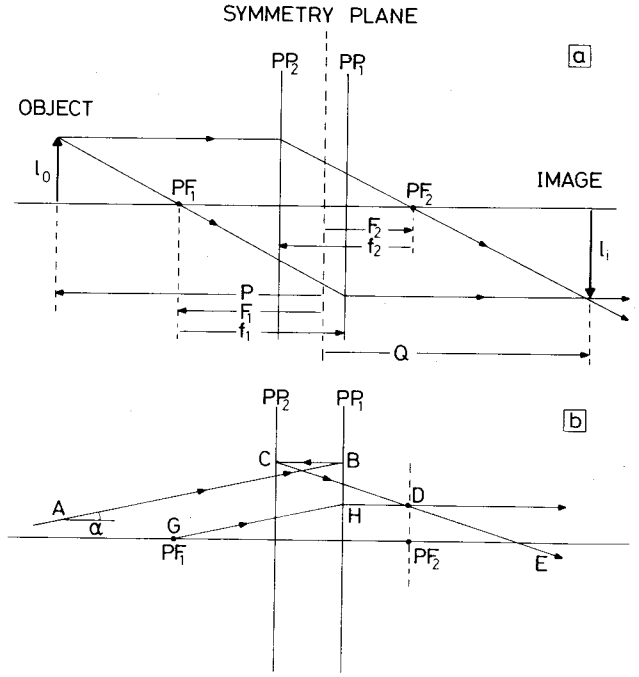

Fig. 3. Characterization of a lens by means of focal and principal planes. The axial position of the focal planes (points) PF_1 and PF_2 and the principal planes PP_1 and PP_2 is determined by the magnitude and the sign of F_1, F_2, f_1 and f_2. F_1 and F_2, and the object and image distances P and Q are defined with respect to the symmetry plane; the focal lengths f_1 and f_2 with respect to PF_1 and PF_2, respectively. The arrows define directions corresponding with positive numbers P, Q, $F_{1,2}$ and $f_{1,2}$. With this convention a positive lens – i.e., the lens most frequently encountered in charged particle transport – has positive values for all four numbers $F_{1,2}$ and $f_{1,2}$ (see also fig. 12). (a) Two characteristic asymptotic trajectories; one entering the lens parallel to the axis and one going through the object focal point. (b) Tracing of an arbitrary ray (starting at A). The actual trajectory coincides only at asymptotic distances.

asymptotically; see fig. 3(b), trajectory going through point A at an angle α with the optical axis. The asymptotically straight line trajectory is continued up to point B where it crosses the principal plane PP_1. A horizontal line BC provides point C on the principal plane PP_2 from which the outgoing trajectory starts. The asymptotic trajectory CDE of the particle leaving the lens can be found realizing that it should cross the focal plane located at PF_2 at the same point D as the ray GH entering the lens parallel to AB going through focal point PF_1 (rules b and c).

From the schematic picture of fig. 3(a) the following relations between object and image distances P and Q, respectively can be deduced:

$$(P - F_1)(Q - F_2) = f_1 f_2 \,. \tag{2}$$

This relation is Newton's formula for "thick" lenses. It can be seen easily that the

choice of the symmetry plane is arbitrary, only the position of the two focal points PF_1 and PF_2 and the two focal lengths f_1 and f_2 matter. For lenses with coinciding principal planes ("thin" lenses) and for which $f_1 = f_2$, relation (2) simplifies to the well-known result:

$$\frac{1}{P}+\frac{1}{Q}=\frac{1}{f}. \tag{3}$$

For the linear magnification $M_L = l_i/l_0$ we can write:

$$M_L = \frac{-f_1}{P-F_1} = \frac{Q-F_2}{-f_2}. \tag{4}$$

From relation (1) it can be seen that the angular magnification $M_A = \alpha_i/\alpha_0$ (fig. 1) and M_L are coupled according to:

$$M_L M_A = \sqrt{E_0/E_i} = f_1/f_2\,. \tag{5}$$

In case more lenses are used in series it is possible to consider the series as one new lens, again characterized by two focal points (planes) and two principal planes. For instance for a lens set C consisting of two lenses A and B with a distance D between the two symmetry planes we can write:

$$(P-F_1^C)(Q-F_2^C) = f_1^C f_2^C \tag{6}$$

in which:

$$\begin{aligned} &f_1^C = f_1^A f_1^B/D', \qquad f_2^C = f_2^A f_2^B/D', \\ &F_1^C = F_1^A + \tfrac{1}{2}D - f_1^A f_2^A/D', \qquad F_2^C = F_2^B + \tfrac{1}{2}D - f_1^B f_2^B/D'. \end{aligned} \tag{7}$$

where $D' = (F_1^B + F_2^A - D)$. In eqs. (6) and (7) P, Q, F_1^C and F_2^C are (arbitrarily) defined with respect to a new symmetry plane located helfway between the symmetry planes of the lenses A and B. In case $D' = 0$, then $F_{1,2}^C$ and $f_{1,2}^C$ go to infinity; a system which is called telescopic. Examples of such a lens system are the Heddle-type lens (sect. 3.5) and analysers in which the entrance and exit slits are located at the boundaries of the deflecting fields (sect. 4.2).

3.2.2. *Matrix formulation*

In cases where the lens system consists of one or two lenses, the quickest way to get insight in the properties of the system is to trace a few characteristic rays through the system graphically or to use eqs. (2)–(7). However if the system consists of more than two or three lenses these methods very soon become laborious. In that case it is often more convenient to calculate the lens properties by means of the so-called transfer matrices (Banford 1966, Hawkes 1970, Di Chio et al. 1974).

A transfer matrix relates the position and slope of a ray at some plane ($z = z_1$) to its position and slope in another plane ($z = z_2$). Again limiting ourselves to asymptotic trajectories in the paraxial approximation, we can generally state:

$$\begin{pmatrix} r_2 \\ r_2' \end{pmatrix} = \begin{pmatrix} A & B \\ C & D \end{pmatrix}\begin{pmatrix} r_1 \\ r_1' \end{pmatrix}, \tag{8}$$

where r_1, r_1' and r_2, r_2' denote positions and slopes of a ray at the planes $z = z_1$ and $z = z_2$, respectively. For the moment we will only consider axial symmetric systems. If we consider for instance a trajectory in a field-free space (see fig. 4), it is easy to see that:

$$\begin{pmatrix} r_2 \\ r_2' \end{pmatrix} = \begin{pmatrix} 1 & (z_2 - z_1) \\ 0 & 1 \end{pmatrix}\begin{pmatrix} r_1 \\ r_1' \end{pmatrix}. \tag{9}$$

For the matrix relating the position and slope of a ray at two sides of a lens we can write (fig. 5):

$$\begin{pmatrix} r_2 \\ r_2' \end{pmatrix} = \begin{pmatrix} -\dfrac{(z_2 - z_{PF_2})}{f_2} & \dfrac{(z_2 - z_{PF_2})(z_1 - z_{PF1})}{f_2} + f_1 \\ -\dfrac{1}{f_2} & \dfrac{(z_1 - z_{PF_1})}{f_2} \end{pmatrix}\begin{pmatrix} r_1 \\ r_1' \end{pmatrix}. \tag{10}$$

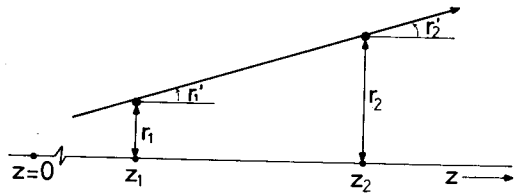

Fig. 4. The trajectory of a particle in field-free space. The radial coordinate and direction of propagation at the axial positions z_1 and z_2 are denoted by (r_1, r_1') and (r_2, r_2'), respectively $(r_1' = r_2')$.

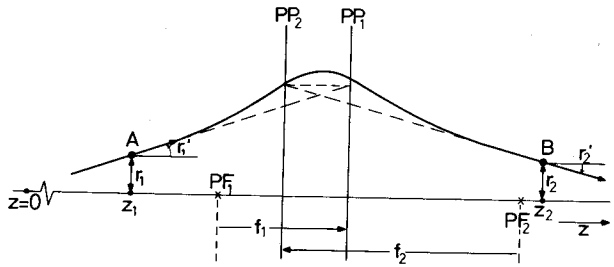

Fig. 5. The asymptotic trajectory (dashed line) of a particle passing a lens. (r_1, r_1') and (r_2, r_2') give the radial coordinates and directions of propagation at the axial coordinates z_1 and z_2, respectively. Note that z_1 and z_2 are not necessarily object and/or image positions. The solid line shows a more realistic trajectory.

Several special cases for z_1 and z_2 can be considered:
$-z_1$ and z_2 coincide with the object image focal planes respectively; in that case:

$$\begin{pmatrix} A & B \\ C & D \end{pmatrix} = \begin{pmatrix} 0 & f_1 \\ -1/f_2 & 0 \end{pmatrix}, \tag{11}$$

$-z_1$ and z_2 coincide with the principal planes PF_1 and PF_2, then:

$$\begin{pmatrix} A & B \\ C & D \end{pmatrix} = \begin{pmatrix} 1 & 0 \\ -1/f_2 & f_1/f_2 \end{pmatrix}, \tag{12}$$

$-z_1$ and z_2 coincide with the object and image plane, then:

$$\begin{pmatrix} A & B \\ C & D \end{pmatrix} = \begin{pmatrix} M_L & 0 \\ -1/f_2 & f_1/f_2 M_L \end{pmatrix}, \tag{13}$$

in which M_L is the linear magnification (4).

The transfer from z_1 to z_2 can now be considered as being composed of a drift from z_1 to PF_1, a transfer from object to image focal plane and a drift from PF_2 to z_2; i.e.:

$$\begin{pmatrix} r_2 \\ r_2' \end{pmatrix} = \begin{pmatrix} 1 & (z_2 - z_{PF_2}) \\ 0 & 1 \end{pmatrix} \begin{pmatrix} 0 & f_1 \\ -1/f_2 & 0 \end{pmatrix} \begin{pmatrix} 1 & (z_{PF_1} - z_1) \\ 0 & 1 \end{pmatrix} \begin{pmatrix} r_1 \\ r_1' \end{pmatrix}. \tag{14}$$

Of course eq. (14) is equivalent to eq. (10). This method is advantageous in case systems containing many lenses have to be treated. Note that the determinant of each matrix is equal to one if no acceleration or deceleration takes place and equal to $f_1/f_2 = \sqrt{E_1/E_2}$ if acceleration or deceleration from E_1 to E_2 occurs.

In the way sketched above it is possible to compute the transfer of rays through lens systems of arbitrary complexity.

3.2.3. Waist-to-waist transfer

So far we have been dealing with the imaging of particle sources and/or other objects. However, usually one is not interested in the exact image but in a suitable (small) object for a next optical element such as for instance an energy analyser (sect. 4). In fig. 1, for instance the smallest beam size, called the beam waist, is not located at the image, but at the focal plane. Such a beam waist can equally well serve as an object for the next optical element. Especially in the case depicted in fig. 2(b), the beam waist in between the two lenses would be a good new object: it has zero beam angle. Now it is possible to make an image of this waist "object", i.e., to proceed in the usual way of object-to-image transfer (conjugate point focussing; eqs. (2)–(7)). However, in some cases it may be advantageous to (also) consider waist-to-waist transfer. In the case of the rectangular phase space diagrams this can easily be done graphically. In the general situation shown in fig. 1, where from each point of a source particles are emitted within a certain pencil angle, a lens produces a (new) waist, which, depending on the size of the source and the pencil angle is either located at the focal plane or coincides with the image. In case of elliptically shaped phase space diagrams (sect. 1) the situation is more complicated. Because this mainly concerns long beam transport lines we limit ourselves to a number of references. Banford (1966), Galeys and Rose (1967), Silbar (1970) and Luccio (1970) treated waist-to-waist transfer in the thin lens approximation, while Glavish (1972) derived formulae describing the same for thick lenses.

3.3. Practical types of lenses

In the past decades various types of magnetic and electrostatic lenses have proved their usefulness for efficient transport of charged particles (Grivet 1965, Klemperer and Barnett 1953, Septier 1967, Banford 1966, Mulvey and Wallington 1973, Liebl 1978). The principal difference between magnetic and electrostatic lenses is that the forces exerted by magnetic fields depends on the particle momentum (mv) while the influence of electrostatic fields on particle trajectories depends on the particle energy ($\frac{1}{2}mv^2$).

Nowadays for most low energy applications electrostatic lenses are used because this type of lens usually is relatively small and uses no energy (no cooling); it does not contain bulky (magnetic) materials and/or coils; besides that, electric stray fields are more easily screened than magnetic stray fields.

However there are specific circumstances where magnetic lenses are the better choice. This is especially the case when light particles (electrons) with high energies have to be transported. Electrostatic lenses requiring electric fields of 50–100 kV/cm are not practical in view of the high-voltage break-down problems. Because synchrotron radiation experiments usually do not involve these high energy particles we will concentrate on electrostatic lenses. Readers interested in magnetic lenses are referred to Fert and Durandeau (1967), Glaser (1952) and Hawkes (1967).

In the following, two classes of lenses will be considered; the so-called weak and strong lenses. Cylinder lenses and aperture (slit) lenses are weak lenses while quadrupole lenses belong to the class of strong lenses.

It should be noted that whenever potentials on lens elements are mentioned, these are referred to a potential at which the particles would have zero energy, i.e., in most cases the source potential.

3.3.1. Weak lenses

(a) *Cylinder lenses.* In fig. 6 a cylinder lens consisting of a combination of two cylinders at different potentials is shown. The shape of the electric field near the gap is such that a charged particle entering the lens feels a force directed radially inwards at the entrance side of the lens and a force radially outwards at the exit side of the lens (or vice versa, depending on the charge state of the particle and the polarity of the potentials on the cylinder elements). However, due to the fact

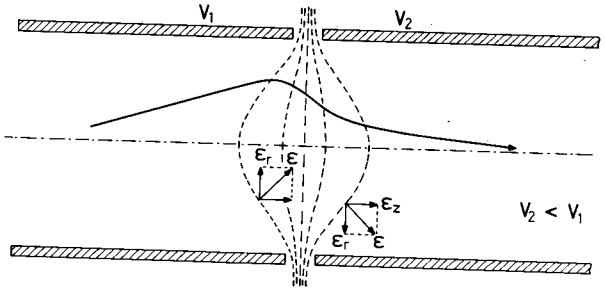

Fig. 6. The principle of operation of a cylinder lens. The dashed lines indicate equipotential lines. The electric field ε present in the vicinity of the gap between the two cylinders has a radial component ε_r directed inwards on entering and outwards on leaving. Since the particle enters the system at a large radius and leaves it at a smaller one the overall effect is a bending of the trajectory towards the optical axis.

that the radial field at a large radius on entering is larger than the radial field at a smaller radius on leaving, the net effect is a bending of the trajectories towards the axis. This is shown in fig. 6. Because this effect is stronger for trajectories initially further away from the axis, the system acts as a lens. Various combinations of cylinders are possible, see fig. 7. All characteristic lens parameters scale with the diameter D of the lens and therefore they are usually expressed in units of length D. Beyond a distance D from the gap the field is practically zero and consequently a new optical element can be placed at that distance from the gap without disturbing the lens. This means that a three-element cylinder lens like the one in fig. 7(b), can be considered as two two-element lenses provided the central cylinder has a length equal to or larger than $2D$.

As for the nomenclature: a lens is called an "immersion" lens if particles are accelerated or decelerated (figs. 7(a,c) and 7(b,d) if $V_3 \neq V_1$). A three-element lens is called an "einzel" lens if $V_3 = V_1$. A "unipotential" lens is a three-element lens of which the central element is at the particle source potential.

The characteristic parameters of the most important types of lenses have been calculated with high precision; the position of focal and principal planes are usually given with an accuracy better than 1%. Extensive tables describing cylinder lenses of various dimensions (fig. 7) have been given by Harting and Read (1976). This book should be on the shelf of every designer of electron (ion) lens systems. Harting and Read treat two-element lenses with various gap widths,

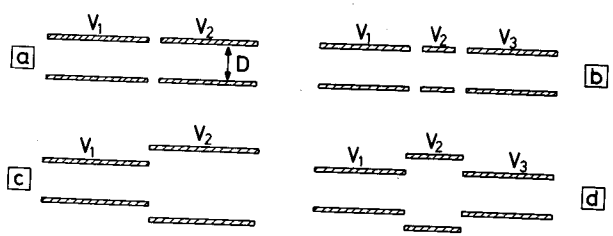

Fig. 7. Cylinder lenses consisting of two and three elements with equal diameters D, (a), and (b), and unequal diameters, (c) and (d). V_1, V_2 and V_3 denote potentials applied at the cylinder elements.

and voltage ratios V_2/V_1 between 1.2 and 90; three-element lenses with a length of the central element equal to D and $0.5\,D$ and V_3/V_1 varying between 1.0 and 30. For each of these combinations the position of the image is given for varying object position (the so-called P–Q curves; for P and Q, see (fig. 3). Also the aberration coefficients (sect. 3.4) are tabulated for each of the combinations. Harting and Read also treat lens systems made up of rectangular tubes with a large height/width ratio. This may be considered as the one-dimensional analogue of the cylinder lens, i.e., it gives one-dimensional focussing. Similar tabulated information can be found in Read et al. (1970), Adams and Read (1972a,b), Natali et al. (1972), Kuyatt et al. (1972). Three-element unipotential lenses are treated by El-Kareh and Sturans (1971a,b). Di Chio et al. (1974) give tabulated lens parameters and P–Q curves for large voltage ratio two-element cylinder lenses (up to $V_2/V_1 = 10^4$).

(b) *Aperture (slit) lenses.* A second type of electric field configuration capable of focussing charged particles is that due to a set of two parallel plates with apertures, held at different potentials, see fig. 8(a). In this case the unit dimension is the aperture diameter A. The space before the first and behind the second plate is assumed to be field-free. Also in this case three or more elements can be employed (see fig. 8(b)) with possibly different aperture diameters and distances between the plates. The properties of these lens systems are comparable with those of the cylinder lenses. The one-dimensional analogue of the aperture lens is the slit lens (height much larger than width). Harting and Read (1976) have tabulated the positions of focal and principal planes for two-element aperture and slit lenses for voltage ratios V_2/V_1 between 1.2 and 90 and for three-element lenses with V_3/V_1 between 1.0 and 30. Also P–Q curves and aberration coefficients are given. Similar information can be found in Read (1969a,b) and Read (1970).

A special type of aperture lens is the so-called Calbick lens (Klemperer 1953). One can prove that a plate containing an aperture separating two regions in space with different electric field strengths acts like a lens (see fig. 9(a)). If E_0 is the energy of the particle ($V_0 = E_0/q$ is the potential on the plate with respect to the particle source, which is assumed to be at zero potential) and ε_1 and ε_2 are the

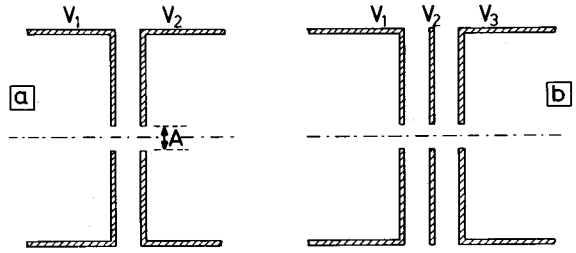

Fig. 8. Two- and three-element aperture lenses. The regions before the first and behind the second aperture are field free.

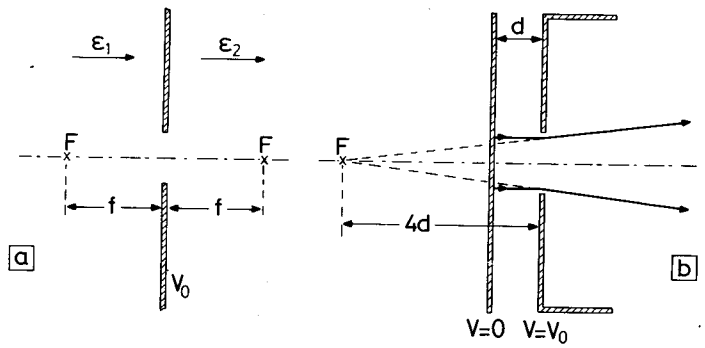

Fig. 9. The Calbick lens; a plate with an aperture separating two regions in space in which axial electric fields with different strengths ε_1 and ε_2 are present acts as a lens. This type of lens is considered to be thin, i.e., $f = F$. (a) General case $\varepsilon_1 \neq \varepsilon_2 \neq 0$. (b) Special case in which $\varepsilon_1 = V_0/d$ and $\varepsilon_2 = 0$; this is a negative lens with $f = -4d$.

electric fields left and right of the plane, respectively, then the focal length of this (thin) lens is given by:

$$f_a = 4E_0/q(\varepsilon_2 - \varepsilon_1)\,. \tag{15}$$

If $(\varepsilon_2 - \varepsilon_1)$ is positive, the sign for f_a is positive. Unlike all other lens types treated so far, the Calbick lens can be either converging or diverging, depending on the signs and the relative strengths of the fields. In first approximation the strength of the lens is independent of the diameter of the aperture. We will give the following example (fig. 9(b)): assume particles produced on a flat surface at zero potential are accelerated in a homogeneous electric fields $\varepsilon_1 = V_0/d$, then pass an aperture and enter a field-free region which for instance can be the first cylinder of a set of cylinder lenses. Now $\varepsilon_2 = 0$ and consequently $f_a = -4d$.

For a slit an equivalent relation holds:

$$f_s = 2E_0/q(\varepsilon_2 - \varepsilon_1)\,, \tag{16}$$

i.e., a slit lens is twice as strong as an aperture lens, however, only one-dimensional focussing occurs.

3.3.2. *Strong lenses*: *quadrupole lenses*

Although, because of their mechanical complexity, quadrupole lenses are not frequently encountered in lens systems used in atomic physics experiments, they have some distinct advantages. They are very strong for short lengths and they have the capability to change the shape of a beam in each of the two dimensions (x and y) independently. This makes it possible to change a circular (square) object into a rectangular one with the desired height and width. This property can be exploited to optimize the shape of a beam before it enters a (for instance one-dimensionally focussing) energy analyser; see sect. 4. For that reason we pay relatively much attention to this type of lens.

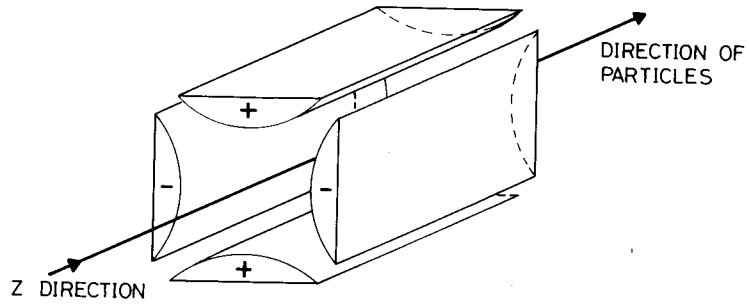

Fig. 10. Electrostatic quadrupole lens, consisting of four bars with hyperbolic surfaces. Opposing bars have the same potential. The plus and minus signs indicate equally large potentials which are positive and negative with respect to the particle source potential, respectively. Replacement by cylindrical rods with diameter 2.3 R_q (see fig. 11) gives a good approximation of the ideal field.

In principle a quadrupole lens consists of four bars with hyperbolic surfaces arranged according to fig. 10. In an electrostatic quadrupole the two sets of opposing hyperbolic bars have positive and negative potentials, whereas in the magnetic case they consist of magnetic north and south poles. Contrary to the other types of lenses discussed so far, quadrupole lenses are considered to be strong focussing devices. This is due to the particular shape of the electric (magnetic) fields (see fig. 11). Whereas the electric fields in axially symmetric lenses only have a relatively small radial component, the electric fields present in quadrupole lenses are fully radial and can extend over large z distances (the length is a free parameter). These fields vary linearly with the distance from axis and consequently such a set-up acts like a lens.

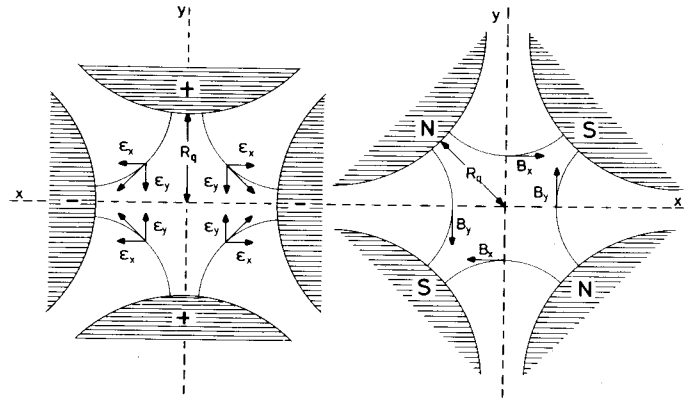

Fig. 11. The shape of the fields present in electrostatic and magnetic quadrupoles. The curved lines connecting the hyperbolic surfaces are electric ($\boldsymbol{\varepsilon}$) and magnetic ($\boldsymbol{B}$) field lines. The particles enter the lens perpendicular to the plane of the drawing. From the x and y components of the electric and magnetic fields it can be seen that a quadrupole lens is converging (positive) in one dimension and diverging (negative) in the other.

As is clear from fig. 11, this type of lens is positive or converging in one plane (the yz plane for positively charged particles) and negative or diverging in the other plane (the xz plane). Therefore the particle motion in the xz and yz planes have to be treated separately. In the converging and diverging planes the particle trajectories inside the lens can be described by means of trigonometric and hyperbolic functions, respectively (Regenstreif 1967, Hawkes 1970). The strength of a particular quadrupole field is given by the field number k:

$$\text{electrostatic lenses,} \quad k = \frac{1}{R_q}\left(\frac{qV}{E}\right)^{1/2}, \tag{17a}$$

$$\text{magnetic lenses,} \quad k = \frac{1}{R_q}\left[\mu_0 NI\left(\frac{q}{2mE}\right)^{1/2}\right]^{1/2}, \tag{17b}$$

R_q is the aperture radius (fig. 11); V is the potential on the poles, NI is the number of ampère-turns available per pole, E and m are the particle energy and mass, respectively. $\mu_0 = 4\pi \times 10^{-7}\,\mathrm{Hm^{-1}}$ is the magnetic susceptibility and q the elementary charge. Equations (17) hold for singly charged particles. The strength of the quadrupole as a whole is characterized by:

$$\theta = kL, \quad \text{where} \quad L = l + 1.1\,R_q, \tag{18a,b}$$

L is the so-called "effective length" of the quadrupole; l is the electrode length. Equation (18b) ensures that fringing field effects are properly taken into account. The position of the focal and principal planes are shown in fig. 12. For the converging plane one can write:

$$\frac{F_{c1}}{L} = \frac{F_{c2}}{L} = \frac{\cot\theta}{\theta}, \qquad \frac{f_{c1}}{L} = \frac{f_{c2}}{L} = \frac{1}{\theta \sin\theta}, \tag{19a}$$

and for the diverging plane:

$$\frac{F_{d1}}{L} = \frac{F_{d2}}{L} = -\frac{\coth\theta}{\theta}, \qquad \frac{f_{d1}}{L} = \frac{f_{d2}}{L} = -\frac{1}{\theta \sinh\theta}. \tag{19b}$$

One can now trace the particle trajectory through any number of quadrupole lenses by applying the transfer matrices given in eqs. (10) and (14) for each of the two planes separately. Note that f_d has a negative sign.

The transfer matrices for the focussing and defocussing planes, respectively, are:

$$M_+ = \begin{pmatrix} \cos\theta & (L\sin\theta)/\theta \\ (-\theta\sin\theta)/L & \cos\theta \end{pmatrix}; \qquad M_- = \begin{pmatrix} \cosh\theta & (L\sin\theta)/\theta \\ (\theta\sinh\theta)/L & \cosh\theta \end{pmatrix}. \tag{20}$$

These matrices describe the transfer from the entrance to the exit plane of the quadrupole lens.

It will be clear that a single quadrupole is not a very useful device because of its

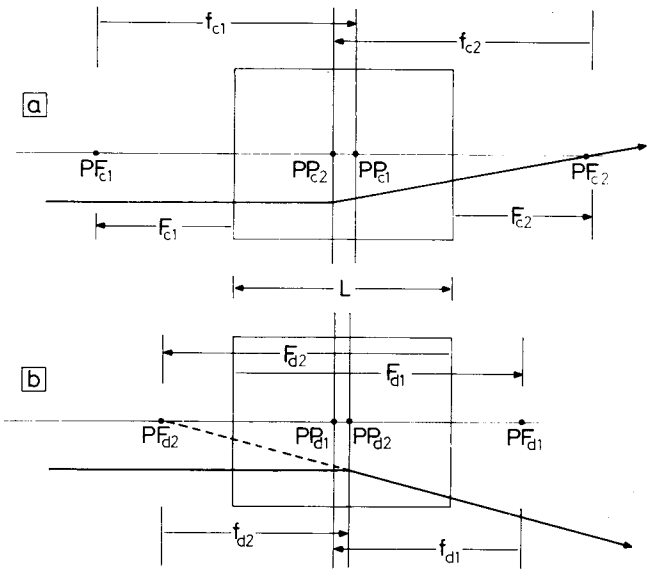

Fig. 12. The location of the focal and principal points (planes) $PF_{1,2}$ and $PP_{1,2}$, respectively, in the converging (a) and the diverging (b) plane. F_1 and F_2 are defined with respect to the front and back planes of the quadrupole respectively; f_1 and f_2 with respect to the focal points PF_1 and PF_2. Note the signs of the various quantities f and F (eqs. (19)) and the direction of the corresponding arrows (see also fig. 3(a)). The lens shown in this figure has $\theta < \pi/2$.

different behaviour in each of the two planes. However, it can be shown that a set of two quadrupoles in series, i.e., a converging–diverging combination in one plane and consequently a diverging–converging in the other plane, always acts as a positive lens in both planes, provided their distance is smaller than the sum of the focal lengths (fig. 13(a)). In general such a doublet will not image an object at the same axial (z) position for the xz as well as the yz plane. Only a careful choice of the strength of each of the two quadrupoles and their mutual distance will produce an image at one axial position in the xz and yz planes simultaneously. Also the magnification will be different for each of the two dimensions. This leads to a distortion; of a circular object an elliptical image is formed. The ratio δ between the magnifications in the xz and yz planes usually has values between 2 and 20. This effect is an advantage whenever it is necessary to transform a slit shaped object into a circular image, or vice versa. Note that Liouville's theorem (1) still holds for each plane independently. In case one wants to avoid too large a distortion a combination of two doublets or of three quadrupoles, a so-called triplet can be used (fig. 13(b)). The distortion δ can now easily be made close to unity. Another advantage of a (symmetrical) triplet is that the principal planes are situated symmetrically with respect to the median plane of the lens and are therefore, to a large extent, independent of the level of excitation. If one considers the lens to be thin, this means that changing the level of excitation does not change the position of the lens in either of the two planes. If the excitation of a doublet is changed, the principal planes of the diverging–

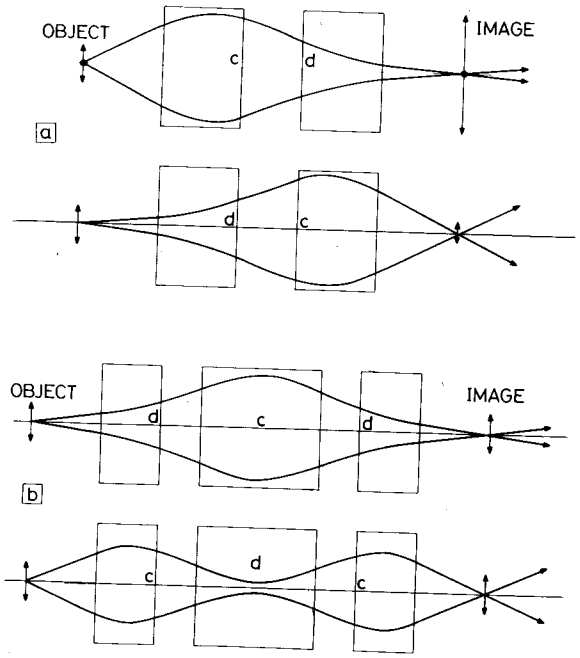

Fig. 13. A comparison between a quadrupole doublet (a) and triplet (b). The upper and lower figures of (a) and (b) show the imaging in the two main planes of the quadrupoles. c and d indicate the converging and diverging planes of the various singlets. Note that the image distortion is much larger with doublets than with triplets.

converging and converging–diverging combinations shift in opposite directions which makes the adjustment of the lens as a whole more difficult.

A handy graphical method for determining the combination of doublet and (symmetrical) triplet parameters yielding coinciding images in the xz and the yz planes is given by Enge (1959, 1961). An analytical treatment of single quadrupoles, doublets and triplets is given by Regenstreif (1967). Hawkes (1970) gives an extensive tabulation of the parameters of the various types of quadrupole systems; aberration coefficients are included.

As was already mentioned in the beginning of this section, the main advantage of quadrupoles above weak lenses is the fact that the focussing is much stronger. For instance a three-element cylinder einzel lens with $V_2/V_1 = 5$ has approximately the same strength as a rather short quadrupole triplet with excitation potentials of the order $(0.2\text{–}0.3)V_1$. This is already a large advantage for potentials V_1 of the order of kilovolts. Another advantage of quadrupoles is that the spherical and chromatic aberrations can be made very small or even zero. This, however, usually requires very sophisticated designs (Hawkes 1970). The major disadvantages of quadrupoles are the large number of independently controllable voltages which are required and the complex mechanical construction. The requirements on the mechanical construction are slightly relaxed by approximating the hyperbolic surfaces by cylindrical rods with a diameter equal to $2.3\,R_q$. Usually the additional aberrations due to this non-perfect shape of the electrodes are negligible.

3.4. *Aberrations*

So far we have treated lenses in the paraxial approximation; besides that it was implicitly assumed that the particles to be transported were mono-energetic. In general, however, neither of these two conditions is fulfilled. This gives rise to the so-called geometrical and chromatic aberrations, respectively. Besides that imperfections due to misalignment and inaccurate machining of lens components cause mechanical aberrations. We will limit ourselves to chromatic and geometrical aberrations of electrostatic lenses.

Except in applications such as electron microscopes, one is usually not interested in producing an exact image of an object. It usually suffices to ensure oneself that the various aberrations do not increase the overall size of the image by more than a small fraction of its aberration-free size. This may not be sufficient in cases where one wants to make an image on a high resolution position sensitive detector such as a channel plate (sect. 5).

(a) *Chromatic aberrations*

Every ensemble of particles with average energy E will have a certain energy spread ΔE. Due to the fact that the strength of a lens is dependent on the ratio of the potentials applied (or equivalently the ratio of particle energies, because the potentials are defined with respect to the particle source potential), particles with an energy difference ΔE will see lenses with different strength. Consequently lenses are discriminating elements, but have no dispersion in the true sense of the word; this gives rise to chromatic aberrations. This can be expressed by means of a chromatic aberration coefficient C_{ch} (Hanszen and Lauer 1967):

$$\Delta r_{ch} = \alpha C_{ch} \frac{\Delta E}{E}, \tag{21}$$

Δr_{ch} is the transverse displacement in the paraxial (aberration-free) image plane of the trajectory of a particle with energy $E \pm \Delta E$ leaving a point object on axis, making an angle α to it. For weak lenses, to our knowledge, these coefficients C_{ch} are not tabulated as such. However, the energy dependence of the positions of principal and focal planes can be deduced from the tables given by Harting and Read (1976) and the various papers mentioned in sect. 3.3.1. For very strong magnifications and diminutions Hanszen and Lauer (1967) give approximated expressions for C_{ch}. For quadrupoles these coefficients are tabulated by Hawkes (1970).

(b) *Geometrical aberrations*

All aberrations up to third order, which are due to non-paraxial trajectories in

planes containing the axis, can be expressed in terms of the so-called spherical aberration coefficient (Adams and Read 1972, Hanszen and Lauer 1967). This includes aberrations like coma, distortion, field curvature and spherical aberration. Only aberrations like off-axis astigmatism cannot be treated in this way. However, for the reasons mentioned in the beginning of this section we consider the third order spherical aberration coefficient C_s to be sufficiently indicative for the overall image size. It is defined as (Hawkes 1967) (see fig. 14):

$$\Delta r_s = M_L C_s \alpha^3 , \tag{22}$$

where Δr_s is the transverse displacement in the paraxial image plane of a ray which leaves a point object on axis making an angle α to it. M_L stands for the linear magnification. For weak lenses the coefficients C_s are tabulated by Harting and Read (1976) and in the other papers mentioned in sect. 3.3.1. For rays parallel to the axis ($\alpha = 0$) a modified coefficient $C_s(\infty)$ is given:

$$\Delta r_s = \tfrac{1}{2} C_s(\infty)(d/D)^3 , \tag{23}$$

where $d/2$ is the transverse displacement of the ray from the axis on the object side; D is the characteristic dimension; i.e., cylinder or aperture diameter, slit width. The geometrical aberration coefficients for quadrupoles are extensively treated and tabulated by Hawkes (1970).

Finally we give a few practical remarks which have proved to be very useful for minimizing the aberrations of the most commonly used weak lenses:

– The aberrations in the image can usually be kept within a few percent of the characteristic lens diameter D (i.e., cylinder or aperture diameter, slit width) provided the filling factor of the lens is less than 50% and the lens is used in the accelerating mode. The filling factor is defined as the percentage of D which would be filled if the trajectories in the field-free parts of object and image space are extrapolated to the centre of the lens (whichever fills the lens most).

– Keep the lens as short as possible in terms of the total number of units D. Whenever particles have to be transported over a certain fixed distance between a source and, say, an energy analyser it is preferable to cover that distance in a "short" strong (large diameter) lens rather than in a "longer", weaker (smaller diameter) lens; short and long being defined in terms of units D.

– The aberrations of multi-element lenses are smaller for accelerating intermediate elements than for decelerating ones (see for example fig. 14).

– Beam steering devices like deflection plates have to be kept away from lens gaps at least one unit D. It is advisable to apply these plates behind every aperture or slit which defines a source or an (intermediate) image. Another possibility is to introduce deflecting plates in the center element of an einzel lens, or to use the rods of the central quadrupole in a triplet for beam steering.

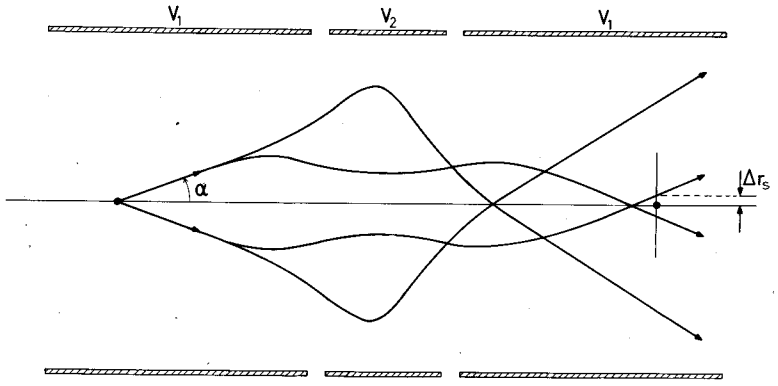

Fig. 14. Actual electron paths in a cylindrical einzel lens operated in the accelerating ($V_2/V_1 = 12.1$) and decelerating ($V_2/V_1 = 0.045$) modes (from Adams and Read (1972a)). In both modes these lenses have the same first-order focussing properties. However, due to spherical aberrations the image positions are strongly shifted. The length of the central cylinder is equal to the diameter D; the vertical scale is a factor 2.5 larger than the horizontal one. The object distance the paraxial image distance are equal to $2D$ (dots). The rays closest to the axis are those of the accelerating mode. The filling factor is 60% in both cases.

3.5. Design of practical lens systems

The complexity of a lens system strongly depends on the number of parameters one wants to control independently. Usually one wants the system to fulfil a combination of some of the following requirements:

(a) fixed object and image positions;

(b) variable particle energy at the exit side of the lens for fixed energy at the entrance side;

(c) fixed linear or angular magnification (note eq. (1));

(d) control of beam angle; one usually requires the beam angle at the exit side to be zero.

In the following we will limit ourselves to examples of cylinder lenses. However, these examples hold equally well for the other types of lenses treated in sect. 3.3.1. Requirement (a) can be fulfilled by one single lens, i.e., two cylinder elements. Any additional degree of freedom requires an additional element (i.e., an additional lens gap). For instance for the simultaneous fulfillment of (a) and (b) one needs at least three cylinder elements. An example of the focussing conditions for such a "zoom lens" are given in fig. 15. The linear magnification cannot be controlled. Besides that, the total range of voltage ratios V_3/V_1 in which imaging is possible depends on the object and image distances P/D and Q/D, respectively. As can be seen in fig. 16 the beam angle θ_B at the image side of a three-element zoom lens is not zero (dashed rays; $V_4 = V_2$). The insertion of an extra element V_4, i.e., the introduction of a two-gap einzel lens at position B can provide a zero beam angle at the exit side of the lens. Lens B has to be excited such that the second focal point PF_{2A} of lens A is imaged on the first focal point PF_{1C} of lens C (Kuyatt 1967). If this system has to cover a large range of voltage ratios V_3/V_1, the position of the intermediate image does not coincide with field lens B

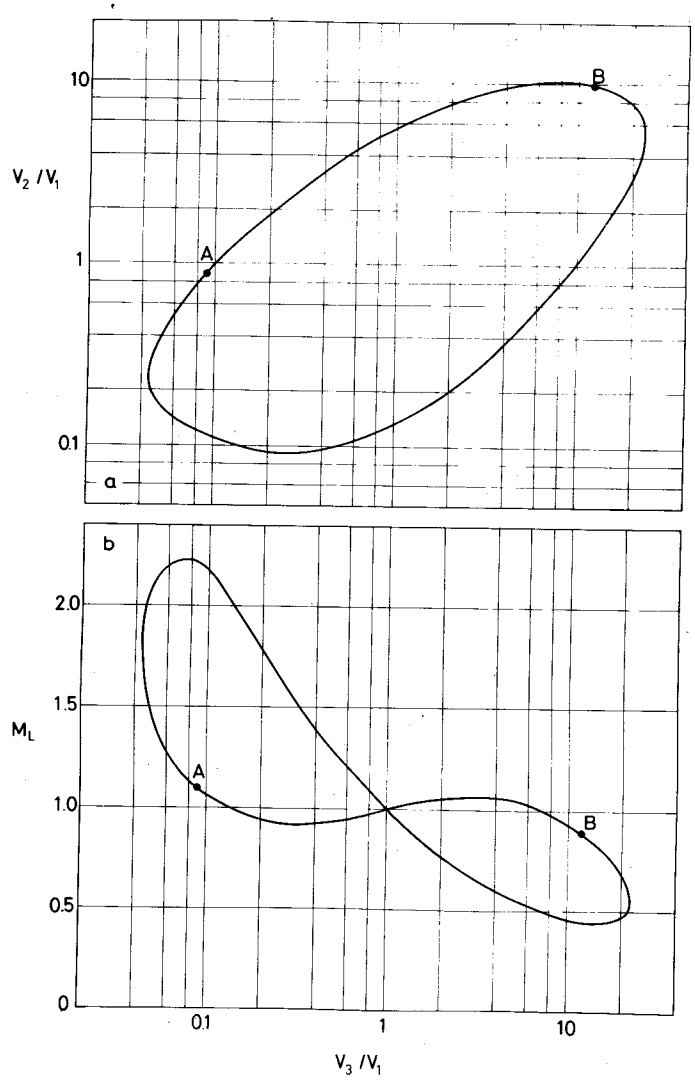

Fig. 15. Focussing conditions of a three-element cylinder "zoom lens" (a) and the corresponding linear magnification (b). The length of the central element is equal to its diameter D; the three cylinders have the same diameter. The width of the gaps is 0.1 D. The object and image distances are chosen $P/D = Q/D = 3$ (see fig. 3(a)). The curves are deduced from tables given by Harting and Read (1976). Note that in this particular example the linear magnification M_L deviates from unity less than 10% in the voltage ratio range $0.1 \leqslant V_3/V_1 \leqslant 10$ (between the points A and B).

for all values of V_3/V_1; this causes a shift in position of the final image. In principle this can be corrected by applying different potentials on the two V_2 elements.

An elegant five-element system in which the conditions (a)–(d) are satisfied simultaneously is described by Heddle (1971a); see fig. 17. The five cylinders can

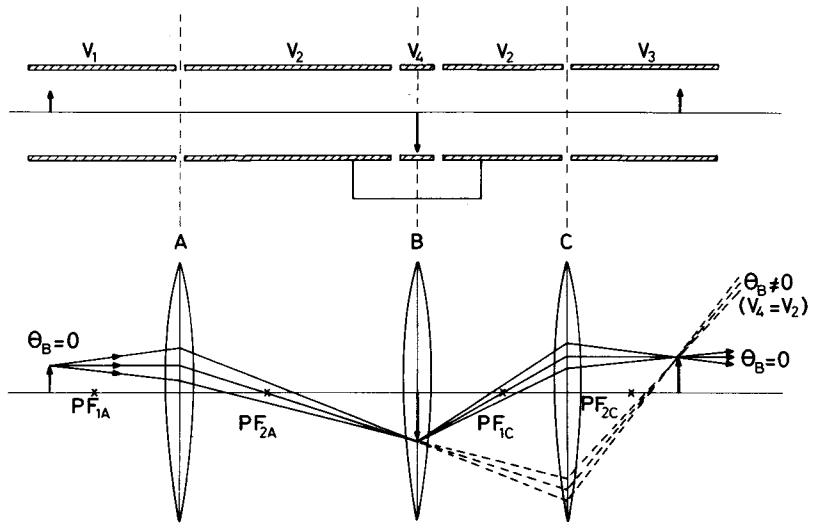

Fig. 16. A source object with beam angle $\theta_B = 0$ imaged by means of a three-element lens ($V_4 = V_2$; two lens gaps at A and C) generally yields an image with beam angle $\theta_B \neq 0$; see dashed line trajectories. The addition of an einzel lens B ($V_4 \neq V_2$) which images the focal point PF_{2A} of lens A on the focal point PF_{1C} of lens C leads to an image with $\theta_B = 0$ (solid line trajectories). Lens B is called a field lens. For the sake of simplicity the lenses are approximated by thin lenses.

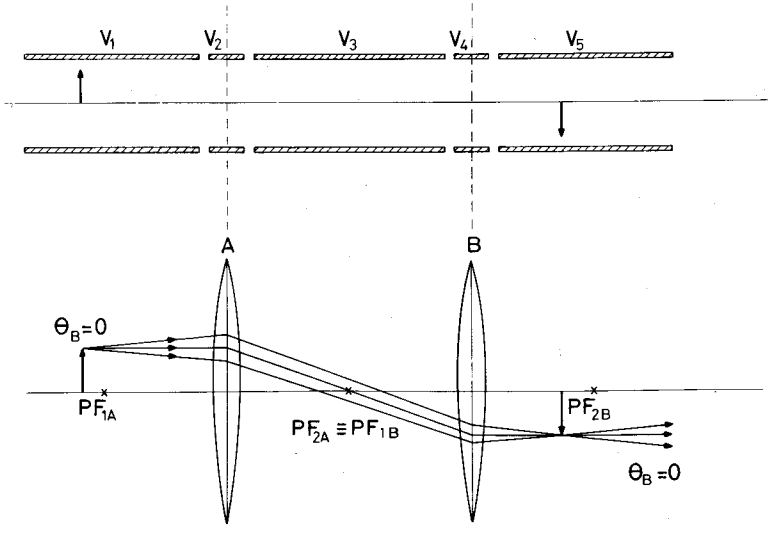

Fig. 17. An image with beam angle $\theta_B = 0$ can be obtained when an object with $\theta_B = 0$ is imaged by means of a combination of two lenses A and B in which the second focal point PF_{2A} of lens A coincides with the first focal point PF_{1B} of lens B.

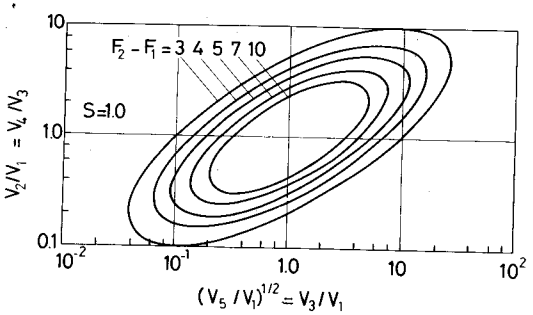

Fig. 18. The focussing conditions for "Heddle-type" lens combinations (fig. 17). $F_2 + F_1$ is the distance between the two symmetry planes of the two three-element lenses A and B, expressed in units of the cylinder diameter D. The length of the central elements of A and B is equal to D. Any object at the entrance side is imaged at a distance $2(F_2 + F_1)$ to the right. For further details, see text.

be considered to form two three-element lenses A and B. If the second focal point PF_{2A} of lens A coincides with the first focal point PF_{1B} of lens B, the beam angle at the exit side of the lens system is zero for zero beam angle at the entrance (fig. 2). Heddle showed that if the two lenses are identical, i.e., $V_5/V_3 = V_3/V_1$ and $V_4/V_3 = V_2/V_1$ and if for every ratio V_5/V_1 V_2 is tuned such as to make PF_{2A} coincide with PF_{1B}, a zoom lens is obtained with zero exit beam angle and a linear and angular magnification equal to: $M_L = M_A = (V_1/V_5)^{1/4}$. Consequently, the magnification is only very weakly dependent on V_5/V_1. In fig. 18 the focussing conditions are shown for various distances between the symmetry planes of A and B. By adding an additional einzel lens at the entrance side (two more elements) this system can also handle incoming beams with beam angles unequal to zero.

Other illustrative examples of lens systems have been given by Kurepa et al. (1974) and Chutjian (1979).

4. Energy and mass analysis of charged particles

4.1. Introduction

One of the very commonly studied pieces of information is the energy spectrum of the particles formed by synchrotron radiation as a function of photon energy.

The emphasis of this section is on devices for the determination of energy distributions. Besides that some attention is paid to mass and velocity analysis. There is of course redundance in the set of parameters energy, mass (momentum) and velocity; whenever two out of these three parameters are known, the third one can be calculated. Analysers for these parameters can be subdivided into three categories:

Static field analysers: In this category there are two classes. In the first class charged particles are deflected in electric and/or magnetic fields; the deflection is more or less, depending on the particle momentum or kinetic energy. This results

in a spatially resolved spectrum, if focussing occurs. In the second class a potential barrier is set up to reflect all particles with energies below a certain preset value, i.e., these retarding potential analysers act as a high pass filter. The integrated energy distribution can be determined by varying the retarding potential.

Dynamic field analysers: The quadrupole RF analyser is treated as an example of an analyser in which (dynamic) electromagnetic fields are applied.

Analysers without fields: Time of flight analysis; the velocity of a particle is determined by measuring the time it takes the particle to cross a well-known distance. In this case the spectrum is time resolved.

The three above-mentioned categories contain several tens of different analysers. Due to lack of space it is impossible to treat all of them extensively. Therefore we will limit ourselves to those types which have proved to have the best overall characteristics. This means that most attention will be paid to the electrostatic deflection type analysers. The most popular analysers of this group will be described shortly and comparative tables will be given (sect. 4.2). This enables the reader to make a "first-order" choice for his particular application. For the final optimization of a chosen type of analyser the reader will be referred to papers treating this particular analyser in depth. Reviews on this matter have been given by Kuyatt (1968), Rudd (1972), Stechelmacher (1973), Wannberg et al. (1974), Afanas'ev and Yavor (1974). An excellent recent review is the one by Roy and Carette (1977).

In the past various types of magnetic deflection type analysers have been used, especially in the field of beta ray spectroscopy. However, the last decade the role of these types of instruments for energy analysis has become relatively unimportant. The main reason for this is the difficulties which are encountered in the shielding of the magnetic stray fields. Because magnetic fields are still widely used in mass spectrometry a few basic features of sector fields are treated in sect. 4.2.4.

Analysers based on retarding fields which are widely used in applications such as UV and X-ray photoelectron spectroscopy and low energy electron diffraction (LEED) are dealt with in sect. 4.3. Quadrupole analysers are treated in sect. 4.4 and time-of-flight analysers in sect. 4.5. Finally attention is paid to multichannel detection techniques, which can reduce data acquisition times considerably (sect. 4.6), the problems caused by magnetic stray fields and their elimination (sect. 4.7), to the choice of materials (sect. 4.8) and last but not least to the energy and transmission calibration of complete systems (sect. 4.9).

4.2. Deflection type analysers

4.2.1. Basic features and terminology

In electrostatic and magnetic deflection type analysers the trajectory of a charged particle depends on its energy and momentum, respectively. This results in spatial separation of particles with different energies (momenta). This is shown schematically in fig. 19. It shows two cross sections of an arbitrary energy analyser; fig. 19(a) gives the dispersive plane and fig. 19(b) the non-dispersive plane. Two particles with energy difference $\Delta E = E_0 - E_1$ entering the analyser along coinci-

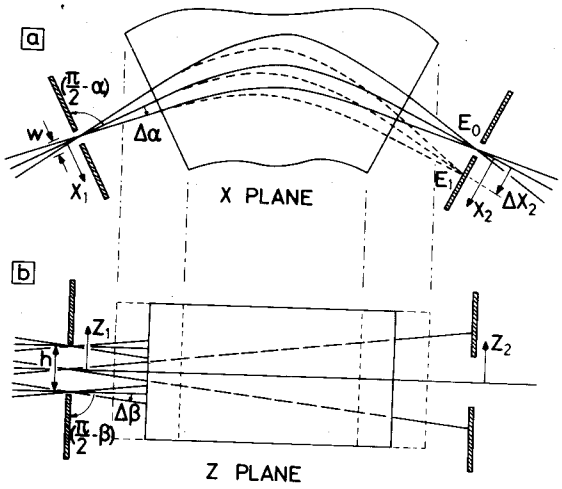

Fig. 19. General deflection type analyser. The relevant parameters in the dispersive plane (a) and the non-dispersive plane (b) are shown; these planes are perpendicular to each other. $\Delta\alpha$ and $\Delta\beta$ are semi-opening angles, w and h are the slit width and height, respectively. Particles with an energy E_1 different from the pass energy E_0 are focussed a distance Δx_2 away from the centre of the exit slit. In this figure it is assumed that there is only focussing in the dispersive plane. Note that in a calculation of the base width resolution the beam angle θ_B has to be included ($\Delta\alpha = \theta_B + \frac{1}{2}\alpha_i$; see fig. 1).

ding trajectories are found to be separated by a distance Δx at the exit of the analyser. Although it is not strictly necessary for the separation of particles with different energies, the analysers to be discussed in this section all have focussing properties in at least the dispersive plane. This greatly enhances the acceptance of the analyser. As in the case of lenses (sect. 2) this focussing action can be characterized by two principal and two focal planes. For those analysers which are compatible with lens systems the location of these planes will be given.

The energy resolution of an arbitrary analyser will depend on many, mainly geometrical, factors; see fig. 19. It depends on the opening angles $\Delta\alpha$ and $\Delta\beta$ in the dispersive and non-dispersive planes, respectively, on the entrance and exit slit widths w_1 and w_2 and heights h and on a characteristic "dispersive length" L, i.e., a length related to the trajectory in the dispersive field. The influence of these parameters is determined in the following way. We assume the central trajectory to be characterized by entrance coordinates $z_1 = x_1 = 0$, entrance angles $\beta = 0$ and α and exit coordinate $x_2 = 0$ (fig. 19). A particle entering the analyser under slightly different conditions ($\alpha \pm \Delta\alpha$, $\pm\Delta\beta$; $x_1 \neq 0$; $z_1 \neq 0$, $E_1 = E_0 + \Delta E$) will pass the exit plane at $x_2 \neq 0$. A Taylor expansion up to second (partly third) order now gives:

$$\Delta x_2 = \frac{\partial x_2}{\partial x_1}\Delta x_1 + \frac{\partial x_2}{\partial E}\Delta E + \frac{1}{2!}\frac{\partial^2 x_2}{\partial \alpha^2}(\Delta\alpha)^2 + \frac{1}{3!}\frac{\partial^2 x_2}{\partial \alpha^3}(\Delta\alpha)^3 + \frac{1}{2!}\frac{\partial^2 x_2}{\partial \beta^2}(\Delta\beta)^2 + \frac{1}{2!}\frac{\partial^2 x_2}{\partial z_1^2}(\Delta z_1)^2 + \frac{1}{2!}\frac{\partial^2 x_2}{\partial x_1 \partial \alpha}(\Delta\alpha)(\Delta x_1) + \frac{1}{2!}\frac{\partial^2 x_2}{\partial z_1 \partial \beta}(\Delta\beta)(\Delta z_1) + \cdots . \quad (24)$$

The last two aberration terms and those not given are either zero or small (except for the cylindrical mirror analyser (see sect. 4.2.3) when using wide slits). We will not consider them any further (see also Wannberg et al. (1974)). The first term in the expansion gives the linear magnification M_L^A of the analyser: $M_L^A = \partial x_2/\partial x_1$. The second term is related to the so-called dispersion D of the system which is defined as:

$$D = E(\partial L/\partial E) \propto E(\partial x_2/\partial E), \quad (25)$$

i.e., the change in image position of a particle trajectory for an infinitesimal change in particle energy. The term linear in $(\Delta\alpha)$ is zero due to the assumption of first-order focussing, at the specific entrance angle α, i.e.: $\partial x_2/\partial\alpha = 0$. Some analysers are designed to have second-order focussing; in that case $\partial x_2/\partial\alpha = \partial^2 x_2/\partial\alpha^2 = 0$. For that reason also the aberration term with $(\Delta\alpha)^3$ is included in eq. (24). The term linear in $\Delta\beta$ is always zero, as can be seen as follows: a small opening angle in the non-dispersive plane reduces the velocity in the dispersive plane with a factor $\cos\beta \approx (1 - \frac{1}{2}\beta^2)$. This means that for small angles β the velocity and hence the energy in the dispersive plane is a function of β^2. Because in this first order x_2 is linearly dependent on the energy it follows that $\partial x_2/\partial\beta = 0$ for $\beta = 0$.

It is obvious that eq. (24) contains the information needed to obtain the energy resolution. Let us define the absolute base energy resolution, ΔE_B, as the range of energies over which a mono-energetic beam produces an output in an analyser set at fixed deflection voltage. Then it becomes clear that the relative base width resolution may be written as:

$$\Delta E_B/E = (w_2 + \Delta x_2)/D,$$

where w_2 is the exit slit width. Taking Δx_2 from eq. (24), with $(\partial x_2/\partial E)\,\Delta E = 0$ for a mono-energetic beam, we arrive at:

$$\frac{\Delta E_B}{E} = C_w\left(\frac{w}{L}\right) + C_\alpha(\Delta\alpha)^2 + C'_\alpha(\Delta\alpha)^3 + C_\beta(\Delta\beta)^2 + C_h\left(\frac{h}{L}\right)^2 . \quad (26)$$

The first term on the right-hand side of (26), the linear resolution term, describes the apparent energy spread due to the finite slit widths of the analyser. For this term one can write:

$$C_w(w/L) = (w_1 + w_2)/D = 2w/D,$$

in which $2w$ is the sum of the entrance and exit slit widths and D the dispersion of the system. The second term gives the apparent energy spread of a mono-energetic beam with an angular divergence $\Delta\alpha$ (semi-angle, see fig. 19): $C_\alpha(\Delta\alpha)^2 = \Delta L/D$. In this relation ΔL ($\propto \Delta x_2$) is the shift in image position given by eq. (24) when only the $(\Delta\alpha)^2$ term is considered. Similarly $C'_\alpha(\Delta\alpha)^3 = 2\Delta L'/D$. The factor

two difference between the second- and the third-order term is due to the fact that an angular variation from $+\Delta\alpha$ to $-\Delta\alpha$ gives rise to variations ΔL and $2\Delta L'$ (i.e., from $+\Delta L'$ to $-\Delta L'$) respectively. All the other terms are defined in a similar way.

The various coefficients C are given in table 1 for several types of analysers. In literature often the energy resolution is defined to be $\Delta E_{1/2}/E_0$ where $\Delta E_{1/2}$ is the full width at half maximum (FWHM) of the distribution. In case of triangular energy distributions we can write $\Delta E_{1/2} = \frac{1}{2}\Delta E_B$. Usually this will not be the case. If one is interested in the halfwidth one has to know the exact shape of the distribution. This can be expressed in a so-called spectrometer function. The most accurate way to determine this function is to calculate the trajectories of a large number of charged particles each with a different set of initial conditions of opening angle, position and energy. In this way all the aberrations due to finite opening angles and slit dimensions automatically show up in the integrated result (Roy and Carette 1971a,b). Also aberrations due to fringing fields at the entrance and exit side of the analyser can be included. For most of the analysers discussed in the following sections this spectrometer function is known; in some cases the above-mentioned trajectory calculations have been performed; in other cases more

Table 1
Survey of constants specific for various types of deflection analysers (eq. (26)).*

Analyser		C_w	C_α	C'_α	C_β	C_h
Parallel plate analyser	$\alpha = 45°$	2	2	–	1	0
	$\alpha = 30°$	3	0	$16/\sqrt{3}$	1	0
Cylindrical mirror analyser	$\alpha = 54.5°$, $n = 0$, $k = 1$	1.29	1.65	–	–	–
	$\alpha = 56.5°$, $n = 0$, $k = 1.25$	1.13	1.63	–	–	–
	$\alpha = 38.8°$, $n = 1$, $k = 0.94$	2.41	0	5.87	–	–
	$\alpha = 42.3°$, $n = 2$, $k = 1.31$	2.20	0	5.54	–	–
	$\alpha = 60°$, $n = 2$, $k = 2.06$	0.92	1.45	–	–	–
Spherical deflection analyser	$\Phi = 180°$	1	1	–	0	1/8
	$\Phi = 90°$	1	2	–	1/2	1/16
Cylindrical deflection analyser	$\Phi = 127°$	2	4/3	–	1	0
Magnetic deflection analyser	$\Phi = 180°$	2	1	–	1	0
Wien filter analyser	$L = \pi v_D/\omega$	2π	3	–	1	0
	$L = \pi v_D/2\omega$	2π	16	–	1	0

*In all cases the linear magnification M_L is assumed to be unity. This means that in those cases where the object and image distances are not fixed by constraints of the analyser, they are chosen equal ($P' = Q'$). Non-relevant coefficients have been left out (dashes). Note that the dispersion D is given by $D = 2L/C_w$ (see eq. (26)). For further information see sects. 4.2.3.–4.2.5 and figs. 20–28.

or less accurate analytical approximations have been derived. References dealing with specific spectrometer functions are given in the separate sections.

Apart from the base width or halfwidth resolution there are usually other, sometimes equally important parameters on which one can base the choice of a particular analyser. For instance, if the process under study yields high count rates, one might want to concentrate on high resolution, if necessary at the expense of transmission. In case of low signal levels the optimum analyser will be one with a good transmission. Apart from resolution and transmission several more characteristic quantities have been introduced in literature. A more or less complete list is the following:

Relative resolution $\Delta E/E$: the ratio between the width ΔE (either halfwidth or base width) of the energy distribution and the energy E of the particles emerging from the analyser.

Absolute resolution ΔE: the width of the energy distribution.

Resolving power $E/\Delta E$: the inverse of the relative resolution.

Transmission T: the ratio of the emergent flux of particles at the pass energy to the flux entering the analyser; generally $T = 1$ for deflection type analysers (no grids present).

System collection efficiency $C(E)$: collection efficiency of the entire system including source area and solid angle, lens and analyser transmission, energy band pass and detector efficiency (sect. 4.9).

Étendue λ: product of entrance solid angle and entrance area (Heddle 1971b).

Luminosity Λ: product of entrance solid angle, entrance area and transmission; i.e., $\Lambda = \lambda T$.

4.2.2. Optimization and pre-retardation

In principle it is always possible to obtain a required energy resolution ΔE by simply enlarging the dimensions of the analyser at a fixed slit width. Provided the aberration terms $C_\alpha(\Delta\alpha)^2$, $C_\beta(\Delta\beta)^2, \ldots$ in eq. (26) are sufficiently small, an increase of L directly leads to an improved resolution $\Delta E/E$. However, usually it is necessary to minimize the dimensions of the various experimental components in order to keep the overall size (and weight) of the experiment within reasonable limits. Pre-retardation, or, if necessary, pre-acceleration of the charged particles before they enter the analyser is a possible way to optimize the resolving power and/or luminosity (étendue) for a fixed analyser size, or, alternatively to obtain the minimum size of a certain type of analyser capable of delivering the required performance. If for a given type and size energy analyser the energy of the transmitted particles is denoted by E_0, then the energy resolution $(\Delta E)_0$ is given by (see eq. (26)):

$$(\Delta E)_0 = E_0[C_w(w/L) + C_\alpha(\Delta\alpha)^2 + C_\beta(\Delta\beta)^2 + C_h(h/L)^2]\,. \tag{27}$$

For analysers with second-order focussing the term $C_\alpha(\Delta\alpha)^2$ has to be replaced by $C'_\alpha(\Delta\alpha)^3$.

The optimization of étendue (luminosity) versus resolution can in principle be regarded as a two-step procedure:

In the first step the relative magnitude of the various terms on the right hand side of eq. (27) is optimized. As an example we will consider a "zero-order draft" in which the last three terms on the right-hand side are much smaller than the term $C_w(w/L)$. Keeping the pass energy of the analyser constant, we now change the optical system transporting the particles from the target to the analyser such that the linear magnification M_L becomes smaller and consequently the angular magnification M_A larger. This in accordance with Liouville's theorem (eqs. (1) and (5)), which states that $M_L M_A = 1$ in case no acceleration or deceleration takes place. A decrease of M_L with a factor k_M means that the slit-width w can be reduced with the same factor without any loss of particles, i.e., the term $C_w(w/L)$ in eq. (26) can be made smaller by a factor k_M. This leads to an increase in resolving power. Alternatively one can choose to keep the slit-width constant; then a larger fraction of the particles emitted by the source will be accepted by the analyser. However, due to the decrease of M_L, the angular aberration terms increase with a factor k_M^2. k_M should now be chosen such that the sum of the four terms reaches a minimum value. Rudd (1972) showed that in case of first-order focussing the optimum situation is obtained when:

$$C_\alpha(\Delta\alpha)^2 \approx C_\beta(\Delta\beta)^2 \approx \tfrac{1}{2}C_w(w/L)\,. \tag{28}$$

The halfwidth resolution can then be approximated by:

$$\Delta E_{1/2}/E = \tfrac{1}{2}C_w(w/L) + \tfrac{1}{4}C_\alpha(\Delta\alpha)^2 + \tfrac{1}{4}C_\beta(\Delta\beta)^2\,. \tag{29}$$

In eqs. (28) and (29) the fourth term of eq. (27) is assumed to be small.

In the second step the pass energy of the analyser is reduced; however, the lens system is adapted such that the mutual ratios of the four aberration terms remain constant. The first step in the optimization thus remains valid. This step can also lead to an increase of the étendue of the total system, i.e., the system accepts a larger fraction of the particles emitted by the source. The gain which is possible in this respect depends on several assumptions (see for instance, Heddle 1971b). We will take the following example: we assume the fourth term $C_h(h/L)^2$ does not contribute to the resolution. This is for instance the case when C_h is small or zero (analysers with one-dimensional focussing). Then the slit height h can in principle be made very large. However, the maximum effective height will usually be determined by the height of the detector. Besides that, accepting too large a beam height may lead to unacceptable aberrations in the entrance optics (see sect. 3.4). Although this is not strictly necessary, for the sake of simplicity, we choose axially symmetric entrance optics, i.e., the opening angles $\Delta\alpha$ and $\Delta\beta$ are influenced at the same rate. Now, we assume that the entrance lens system retards the particles with a factor k_R in energy. Of course also the pass energy E_R of the analyser is reduced with the same factor: $E_R = E_0/k_R$. If we now require the resolution $(\Delta E)_0$ to remain constant, eq. (27) shows that a reduction of the pass energy with a factor k_R allows us to increase the slit width with a factor k_R and each of the angles $\Delta\alpha$ and $\Delta\beta$ with a factor $k_R^{1/2}$. This means that the analyser étendue (for constant h) is increased with a factor k_R^2. However, according to Liouville's theorem (eqs. (1) and (5)) the reduction in energy leads to an increase of the product $M_L M_A$ by a factor $k_R^{1/2}$ and hence the particle intensity per unit area and unit source solid angle as seen by the analyser is reduced by a factor k_R. Consequently the total gain in étendue of the system consisting of analyser and entrance optics is increased by a factor k_R. Of course this gain can only be realized for sufficiently extended sources and for not too low pass energies; pass energies of a few hundred meV to 1 eV are the lowest practically attainable; see sect. 4.8.

Another advantage of pre-retardation is that the larger ratio of slit width to characteristic analyser length L usually relaxes the requirements on the mechanical accuracy.

Heddle (1971b) compared the gain in étendue versus resolution which can be realized theoretically in this way for two types of cylindrical mirror analysers and for spherical deflection analysers with slits of different size and shape; see table 2. Table 2 also gives a ranking of the various analyser types based on other criteria: luminosity versus resolution, transmission versus resolution and on the "general

Table 2
A ranking of Electrostatic Deflection Analysers according to various criteria (1 is best).

Analyser		Luminosity vs. resolution[a]	Étendue vs. resolution[b]	Distribution characteristics[c]	Transmission vs. base resolution[d]
Parallel plate analyser	$\alpha = 45°$			5	
	$\alpha = 30°$			2	
Parallel plate fountain analyser	$\alpha = 45°$				6
	$\alpha = 30°$				1 (MTW), 4
Cylindrical mirror analyser	$\alpha = 54.5°$		1		
	$\alpha = 42.3°$	1(MTW), 2	2	1	2(MTW), 5
Spherical deflection analyser	$\Phi = 180°$	3	3	3	3
Cylindrical deflection analyser	$\Phi = 127°$			4	

MTW stands for Minimum Trace Width.
[a]Sar-El (1970); Sar-El also included a comparison with the so-called Spherical Mirror Analyser. However, due to the difficult mechanical construction, this type of analyser was not built so far. Therefore it is not treated in this paper.
[b]Heddle (1971b).
[c]Roy and Carette (1971a,b).
[d]Schmitz and Mehlhorn (1972).

distribution characteristics" of the various analysers. A similar table is given by Roy and Carette (1977).

One more remark with respect to pre-retardation has to be made: If the particles leaving the target cover a wide energy range then the emittance (see sect. 1) of the source very likely changes with energy. This will for instance be the case if the opening angles with which the particles leave the target and the target area remain (more or less) constant with changing particle energy. This means that for every particle energy a new optimum analyser setting can be found. This of course is very unpractical. Usually one setting is chosen in which the analyser is more or less optimized for the whole energy range to be covered.

In this respect two modes of operation of the total system can be chosen (Nöller et al. 1974). The first mode is the constant relative resolution mode; $\Delta E/E_T$ is constant. The lens system between target and analyser retards (or accelerates) the charged particles with the same factor. The advantage of this way of operation is that the transmission of the lens system and the analyser is constant and consequently it is very suitable for quantitative measurements (see, however, sect. 4.9). Note that the resolution ΔE changes with the pass energy E.

The second mode of operation is one in which the lens system decelerates or accelerates the particles from their target energy to a fixed energy; the pass energy of the analyser being kept at the same value. In this case the resolution ΔE remains constant. However, if one wants to do quantitative measurements a well-designed lens system is required to ensure that the transmission is independent of the target particle energy. Examples of such lens systems are given by Nöller et al. (1974) and Kurepa et al. (1974); see also sect. 4.9.

4.2.3. *Electrostatic analysers*

For a quick survey of the most essential properties of these analysers the reader is referred to tables 1 and 2.

Parallel plate analyser

In a parallel plate analyser the deflecting field is a homogeneous electric field resulting from a set of two parallel plates kept at different potentials; see fig. 20.

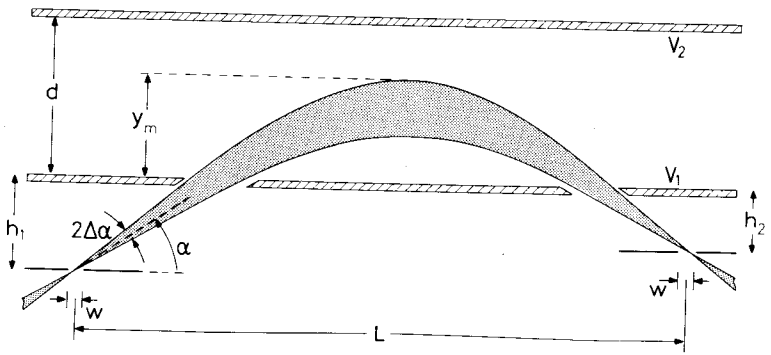

Fig. 20. Parallel plate analyser.

The potential on the top plate (V_2) is such that the particles are bent back to the bottom plate. Very generally, the analyser consists of three regions: one region in which the above mentioned (vertical) field is present (across a distance d in fig. 20) and two field-free regions below the bottom plate (V_1) in which the entrance and exit slits are located. The heights of these field-free regions are h_1 and h_2, respectively. The particle enters the analyser through the entrance slit with width w at an angle α with respect to the plates. The horizontal distance a particle travels is directly related to its kinetic energy, and therefore only particles with a specific energy will be able to leave the analyser through the exit slit. Generally we can write:

$$L = (h_1 + h_2)\cot\alpha + 2(E/\varepsilon)\sin 2\alpha\,, \tag{30}$$

in which L is the distance between the two slits, E the energy of the particle and ε the electric field strength between the plates: $\varepsilon = (V_2 - V_1)/d$. The maximum height y_m is given by:

$$y_m = (E/\varepsilon)\sin^2(\alpha + \Delta\alpha)\,. \tag{31}$$

For specific combinations of $(h_1 + h_2)$ and α there is first-order focussing ($\partial L/\partial\alpha = 0$):

$$(h_1 + h_2) = 4(E/\varepsilon)\cos 2\alpha \sin^2\alpha\,. \tag{32}$$

This focussing is one-dimensional; it takes place only in the plane perpendicular to the plates.

The historically oldest version of this type of analyser is the one in which $\alpha = 45°$ and $(h_1 + h_2) = 0$; i.e., both slits are located in the bottom plate (Pierce 1949, Harrower 1955). In that case, $L = 2(E/\varepsilon)$.

Green and Proca (1970) showed that for $\alpha = 30°$ second order focussing is obtained ($\partial L/\partial\alpha = \partial^2 L/\partial\alpha^2 = 0$) which allows the acceptance of larger opening angles $\Delta\alpha$. The horizontal distance between the slits now becomes:

$$L = \tfrac{3}{2}\sqrt{3}(E/\varepsilon) \quad \text{and} \quad (h_1 + h_2) = \tfrac{1}{2}(E/\varepsilon)\,.$$

Whenever the angular aberrations are zero up to third order, the waist or minimum width of the trace is not at the image plane but at a plane above it (Conrady 1957). Proca and Green (1970) showed that an exit slit placed at the position of this waist (i.e., h_2 becomes smaller) yields a better result. Information on the spectrometer functions is given by Aksela (1973), Roy and Carette (1971a,b) and Rayborn and Hsiao (1974).

Although the parallel plate analyser does not score high in comparison with other types of analysers (table 2), it is often used because of its relatively simple mechanical construction. Another advantage is that it is possible to apply pre-

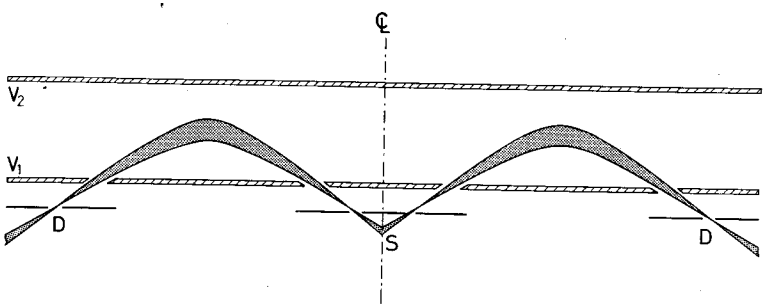

Fig. 21. Fountain analyser, a parallel plate analyser with 2π symmetry.

retardation such that the various contributions to the final energy resolution are optimized (sect. 4.2.2).

A special type of parallel plate analyser is the so-called "fountain spectrometer", characterized by circular entrance and exit slits instead of rectangular ones. In cases where point-like particle sources are present, this geometry is particularly useful in view of the much larger accepted solid angle (fig. 21). It was introduced by Edelmann and Ulmer (1965); a further description can be found in Schmitz and Mehlhorn (1972). A disadvantage of the fountain spectrometer is that it requires a very large circular area to be covered by detectors; besides that optimization via pre-retardation is not practical.

Information on fringing field effects at the entrance and exit slits of these types of analysers can be found in articles by Proca and Rüdinger (1973) and Bosi (1972). Recent examples of parallel plate analysers have been described by Smith et al. (1977), Van Veen et al. (1979) and Steckelmacher and Lucas 1979).

Cylindrical mirror analyser

The cylindrical mirror analyser (CMA) is probably the most widely used analyser in surface physics. The deflecting field is formed by two concentric cylinders with radii R_1 and R_2, kept at potentials V_1 and V_2, respectively; see fig. 22. The general electron optical properties of the analyser are the following; charged particles created at a source S enter the analyser through a circular entrance slit with radius $(R_1 - h_1)$ and width w. After passage through a field-free region with radial length h_1, the particles enter the analysing field between the two cylinders at an angle α with respect to the cylinder axis. After deflection by the electric field and passage through a second field-free region with radial length h_2 the particles are focussed onto a circular exit slit with radius $(R_1 - h_2)$. Behind this slit a detector D is located. Due to the full 2π azimuthal symmetry a large solid angle is accepted; consequently compared with other types of analysers the étendue of this analyser is large.

The distance L between the two slits is a function of the angle α, the length of the field-free regions $(h_1 + h_2)$ and the electric field strength between the cylinders (Zashkvara et al. 1966).

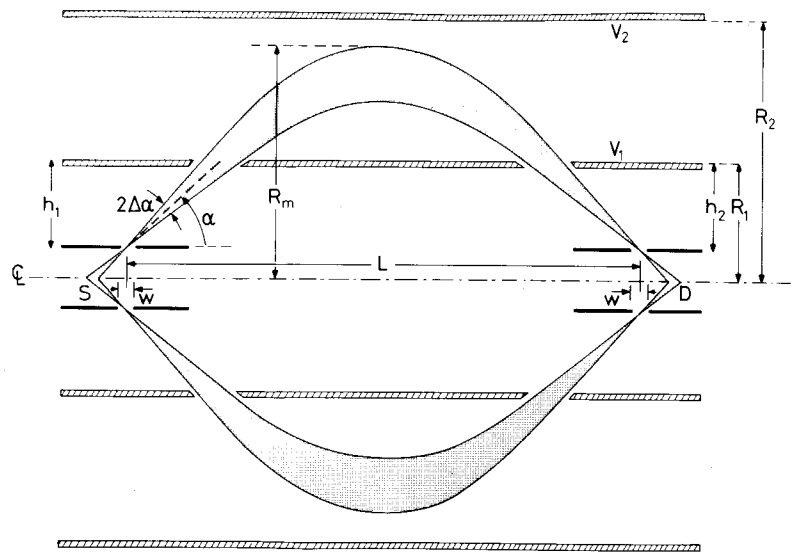

Fig. 22. Cylindrical mirror analyser (CMA). The deflecting field is generated by means of two concentric cylinders with radii R_1 and R_2.

$$L/R_1 = n \cot\alpha + 2(k\pi)^{1/2} \cos\alpha \exp(k \sin^2\alpha) \operatorname{erf}(k^{1/2} \sin\alpha), \tag{33}$$

in which

$$n = (h_1 + h_2)/R_1\,, \tag{34}$$

and

$$k = \frac{E}{q(V_2 - V_1)} \ln(R_2/R_1)\,. \tag{35}$$

In this expression E is the initial kinetic energy of the particle. k is related to the electric field strength ε in the region between the two cylinders:

$$\varepsilon = \frac{(V_2 - V_1)}{r \ln(R_2/R_1)}, \quad \text{where } r \text{ is the radial coordinate} \tag{36}$$

$R_1 \leqslant r \leqslant R_2$ (see fig. 22) and $\operatorname{erf}(k^{1/2} \sin\alpha)$ is the error function (Abramowitz and Stegun 1970):

$$\operatorname{erf}(x) = \frac{2}{\sqrt{\pi}} \int_0^x \mathrm{e}^{-t^2}\,\mathrm{d}t\,.$$

For "complete" cylinders, i.e., with full 2π azimuthal symmetry n can have any value between 0 and 2; for cylinders covering an azimuth less than 2π, say half cylinders, n can have any value up to infinity (Risley 1972). We will not consider the latter case any further.

The dispersion D (eq. (25)) is independent of n:

$$D/R_1 = k \sin 2\alpha + k^{3/2}\pi^{1/2} \cos\alpha \exp(k \sin^2\alpha) \times \operatorname{erf}(k^{1/2} \sin\alpha)(k^{-1} + 2\sin^2\alpha) . \quad (37)$$

The maximum penetration of the particles into the deflecting field is given by (fig. 22):

$$R_m/R_1 = \exp[k \sin^2(\alpha + \Delta\alpha)] . \quad (38)$$

The first cylindrical mirror analyser to be built had $n = 0$; i.e., both slits were located in the inner cylinder ($n = 0$, $k = 1$, $\alpha = 54.5°$, $L/R_1 = 2.85$, $D/L = 1.55$ (Blauth 1957, Mehlhorn 1960). For $n = 2$ both slits are contracted to small circular apertures on axis.

The parallel plate analyser treated in the previous section is a limiting case of the cylindrical mirror analyser (R_1, $R_2 \to \infty$). The main differences between the two types of analysers are the following. The CMA has two-dimensional focussing, i.e., a point source is focussed to a point image. The parallel plate only has one-dimensional focussing. Besides that the CMA has three independently variable parameters (n, α, k), whereas the parallel plate analyser has only two ($h_1 + h_2$, α). This facilitates the optimization of the device.

Because one degree of freedom is always lost by demanding first order focussing ($\partial L/\partial\alpha = 0$), two remain for the fulfillment of other requirements:

For a fixed geometry (n) one can require second-order focussing ($\partial^2 L/\partial\alpha^2 = 0$). Examples are:

Axis to axis geometry: ($n = 2$), this leads to probably the most well-known type of CMA: $n = 2$, $\alpha = 42.3°$ and $k = 1.31$ (Zashkvara et al. 1966, Roy and Carette 1971a,b, Sar-El 1967, Eagen and Sickafus 1977). In this case $L/R_1 = 6.13$ and $D/L = 0.91$. For the base energy resolution of this type and the other analysers mentioned in this section we refer to eq. (26) and table 1.

Ring to axis geometry: $n = 1$, $\alpha = 38.8°$ and $k = 0.94$ (Zashkvara et al. 1971). This leads to $L/R_1 = 3.60$ and $D/L = 0.83$. This geometry has the experimental advantage of free access to the interior of the inner cylinder (Harris 1974).

Ring to ring geometry: $n = 0$, $\alpha \simeq 31°$ and $k \simeq 0.2$. Aksela et al. (1970) showed that in this case also the third order aberration coefficient $\partial^3 L/\partial\alpha^3$ reaches a minimum value close to zero. However, the dispersion becomes too small for this analyser to be of any practical use.

In case the source has non-negligible radial dimensions the velocity vector component out of the axial plane becomes important. Aksela (1972) showed that the decrease of the resolving power due to this effect can be minimized by a proper choice of the parameters: A first-order focussing example of this is the case: $n = 0$, $k = 1.25$, $\alpha = 56.5°$, $L/R_1 = 3.92$ and $D/L = 1.77$.

Risley (1972) gives graphical and tabular information on a large number of (other) combinations of the parameters n, α and k yielding first- and second-order focussing, respectively.

As in all other analysers with second-order focussing there is a position at a radius larger than that of the exit slit where the trace width has a minimum. Depending on $\Delta\alpha$, the size of this waist can be a factor 2 to 4 smaller than the image size. Its position and width are given by Sar-El (1970). At the waist the base width of the energy distribution is smaller than at the image. However, the halfwidth of the distribution usually is larger. This is due to the peculiar shape of the distribution function at the waist (Aksela 1971, 1972). For larger opening angles $\Delta\alpha$ and larger source dimensions the energy distributions at the waist and at the image become similar and the advantage of a slit located at the waist position disappears.

A very practical contribution in this field is given by Draper and Lee (1977). They give spectrometer functions and comparative tables for a large number of different analysers based on numerical trajectory calculations. For seven values of the angle α ($30° \leqslant \alpha \leqslant 65°$) and three analyser geometries ($n = 1$, 1.5, 2) the luminosity is given for source, slits and detector dimensions optimized such that the same relative resolution of 8×10^{-4} is obtained in all cases. The general conclusion which can be drawn is that a large angle is favourable for a good result. However for $\alpha > 60°$ the ratios R_2/R_1 and L/R_1 become unpractically large. A practical limit possibly is $\alpha = 60°$; then $R_2/R_1 \approx 5$ and $L/R \geqslant 10$, more or less independent of n. Therefore, for comparison the case $n = 2$, $k = 2.06$ and $\alpha = 60°$ is also given in table 1 ($L/R_1 = 11.3$ and $D/L = 2.16$). Draper and Lee show that although for angles $\alpha > 42.3°$ only first-order focussing can be realized the result can still be comparable or even superior to that of second-order focussing devices, especially for opening angles $\Delta\alpha \leqslant 2°$ (Risley 1972). This is due to the larger dispersion which is attained for large α. A detailed description of an $\alpha = 60°$ CMA is given by Citrin et al. (1972); it includes details on the mechanical construction.

As for fringing fields, usually grids are placed in the slits in the inner cylinder (fig. 22) to minimize their influence. This has certain disadvantages due to the loss in transmission and the possible creation of secondary electrons (sect. 4.3). Vašina and Frank (1979) considered the lens action at the slit of a gridless CMA (compare with the Calbick lens, sect. 3.3.1). For further information dealing with fringing fields, see Renfro and Fischbeck (1975) and Bosi (1972). Sometimes pre-retardation is applied by means of cylindrical grids placed between the source and the inner cylinder slit. However, no accurate focussing is possible in this way and it leads to additional transmission losses.

In some experiments two CMAs are applied in series. This leads to a much better source definition. If for instance $n = 2$ CMAs are used (Palmberg 1974) then particles emerging from off-axis source points can still pass the exit slit of the first CMA for specific deviations $\Delta\alpha$ and/or ΔE. However, such particles are rejected by the second CMA. This double CMA set up may be advantageous for those experiments where the particles are produced by extended X-ray sources or electron beams. Besides that the number of reflected particles and secondary electrons reaching the exit slit is strongly reduced (sect. 4.8).

Spherical deflection analyser

In the spherical deflection analyser, first investigated by Purcell (1938), the deflecting field is formed by two concentric spherical surfaces with radii R_1 and R_2 kept at potentials V_1 and V_2, respectively (fig. 23). The central trajectory (dashed line in fig. 23) is a circle; its radius of curvature R_0 is taken as the characteristic dispersive length (L). The radial electric field ε_r between the spherical surfaces is given by:

$$\varepsilon_r = (V_2 - V_1)R_1R_2/r^2(R_2 - R_1)\,. \tag{39}$$

The pass energy of the analyser, i.e., the energy of the particles travelling along the central trajectory, is:

$$E_0 = q(V_2 - V_1)/(R_2/R_1 - R_1/R_2)\,. \tag{40}$$

The spherical analyser has two-dimensional focussing, i.e., a point source O placed at a certain distance P' from the entrance plane of the analyser is focussed in a point image I located at a distance Q' from the exit plane (fig. 23). The focal properties can be characterized by two focal and two principal planes; see fig. 24. The position of these planes is given by the relations:

$$f = R_0/\sin\Phi\,, \qquad F = R_0\cot\Phi\,. \tag{41}$$

The position of object and image are related via:

$$(P' - F)(Q' - F) = f^2\,. \tag{42}$$

It can be shown that the centre of curvature C, the object O and the image I are lying on a straight line. Further use of the quantities mentioned in eqs. (41) and (42) is given in sect. 3.2.1 (eqs. (4)–(7)).

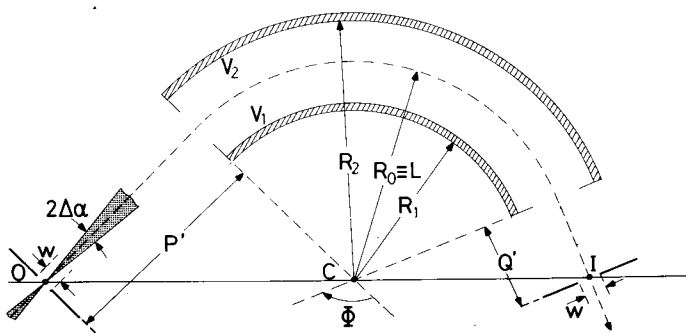

Fig. 23. General diagram for spherical and cylindrical deflection analysers with arbitrary sector angle Φ. In a spherical analyser the deflection field is due to two concentric spheres (radii R_1 and R_2); in the cylindrical analyser to two concentric cylinders (radii also R_1 and R_2).

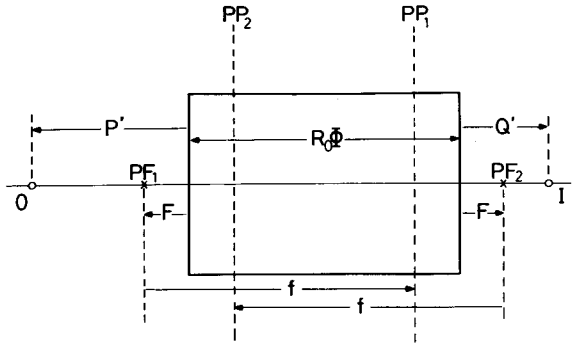

Fig. 24. The location of focal and principal planes (points) of spherical and cylindrical deflection analysers with arbitrary sector angle Φ. $R_0\Phi$ is the length of the particle trajectory in the analysing field. The object and image distances P' and Q' and the lengths F are defined with respect to the entrance and exit planes of the deflecting fields, see figs. 23. and 3(a).

The most well-known example of this class of analysers is the 180° spherical deflection analyser ($\Phi = 180°$). In that case the object and image points are located in the entrance and exit planes of the analyser; see fig. 25. The maximum excursion of the particles is given by:

$$R_m = R_0(1 + \Delta\alpha)\,. \tag{43}$$

The base energy resolution of this device can be deduced from eq. (26) and table 1. For optimization of the halfwidth resolution with respect to the angular aberration and slit terms (eq. (29)) one can use eq. (28). This relation was confirmed to be accurate within 20% by Polaschegg (1976) and Poulin and Roy (1978). In the latter paper a comparison is given between various quality factors introduced by a number of authors. For further information on the spectrometer function see Roy and Carette (1971a,b) and Chase (1973).

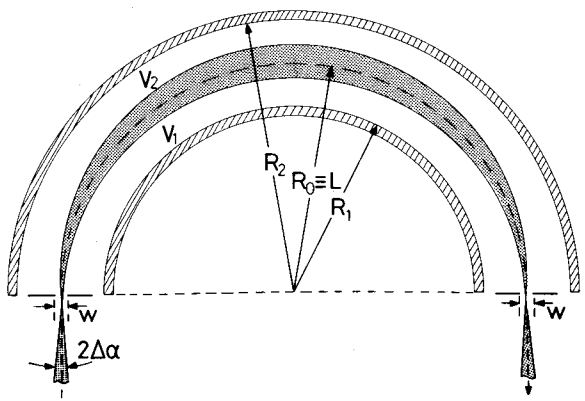

Fig. 25. The hemispherical (180°) deflection analyser.

This type of analyser is widely used for the production and analysis of well-defined particle beams. Therefore pre-retardation is a good technique to optimize the performance (Nöller et al. 1974, Heddle 1971b, Polaschegg 1974). It should be realized that the entrance optics have to be designed such that the beam angle (see sect. 2) is zero at the entrance slit of the analyser. If this is not the case the effective opening angle $\Delta\alpha$ ($=\theta_B+\frac{1}{2}\alpha_i$ in fig. 1) is larger than strictly necessary ($=\frac{1}{2}\alpha_i$). This will increase the spherical aberration of the device and consequently reduce the resolving power.

In a 180° analyser an entrance beam angle equal to zero leads to an exit beam angle also zero. From eqs. (41) and (42) it can be deduced that for $\Phi \neq 180°$ this is not the case.

For the minimization of fringing field effects the well-known Herzog correction is often applied (Herzog 1935, 1940). Elaborate practical applications of this correction are given by Wollnik and Ewald (1965). For further information on fringing field effects see Sköllermo and Wannberg (1975) and Jost (1979).

Imhof et al. (1976) studied the time resolution of this type of analyser. It appears that good energy resolution and good time resolution, which is important in coincidence experiments (sect. 7), are conflicting requirements.

Good examples of spherical deflection analysers in which some or most of the above mentioned features are applied are the following:

Simpson (1964), Kuyatt and Simpson (1967) and Chutjian (1974, 1979) used 180° analysers with $R_0 = 2.54$ cm. Brunt et al. (1977) with $R_0 = 5$ cm and Thomas and Weinberg (1979) with $R_0 = 7.6$ cm. Kuyatt and Plummer (1972) describe a 135°, $R_0 = 2.54$ cm device. One of the largest analysers probably is the one used for ESCA studies in Uppsala (Gelius et al. 1974): $R_0 = 36$ cm, $\Phi = 157°$ and $\Delta E/E = 5 \times 10^{-4}$. Finally it should be mentioned that also examples exist with 2π azimuthal symmetry (2π rotation about the line OCI in fig. 23); see Poole et al. (1972), Kemeny et al. (1972) and Moore et al. (1978). The solid angle which can be accepted now becomes comparable to that of the cylindrical mirror analyser.

Cylindrical deflection analyser

The deflecting field in a cylindrical deflection analyser is created by means of two cylindrical surfaces with radii R_1 and R_2 at potentials V_1 and V_2, respectively (fig. 26). The radius of curvature R_0 of the central ray (dotted line in fig. 26) is chosen as the characteristic dispersive length L. The radial electric field is given by:

$$\varepsilon_r = (V_2 - V_1)/r \ln (R_2/R_1), \tag{44}$$

and the pass energy of the analyser,

$$E_0 = q(V_2 - V_1)/2 \ln(R_2/R_1). \tag{45}$$

The cylindrical deflection analyser has one-dimensional focussing in the plane of the drawing (fig. 26). A point source O located at a distance P' from the entrance plane is focussed in a line image I at a distance Q' from the exit plane

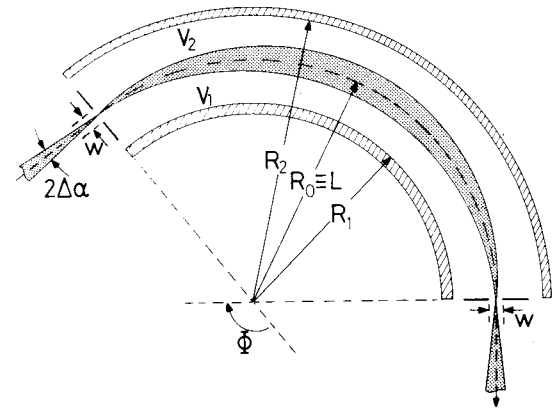

Fig. 26. The 127° cylindrical deflection analyser.

(see fig. 23; note that in this case O, C and I are *not* on a straight line). The focal properties are characterized by eq. (42) in combination with the relations (fig. 24):

$$f = R_0/\sqrt{2} \sin(\sqrt{2}\,\Phi), \qquad F = R_0 \cot(\sqrt{2}\,\Phi)/\sqrt{2}. \tag{46}$$

For $\Phi = \pi/\sqrt{2} = 127°$ the source and image are located at the entrance and exit planes of the analyser (fig. 26). This geometry, for obvious reasons often called the 127° analyser is the most well-known example of the cylindrical deflection analysers. In this type the maximum excursion R_m of the particles is given by:

$$R_m = R_0(1 + \Delta\alpha/\sqrt{2}). \tag{47}$$

The base energy resolution can be deduced from eq. (26) in combination with table 1. Relation (28) can be used for the optimization of the angular aberration term with respect to the slit term. The validity of this relation has been confirmed by accurate numerical trajectory calculations (Roy and Carette 1971a, Roy et al. 1974).

The properties of the cylindrical deflection analyser were first investigated by Hughes and Rojanski (1929). Theoretical papers dealing with the various properties of this analyser are those of Paolini and Theororidis (1967), Arnow and Jones (1972), Johnstone (1972) and Delgate and Carette (1971). A description of an experimental system yielding $\Delta E = 20$ meV, including entrance optics and fringing field corrections is given by Roy et al. (1974); see also Froitzheim and Ibach (1974).

As in the case of the spherical deflection analyser the Herzog fringing field correction can be applied (Herzog 1935, 1940, Wollnik and Ewald, 1965); see also Jost (1979).

Although this type of analyser does not score very high in the comparative table 2, it has the advantage of a very simple mechanical construction. This is the reason why it is widely used.

Toroidal deflection analyser

The spherical and cylindrical deflection analysers are both special cases of the general toroidal analyser. In a toroidal analyser the surfaces have different radii of curvature in the plane of the particle trajectory and in the plane perpendicular to it. In principle this leads to an additional degree of freedom in the design. The focussing properties of this device are given by Ewald and Liebl (1955). Information on the aberration coefficients (eq. (26)) can be found in an article by Wannberg et al. (1976).

4.2.4. Magnetic analysers

The first types of charged particle analysers used in atomic and molecular physics were almost all magnetic deflection analysers. This is due to the fact that the magnetic instrument had already reached a high degree of perfection in the older field of beta-ray spectroscopy.

However, as the energies of the particles to be analysed became lower and lower, the usefulness of magnetic analysers decreased. Low-energy analysis, especially of electrons requires very stringent shielding against stray magnetic fields.

Iron-core instruments are not practical in this respect; the magnetic spectrometer in use nowadays usually are iron-free. In most cases they have a $1/\sqrt{r}$ field and two-dimensional focussing after a deflection angle $\pi\sqrt{2}$. However, even in this configuration high resolution low-energy electron spectroscopy requires large Helmholtz coils for the reduction of external fields; μ-metal shields can usually not be applied for this purpose.

For these reasons most modern charged particle analysers apply electrostatic fields. Extensive reviews of the properties of magnetic analysers are those of Siegbahn (1965), Sevier (1972) and Fadley et al. (1972).

To enable the reader to make a basic comparison between electrostatic and magnetic deflection analysers we will very shortly treat some properties of the general magnetic sector field (fig. 27). The focussing properties of such a magnetic sector are governed by the eqs. (41) and (42). For a perpendicular entrance and exit of the beam into the sector field the focussing is one-dimensional. As in the case of the spherical deflection analyser the object O, the image I and the centre

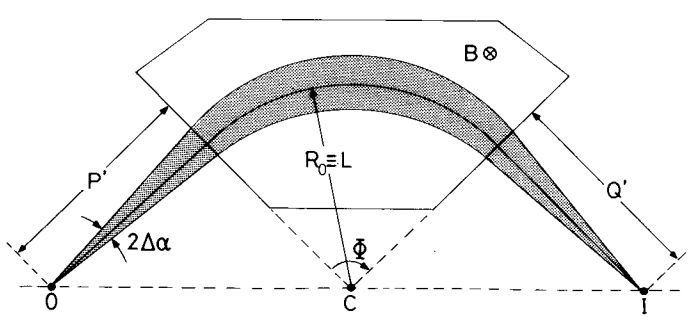

Fig. 27. Magnetic sector field with sector angle Φ.

of curvature C are located on a straight line. The base energy resolution is given by eq. (26) and table 1. It should be mentioned that by choosing the entrance and exit angles in a specific way astigmatic focussing can be obtained.

Magnetic fields are still widely used for mass analysis. Because this is a large (and old) field about which many good books and reviews have been written in the past, we will not treat this here; see for example, Farmer (1963) and Dickworth and Ghoshal (1963).

4.2.5. Analysers with crossed electric and magnetic fields

When electrostatic as well as magnetic fields are applied, the charged particle is subjected to two forces simultaneously. The total force $\boldsymbol{F}$ then becomes:

$$\boldsymbol{F} = m(\mathrm{d}\boldsymbol{v}/\mathrm{d}t) = q(\boldsymbol{\varepsilon} + \boldsymbol{v} \times \boldsymbol{B}), \tag{48}$$

where m and q are the mass and the charge of the particle and $\boldsymbol{\varepsilon}$ and $\boldsymbol{B}$ the electric and magnetic field strengths, respectively. $\boldsymbol{v}$ is the particle velocity. Equation (48) shows that the motion of the particles depends on their velocity. For specific orientations and magnitudes of $\boldsymbol{\varepsilon}$, $\boldsymbol{B}$ and $\boldsymbol{v}$ this effect is optimal for energy (and mass) analysis. Two examples are the Wien filter analyser and the trochoidal analyser. In both cases the electric and magnetic fields are mutually perpendicular.

Wien filter analyser

In a Wien filter analyser the charged particle is injected into the device in a direction perpendicular to both electric and magnetic field (fig. 28). The strengths of both fields are chosen such that for one particular velocity v_D the total force is

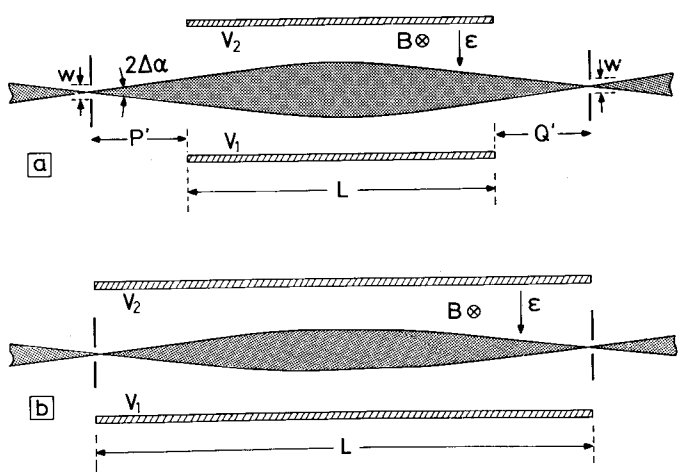

Fig. 28. Wien filter analyser. $\boldsymbol{\varepsilon}$ and $\boldsymbol{B}$ stand for (crossed) electric and magnetic fields. (a) General case with arbitrary length of the filter. (b) Filter in which a slit placed at the entrance boundary of the fields is imaged on a slit at the exit boundary.

zero, i.e., the particle trajectory is straight. According to eq. (48) this is the case when:

$$v_D = \varepsilon/B\,. \tag{49}$$

Particles with a velocity different from this velocity v_D are deflected from the straight line trajectory. Hence a Wien filter essentially has velocity dispersion. If the particles to be analysed have the same mass, one can use this effect for energy analysis. Alternately for particles with the same energy it leads to mass separation.

In the dispersive plane, i.e., the plane containing the particle trajectories and the electric field vector there is focussing; i.e., for a suitable combination of P', Q' and L (fig. 28(a)): $\partial x_2/\partial\alpha = 0$. The position of the focal and principal planes characterizing this focussing is given by (figs. 24 and 28(a); in fig. 24 $R_0\Phi$ has to be replaced by L):

$$f = \frac{v_D}{\omega}\left(\sin\frac{\omega L}{v_D}\right)^{-1}, \qquad F = \frac{v_D}{\omega}\cot\frac{\omega L}{v_D}\,. \tag{50}$$

The position of object and image is governed by eq. (42). In eq. (50) v_D is given by eq. (49); ω is the cyclotron frequency given by $\omega = qB/m$. For further use of the equations see sect. 3.2.1. The most well-known Wien filter is the one in which $L = \pi v_D/\omega$. The slits are then located at the entrance and exit boundaries of the fields (see fig. 28(b)). In that case the spherical aberration coefficient C_α has a minimum (Andersen 1967). Besides that a beam entering the device with a beam angle zero also leaves it with zero beam angle (sect. 2). This is not the case for shorter or longer filters. The base energy resolution of the filters with $L = \pi v_D/\omega$ and $L = \pi v_D/2\omega$ can be deduced from eq. (26) and table 1. Note that $\Delta m/m = \Delta E/E$.

The advantage of a Wien filter is the straight trajectory of the particles and the simple construction. When electrons are analysed, coreless coils usually suffice. For this case Anderson (1967) described an inhomogeneous magnetic field to correct second order spherical aberrations. High resolutions (25 meV) have been obtained by Boersch et al. (1964) and Andersen and Le Poole (1970). Galeys and Kuyatt (1978) and Collins (1973) showed that two-dimensional focussing is obtained when the uniform magnetic field is replaced by a toroidal one.

Trochoidal analyser

In the trochoidal analyser the particles, mostly electrons, are injected parallel to the magnetic field (fig. 29). Due to the combined electric and magnetic forces (eq. (48)) the particles describe trochoidal trajectories (Stamatovic and Schulz 1970). The strength of the magnetic field is chosen such that the cyclotron period ($\omega^{-1} = m/qB$) is much smaller than the passage time from entrance to exit slit; besides that the "radius" of the trochoidal orbit is much smaller than the characteristic dimensions of the analyser. This means that it suffices to consider

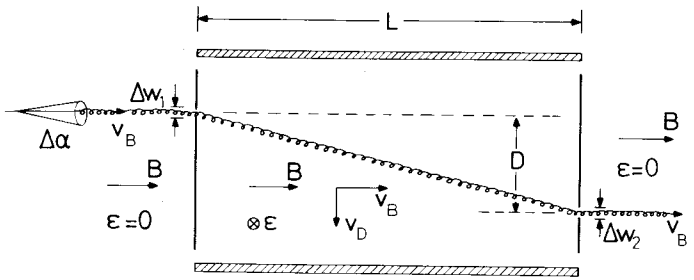

Fig. 29. Trochoidal analyser. $\boldsymbol{\varepsilon}$ and $\boldsymbol{B}$ stand for (crossed) electric and magnetic fields. v_B and v_D are the beam and the drift velocity, respectively. $\boldsymbol{\varepsilon} = 0$ outside the analyser; $\boldsymbol{B}$ is present everywhere, i.e., from target to detector.

only the guiding centre motion; i.e., to average over the trochoidal motion. Note that in the Wien filter this is not allowed. The trajectory of a particle is now determined by two constant velocities: a velocity v_B along the magnetic field lines, equal to the initial velocity in that direction and a $(\boldsymbol{\varepsilon}\times\boldsymbol{B})$ guiding centre drift velocity $v_D = \varepsilon/B$. v_D is perpendicular to the electric as well as the magnetic field (Chen 1976) and hence causes a deflection from the initially straight line trajectory. If the device has a length L then the deflection D is given by: $D = v_D L/v_B$. Because v_D is independent of the particle energy and mass the deflection D is inversely proportional to the velocity of the particle at the entrance side of the analyser. For the analyser pass energy one can derive:

$$E = (\varepsilon L/BD)^2\, m/2q\,. \tag{51}$$

In first approximation the base energy resolution is given by (Roy 1972):

$$\Delta E_B/E = 2(\Delta w_1 + \Delta w_2)/D + 2(\Delta\alpha)^2 + \varepsilon\Delta w_1/E\,. \tag{52}$$

In eq. (52) the first and second terms on the right-hand side give the contribution to the energy resolution due to the aperture diameters and the opening angle of the beam with respect to the $\boldsymbol{B}$-field direction (fig. 29). The third contribution to the energy spread is caused by the potential drop $\varepsilon\Delta w_1$ across the entrance aperture. This last term usually has the largest influence on the resolution.

For proper operation of the device the uniform magnetic field extends from the particle source in front of the analyser to the particle detector behind the analyser. For applications in which one is interested in the energy spectrum of electrons, this analyser is a good candidate. The large magnetic field confining and guiding the particles makes operation at energies well below 1 eV possible.

The energy distribution of particles emerging from this type of analyser has been calculated by Roy (1972). Roy and Burrow (1975) and Langendam (1978) used this analyser in a 180° backscattering spectrometer. From these papers it is clear that the trochoidal analyser may be very useful in fields such as ultraviolet photoemis-

sion spectroscopy. Tam and Wong (1979) described a system in which a trochoidal analyser was combined with a magnetic filter; this filter preferentially stops electrons with large transverse energies. This increases the resolving power of the analyser.

4.3. Retarding potential analysers

One of the oldest methods to determine the kinetic energy of a charged particle is to apply a retarding electrostatic field at the particle collector. In principle all particles with an energy larger than the potential barrier can reach the collector. A variation of the potential difference between particle source and collector leads to an integrated energy spectrum. By differentiating the result with respect to the retarding potential, one obtains the spectrum itself. This idealized picture is shown schematically in fig. 30(a). In such a set-up, in which the entrance aperture usually is replaced by a high-transmission grid, particles with an energy larger than eV_R will reach the collector and in principle contribute to the measured current. However, reflected particles and secundary electrons (provided these are

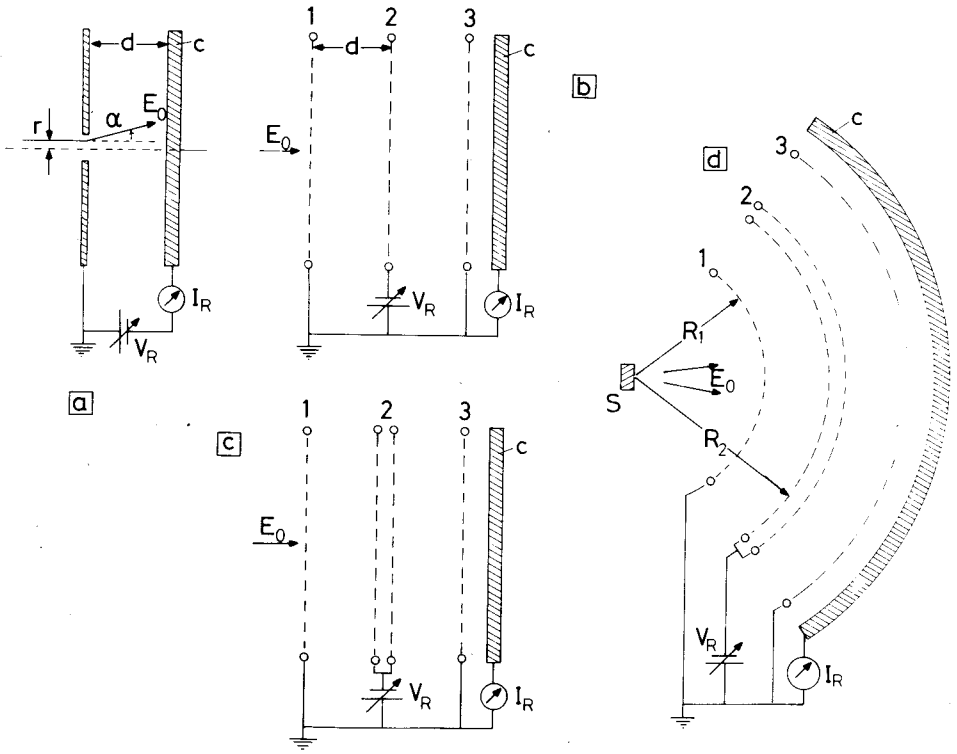

Fig. 30. Retarding potential analyser arrangements. (a) Simplest set-up with retarding field between an entrance plate with aperture and collector plate. (b) Three-grid arrangement with single retarding grid (2). (c) Four-grid arrangement with double retarding grid (2). (d) Spherical four-grid system.

created by negatively charged incoming particles) will be accelerated away from the collector surface, leading to erroneous results. A possible way to prevent this is to shield the retarding field from the collector by means of grids (fig. 30(b)). The particle is energy analysed by a retarding field between grids 1 and 2 and reaccelerated between grids 2 and 3. Collector C can be biased with respect to grid 3 to ensure that all particles are collected.

There are several effects which influence the measured energy resolution.

First of all the potential in the plane of grid 2 in fig. 30(b) is not equal to V_R everywhere. In between the grid wires the potential is lower due to the influence of grids 1 and 3. For example a mesh at potential V with 100 wires per inch of thickness 0.025 mm, placed between two grounded grids each at a distance of 6.35 mm, gives a potential difference between the wires and the centre of a grid aperture: $\Delta V/V \approx 2\%$ (Taylor 1969). This of course directly limits the minimum obtainable energy resolution. A solution to this problem is to replace the retarding grid by a set of two grids, both at the same potential; see fig. 30(c). Taylor (1969) showed that in his case the addition of this extra grid improved the resolution from 2.4 to 0.3%.

A more basic drawback which affects the energy resolution is that not the total kinetic energy is determined but the particle momentum perpendicular to the potential lines. If a particle with energy E_0 and charge q enters the retarding field with an angle α with respect to the field lines a potential barrier with a height $(E_0 \sin^2 \alpha)/q$ suffices to reflect the particle. If the particle beam to be analysed has an angular distribution with halfwidth $\Delta\alpha$ the corresponding broadening of the energy distribution is (Simpson 1961):

$$\Delta E_B/E = \sin^2 \Delta\alpha \,. \tag{53}$$

For this reason the shape of the grids has to be adapted to the experimental situation. Plane grids are used for large particle sources from which the particles are emitted with small opening angles. The opposite situation is more frequently encountered: Small particle source and large opening angles. In that case a spherical grid system is to be preferred over a plane one; see fig. 30(d).

The angle α is influenced by more effects than only the particle source characteristics: because the particle leaves a field-free region and enters a region with field, the aperture in fig. 30(a) acts as a (negative) Calbick lens (sect. 3.3.1). When gridded planes are used each of the meshes acts as a separate lens. Although these lenses are ill-defined and the Calbick formalism is only applicable for paraxial trajectories, i.e., for trajectories far away from the wires of the grid or the edge of the aperture, we assume that in first approximation this treatment is sufficiently accurate to give some insight in the magnitude of the effects. In case of an aperture the focal length is: $f = -4\,d$ (eq. (15) for particles having threshold energy; d is the distance between the aperture and the collector plate). Hence a particle entering the field perpendicular to the entrance plate after passing through the entrance aperture at a radius R_A will have an angle $\alpha \approx \mathrm{tg}\,\alpha = R_A/4d$. Consequently an aperture with diameter a_1, or a grid with mesh size a_1 leads to a

limiting energy resolution $\Delta E_B/E = \sin^2(a_1/8d) \approx a_1^2/64\,d^2$. It is clear that for $a_1 \leqslant 0.1\,d$ this contribution is negligible.

Equation (15) also shows that the lens action at grid 2 is positive and much stronger than that at grid 1; the energy of the particles approaches zero and hence the focal length of the lens becomes vanishingly small. Therefore eq. (15) is of no use anymore. In this case the energy resolution has to be obtained from numerical trajectory calculations. For a given combination of mesh size a_2 and retarding field strength ε_R, the energy resolution can be deduced from the calculated transmission versus particle energy curves. Such theoretical curves are given by Hutchital and Rigden (1972a,b), Staib (1972a,b) and Staib and Dinklage (1977). Staib (1972a) showed that 50% transmission is obtained for an energy shift ΔE from threshold where $\Delta E_{0.5}\,(\text{eV}) = 0.05\,\varepsilon_R a_2$, i.e., a retarding field strength of 1 V per unit a_2 leads to $\Delta E_{0.5} = 50$ meV. Figure 31 shows the result of a two-dimensional trajectory calculation (grids consisting of only vertical wires, Hutchital and Rigden (1972a)). It shows the strong positive lens action and the large aberrations for trajectories close to the wires.

Also stray magnetic fields will influence the trajectory of the particles and thus the angle α with respect to the electric field. In case of parallel particle trajectories initially perpendicular to plane grids the magnetic field will curve all trajectories in the same way; this leads to a shift in apparent energy. However, if the particles move at different angles with respect to the magnetic field lines, as is the case in the spherical grid system, the curvature of the trajectories is different for different angles; this leads to a broadening of the energy distribution. Hutchital and Rigden (1972b) calculated the magnetic field induced base resolution $\Delta E_{B,Mag}$ in a spherical grid system. It is shown that a minor shielding against magnetic stray fields usually sufficies (e.g., $\Delta E_{B,Mag} \approx 50$ meV for $B = 100$ mG; $\Delta E_{B,Mag}$ scales with B^2).

Compared with the deflection type analysers the spherical retarding potential analyser has some distinct advantages and disadvantages. It has a very large luminosity; the solid angles which are accepted are at least as large and usually

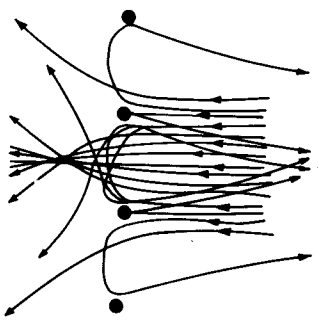

Fig. 31. Numerically calculated trajectories of 500.5 eV particles in a 500 V/inch retarding field between two one-dimensional grids (one inch apart) (i.e., wires perpendicular to the plane of the drawing). The region right from the grid shown in the figure is assumed to be field-free (from Hutchital and Rigden (1972a)).

larger than those accepted by for instance the cylindrical mirror analyser (sect. 4.2.3). Besides that the source area can be made appreciably larger than that of the deflection analysers. Equation (53) shows that a source with diameter d_S ($d_S \ll R_1$ (see fig. 30(d)) leads to a broadening of the energy distribution such that $\Delta E_B/E \approx d_S^2/4R_1^2$. This means that one can allow source diameters much larger than those in deflection type analysers. The resolution is linearly instead of quadratically dependent on the slit size: $\Delta E_B/E \propto w/R_0$ (or w/L, see eq. (26)). This also means that the alignment of the source with respect to the analyser is much less critical in the retarding analyser.

The retarding potential analyser is capable of a high resolution. Hutchital and Rigden (1972a,b), Goto and Ishikawa (1972) and Staib and Dinklage (1977) showed that for electron energies of 500–1000 V resolutions of the order of 0.1% are attainable.

The disadvantages of the retarding potential analyser are two-fold. First of all the measurement integrates over all energies above a preset value. This means that the (shot) noise level is much higher than in the case of the deflection type analysers. This makes it essential to modulate the retarding potential and to apply lock-in techniques. For details about these techniques, see Taylor (1969) and Golden et al. (1972). Besides that, the creation of large amounts of secondary electrons on the grids has an obscuring effect on the measurement (Wei et al. 1969). These effects make the signal to noise ratio of retarding potential analysers usually worse than that of the deflection analysers. They are, however, very useful in cases of large sources. Besides that, if a LEED set-up (fig. 30(d)) is required for the analysis of a target surface, it is advantageous to use this set-up also for photoelectron and Auger spectroscopy.

A way to circumvent the problem related to the high pass character of the analyser is the following: The particles in which one is mostly interested are those passing the grid with very little energy. Now suitably chosen small electric fields can be applied such that these low-energy particles are bent back to the axis of the system whereas the trajectories of the higher energy particles are much less influenced by this field. By placing a small collector on the axis one discriminates against higher energy particles and consequently the high pass filter becomes a band pass filter. In this way advantageous features of retarding potential and deflection type analysers are combined. In fig. 32 two of those arrangements are shown: in the set-up of Hutchital and Rigden (1972a,b), fig. 32(a), the focussing field is generated by applying a small potential on the circular suppressor grid. In fig. 32(b) the set-up of Staib (1972a) is shown. Here the low-energy particles are focussed to the axis by a set of two spherical grids, generating a radial electric field. In both cases, however, a high background is still present. Harris et al. (1975) compared both types experimentally. The Hutchital–Rigden set-up was found to be superior, probably because of the presence of fewer grids, see also Lindau et al. (1973). However, recently, Staib and Dinklage (1977) described an improved version of the Staib type analyser. Apart from the band pass character which is obtained in this way, an additional advantage is that the collector size is small enough to apply normal size particle multipliers.

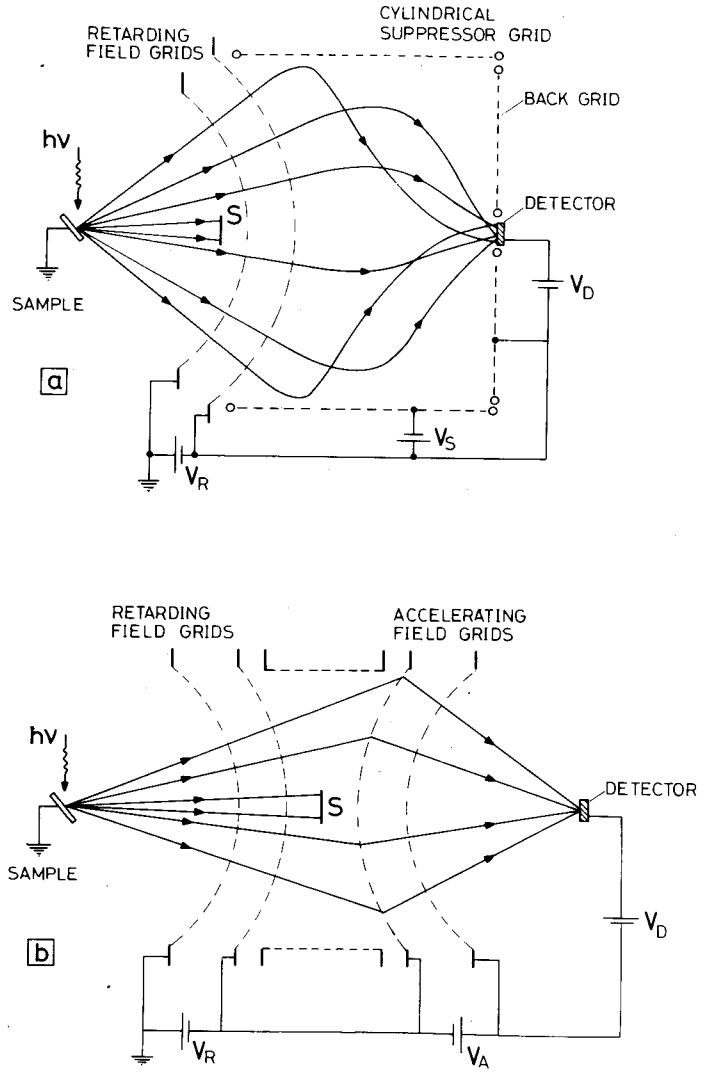

Fig. 32. Two so-called post-monochromator arrangements. Particles passing the retarding field grids with little energy are preferentially reflected to a detector placed on axis. (a) Hutchital and Rigden set-up. (b) Staib set-up.

A third way to obtain a band pass retarding potential analyser is to apply a combination of two retarding fields, in which one is used in reflection and the second in transmission. Lee (1972, 1973) and Eastman et al. (1980) obtained good results with such a set-up.

Another class of retarding potential analysers is the so-called filter lens. In principle a filter lens consists of an einzel lens (see sect. 3), in which the central element is operated in a strongly decelerating mode. Particles with an energy below a certain preset value are reflected in this central element. Because such a strongly decelerating lens system is highly chromatic (see sect. 2.4), particles with an energy higher than the preset value are focussed back to the axis with large aberrations and consequently are smeared out in space. In case an exit aperture is used only particles with an energy within a small band are focussed on the aperture correctly and thus the high-energy component of the beam is attenuated. This effect becomes very strong when the entrance and exit apertures are placed off-axis. Usually such a filter system consists of more than three elements; often a combination of cylinder and aperture lenses is used (Simpson 1961, Simpson and Marton 1961, Kessler and Lindner 1964, Zeman et al. 1971).

Finally it should be mentioned that it is also possible to apply the retarding potential technique in an axial magnetic field. See for example: De Jagher et al. (1974), Hsu and Hirschfeld (1976) and Hopman et al. (1977).

4.4. *Quadrupole analysers*

A quadrupole mass filter uses an arrangement of electrodes identical to that of the quadrupole lens (fig. 10). For the excitation of the filter an RF voltage is added to the DC voltages on the two pairs of rods. The principle of the filter is to create a field with the following characteristic:

$$V(x, y, t) = cA \cos \omega t (x^2 - y^2) + V_{DC}\,, \tag{54}$$

where c is a constant, and A and ω are the amplitude and frequency of the RF voltage, respectively. In a field of this kind only ions of a specific m/e have a stable oscillatory trajectory along the z-axis, given by (for $V_{DC} = 0$):

$$m/e = cA/\omega^2\,, \tag{55}$$

while all other ions have trajectories with increasing amplitude. Mass selection is performed by scanning either A or ω.

The field prescribed by eq. (54) is usually approximated rather closely by the use of cylindrical rods, as was pointed out already in sect. 3.2.2. The DC voltage can be varied in order to trade off sensitivity and mass resolution; the lower the DC voltage, the higher the sensitivity.

Being versatile, fast scanning and sensitive devices (large opening angle), quadrupole filters are generally used in routine applications like background gas analysis and in neutral-beam detectors (fig. 40).

One aspect of the filter needs special mention: they are not optimal for coincidence experiments, since there is a considerable spread in ion transit times. This time depends on the phase of the RF field at the moment the ion enters the field, and on the entrance angle.

For more detail on quadrupole analysers we refer to the review by Blauth (1968).

4.5. Time-of-flight analysers

Time-of-flight (TOF) analysis of particle velocities or energies requires that the particles be created at a sharply defined moment in time, after which dispersion of the velocities takes place in a field-free drift region between particle source and detector. Being a pulsed method, TOF analysis can only be performed with a duty cycle considerably smaller than unity; the duty cycle is determined by the time window necessary to record the velocity range of interest. On the other hand, a whole range of velocities is detected simultaneously and this multichannel character usually makes up for the small duty cycle.

Clear advantages over single-channel detection systems are the following. Firstly, relative intensities within one spectrum do not need correction for fluctuations in target gas pressure or photon flux because of the simultaneous data accumulation in all channels. Secondly, detector background counts are randomly distributed over the whole range of channels rather than being accumulated in one channel. A further noise reduction occurs since the product of time window and repetition rate is usually smaller than unity.

If the particle source is excited by synchrotron radiation, with its inherently well-defined pulsed time structure, the TOF analyser may well be worthwhile to consider as an alternative to deflection-type analysers. Very efficient systems can be built since large opening angles are easily realized in the absence of deflection fields. The only problem may be the size and shape of available detectors. One might for instance envisage the design of a 2π-steradian TOF spectrometer, using a large-radius hemispherical channel plate with position-sensitive read-out for complete angular information.

The resolution of TOF devices is determined by:
- the time structure of the exciting pulse;
- the drift length l;
- the spatial extent of the source, i.e., variation in flight path to the detector Δl;
- the timing characteristics of the detector.

The first factor can often be chosen freely within certain limits; when using synchrotron radiation, however, it is fixed by the storage-ring characteristics. For some rings the light-pulse width is slightly less than one nanosecond, while for other rings values of only around 100 ps are quoted. As regards the effect of source size, one must distinguish between two cases. First, the case in which one wishes to analyse initial particle velocities without any preacceleration. This would be the normal mode for, e.g., photoelectron energy analysis. Then one will choose a compromise between intensity and resolution. The energy resolution can then be derived from:

$$\left(\frac{\Delta E}{E}\right) = \left[\left(\frac{2\Delta t}{t}\right)^2 + \left(\frac{2\Delta l}{l}\right)^2\right]^{1/2}, \tag{56}$$

where Δt represents the total time resolution, including the length of the exciting pulse. Second, there is the mode of operation commonly applied for ion mass

analysis. Here the particles are accelerated prior to injection into the drift region, in order to reduce the total TOF and thus the time window. The source-size effect on the resolution can then be minimized by "space focussing". The principle (Wiley and McLaren 1955) is that a particle initially closer to the detector acquires less energy than those further away, and thus may be overtaken by the latter. With a proper choice of accelerating field and drift length, or better still, with two or more separate fields between source and drift region, a large improvement of the space resolution is possible (see e.g., Sanzone 1970). However, another problem remains, namely the decrease of the resolution due to the initial velocities of the ions, in particular of fragment ions that arise in molecular dissociation. For some purposes, one wishes to collect all the ions, regardless of their initial velocity, in as small a time window as possible. Basically this simply requries a large ion draw-out field (Backx et al. 1975). For more stringent requirements, an elegant solution to the "energy-focussing" problem was described by Karataev et al. (1972). They used a folded drift region with reflection of the ions in a retarding field to obtain an excellent energy focus over a wide range of initial energies.

In other ion TOF applications, high mass resolution is not required. One then has the option to apply only a moderate extraction field, which means the information on initial ion velocity is retained in the TOF peak shape. Analysis of peak shapes such as shown in fig. 33 permits determination of the dissociation energy with reasonable accuracy (see, Van Wingerden et al. 1979).

Detector time resolution is currently not a limiting factor; with the advent of the micro-channel plate resolutions of 70 ps have been obtained (White et al. 1979).

We now briefly mention some details of two TOF instruments. A straightforward application of the TOF principle is the device used by White et al. (1979).

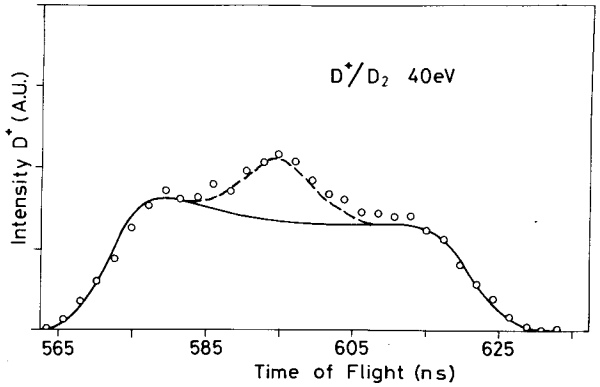

Fig. 33. Time-of-flight spectrum of D^+ ions, formed in dissociative ionization of D_2 by 8 keV electron impact (Van Wingerden et al. 1979). The start signal for the time-to-pulse height conversion is given by electrons, scattered with 40 eV energy loss (to simulate photoionization at $h\nu = 40$ eV). The full curve represents the prediction for D^+ with average energy of 8 eV; the dashed curve D^+ with thermal energy.

They built an electron spectrometer for the 1–50 eV energy range. It has an energy resolution of 5% and angular resolution of ±3°. The spectrometer permits a gain in collection time over conventional spectrometers of around two orders of magnitude.

An interesting device is the double TOF spectrometer (fig. 34) described by Guyon (1979) which is applied for coincidence detection of photoelectrons and photoions. In the photoelectron channel a small draw-out field (1 V/cm) provides a high transmission for essentially zero-energy electrons. Fast electrons are discriminated not only by their small solid angle of acceptance, but further by their TOF difference with respect to the zero-volt electrons. The arrival of a threshold electron is used to trigger a 60 V/cm ion draw-out field, which accelerates the corresponding photoion into a 5 cm drift region. The ion mass resolution is 20, and initial kinetic energies can be obtained from the peak shape with an accuracy of approximately 0.2 eV.

Further applications of the TOF principle have been described by numerous authors. We mention here Land and Raith (1973), Toburen and Wilson (1975), Backx et al. (1975a), Kennerly (1977) and Littlefield and Harmon (1978).

A special feature of the TOF analyser is that it permits coincidence detection of two particles of the same kind having different velocities. For instance, such an autocorrelation measurement of different-mass ions arising from one double-ionization event was described by Backx and Van der Wiel (1975).

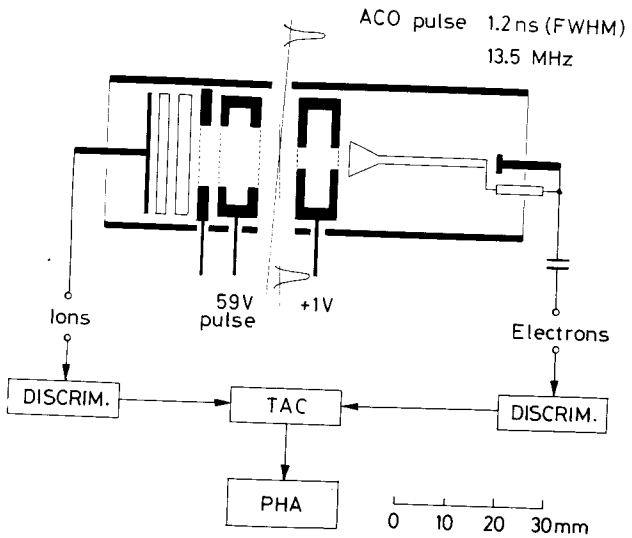

Fig. 34. Double time-of-flight spectrometer for coincidence detection of photoelectrons and photoions (Guyon 1979). Photoelectrons of near-zero energy are efficiently extracted by the +1 V voltage. Arrival of the photoelectron is used to trigger the −59 V pulsed ion extraction field. Dimensions are chosen such that space-focussing of the ions is ensured.

4.6. Multichannel detection

In synchrotron radiation experiments many parameters can be and in most cases are studied. In for instance experiments on photoemission from a target, illuminated by a light beam with photon energy $h\nu$, electrons are produced with a certain energy (E) and angular distribution (expressed in terms of the polar and azimuthal coordinates θ and ϕ, respectively). If one wants to investigate the photoemission probability as a function of E, θ, ϕ, $h\nu$, photon polarization (i.e., linearly or circularly polarized light) and possibly the orientation of the photon beam with respect to the surface, it is clear that this can be very time consuming, especially if the analysing system is capable of looking at only one particular combination of the parameters at a time. This may give rise to serious problems such as (surface) contamination or damage of the target during illumination. For that reason nowadays more and more attention is paid to parallel or multichannel detection techniques. Multichannel detection can be performed either in the time or in the position domain. An example of the first possibility is the technique of time-of-flight analysis (sect. 4.5). The present section deals with the requirements, which analysers must satisfy in order to be used in conjunction with position-sensitive detectors. Details of the read-out techniques for micro-channel plates, the most commonly used device for multichannel detection, are given in sect. 5.3 together with applications.

Three of the above mentioned parameters, E, θ and ϕ, can be spatially resolved such that there exists a known one-to-one relation between the parameter and a position on the position-sensitive detector; therefore these parameters are suitable for multichannel detection. In case two-dimensional detectors are used, it is in principle possible to perform multichannel analysis on two parameters simultaneously. We now give some general remarks and treat a few typical examples:

Multichannel energy analysis: The "ideal" energy analyser used for multichannel detection of a complete energy spectrum has the following features:

– Particles with different energies are imaged on a plane.

– This image plane is an equipotential plane. This latter property is important because the front surface of the channel plate is an equipotential plane. The only analyser which combines both features is the parallel plate analyser: see fig. 35(a) and sect. 4.2.3. In the 45° version the image plane coincides with the bottom electrode; the 30° versions have an image plane below the bottom electrode (Proca and Green 1970). Because the parallel plate analyser has one-dimensional focussing the non-dispersive dimension can in principle be used to obtain information on the (θ) angular distribution. This holds for all one-dimensionally focussing analysers. An example of a 45° parallel plate analyser in which energy and angular distributions are simultaneously determined is given by Pauty et al. (1974). However, in this case no channel plate was used at the bottom electrode but the electrons passing the exit grid (fig. 35(a)) were imaged on an electron-sensitive photographic plate. An ideal analyser for simultaneous detection of the parameters E and ϕ is the 45° fountain parallel plate analyser (fig. 21). However the channel plate has to be large and ring shaped.

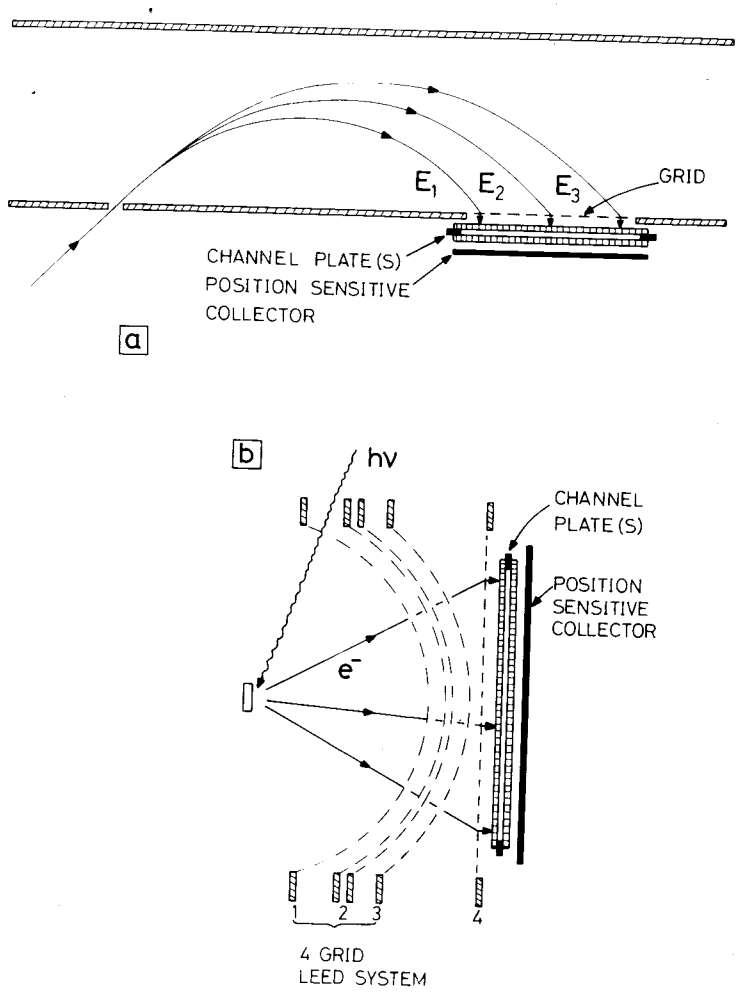

Fig. 35. Examples of multichannel detection arrangements in which micro-channel plates are used. (a) Parallel plate analyser. The curved trajectories represent particles with energies E_1, E_2 and E_3. The grid serves to separate the deflecting field between the plates and the (usually) accelerating field between the grid and the channel plate. (b) Spherical four-grid retarding potential analyser for multichannel detection of angles of emission. The grid in front of the channel plate (4) serves to separate the accelerating field in front of the channel plate from the rest of the analyser.

The 180° hemispherical and 127° cylindrical deflection analysers have also well-defined image planes; however, these coincide with the exit planes and thus are not equipotential planes. The presence of the channel plate at the exit plane spoils the potential distribution of the analyser. This may lead to aberrations in the image, especially for energies focussed at radii much different from the central one, R_0; see figs. 25 and 26. A solution to this problem is to use a lens system to image the exit plane of the analyser on the channel plate which is now placed in

the field-free region of the last lens element. The characteristic dimension D of the lens system has to be chosen such that the (spherical) aberrations are sufficiently small. If the range of energies to be imaged on the detector is large, chromatic aberrations may cause serious problems (sect. 3.4). An alternative solution is to use sector fields shorter than 180° and 127°, respectively. The image plane then no longer coincides with the exit plane; see, e.g., fig. 23.

In a cylindrical mirror analyser particles with different energies are imaged in the field-free region in the inner cylinder (fig. 22). The image surface is a cone with the apex pointing away from the entrance slit. Wannberg (1973) showed that if the outer cylinder is replaced by a surface of the type $R_2 = R_1 \exp(1 + Az)^{-1}$ the image surface coincides approximately with the inner cylinder over an energy range of about 20% of the central energy (z is the axial coordinate and A a suitably chosen constant). Although in principle a set of ring-shaped electrodes located at the inner cylinder can be used for multichannel detection, the overall set-up does not look very promising.

Smeenk et al. (1982) apply a toroidal deflecting analyser for simultaneous detection of energy in the dispersive plane and angle (only θ) in the non-dispersive plane.

In case of magnetic sector fields the image surface generally is curved (Sevier 1972), however, a suitably chosen field geometry can lead to an image plane. Fadley et al. (1972) showed that a $\pi\sqrt{2}$ iron-free instrument an energy interval of 10–20% of the central energy can be analysed simultaneously.

Multichannel angle analysis: The most obvious choice for angle resolved analysis with simultaneous detection of θ and ϕ is the spherical grid retarding potential analyser (sect. 4.3 and figs. 30(d) and 35(b)). Such a system is described by Weeks et al. (1979). As was discussed in sect. 4.3 the disadvantage of this set-up is its high-pass character. A very elegant solution to this problem is given by Eastman et al. (1980) who applied two retarding potentials in series, one in reflection (mirror) and one in transmission; i.e., a combination of a low- and a high-pass filter. The shape of the retarding fields is chosen such that the angular information is retained.

Deflection type analysers with azimuthal symmetry are suitable for multi-channel detection of the angle ϕ, i.e.: the cylindrical mirror analyser, the fountain analyser and the 2π version of the spherical deflection analyser. In principle a θ range equal to twice the opening angle $\Delta\alpha$ (fig. 22) can be analysed simultaneously. An example of such a system is depicted in fig. 36 (Van Hoof and Van der Wiel 1980): photoelectrons produced at a solid target are energy analysed by means of an $\alpha = 42.3°$ cylindrical mirror analyser. The polar angle selection lens placed between the CMA and the target is excited such that for a particular energy, an angular band $\Delta\theta_S$ around a chosen angle θ_S is focussed into the opening angle accepted by the analyser ($42.3° \pm 6°$). The detector input lens focusses the electrons leaving the CMA on the detector plane. This latter lens improves the ϕ resolution and ensures that the electrons hit the channel plate perpendicularly (which is advantageous for the efficiency; see sect. 5.3). The width of ring-shaped slit defines the θ resolution.

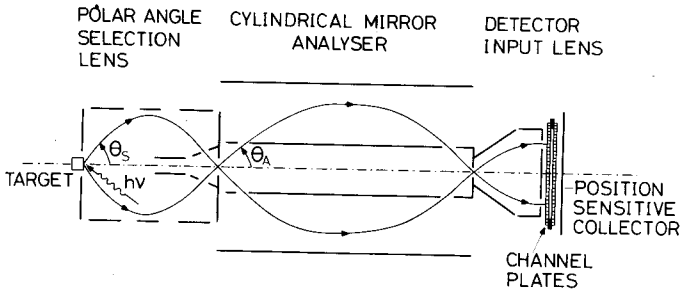

Fig. 36. Cylindrical mirror analyser with entrance and exit optics optimized for multi-channel detection of the azimuthal angle ϕ. For details, see text.

4.7. *Magnetic stray fields*

In a careful design of an energy analyser the influence of magnetic stray fields is taken into account. These stray fields may be due to the earth magnetic field or to the application of magnetic materials such as iron and most types of stainless steel. Especially in the case of transport and analysis of low energy electrons it is essential to shield against these fields. The shielding requirements can be deduced from the following analysis:

In the idealized case of a deflection type analyser in which the particle described a circular orbit in a plane perpendicular to a uniform magnetic stray field B (e.g., cylindrical and spherical deflection analysers; mean radius R_0), this field causes an additional inward (or outward) radial force. This has to be compensated by the analyser electric field such that the particle is able to reach the exit slit. This leads to a shift in the apparent pass energy. For this shift, ΔE_{MAG}, one can derive (Rudd (1972), E expressed in eV):

$$\Delta E_{MAG}/E = (q/2m)^{1/2}\,(BR_0/E^{1/2})\,. \tag{57}$$

For the other types of deflection analysers similar relations can be found.

When the trajectories of different particles inside the analyser do not differ much, i.e., when for instance the opening angle accepted by the analyser is not too large, the magnetic stray field has the same influence on all particles of the same energy. Consequently the effect of a field perpendicular to the dispersive plane is limited to this shift in pass energy; it does not change the energy resolution. This is the case in all deflection type analysers with a well-defined dispersive plane. However, it does not apply to for instance the spherical grid retarding potential analyser (sect. 4.3) and the 2π-CMA (sect. 4.2).

In general, if we allow a maximum deviation d from an ideal particle trajectory with length l, the maximum magnetic field B_m to be tolerated is given by

$$B_m = 2(2m/q)^{1/2}\,(E^{1/2}d/l^2)\,, \tag{58}$$

E is again expressed in eV. If for instance a 180° spherical deflection analyser with

mean radius $R_0 = 5$ cm is applied to analyse 10 eV electrons, a maximum allowed deviation $d = 0.1$ mm leads to $B_m \approx 1$ mG. Under the same conditions the relative pass energy shift is $\Delta E_{MAG}/E \approx 0.05\%$ (eq. (56)).

The shielding of magnetic fields can be achieved in two ways: one can place the analyser at the centre of a system of Helmholtz coils and/or inside a box with high permeability metal walls (mumetal). Helmholtz coil systems can be used to shield the earth magnetic field and other fields which are more or less uniform over the dimensions of the experiment. Such a system is made up of two equal coils at a distance equal to their radius in case of circular coils and at a distance 0.545 times the length of one side in case of square coils (Firester 1966). The latter type of coils usually allows better access to the interior. A complete field annullment systems contains three of those sets of coils along mutually perpendicular axes. Cacak and Craig (1969) calculated that such a system of six circular coils with radii R_H provides a magnetic field homogeneous within 1 and 0.1% in spherical volumes equal to $0.2\,R_H^3$ and $0.03\,R_H^3$, respectively. For further information, see Rudd (1972), Rudd and Craig (1968), Kaminishi and Nawata (1981).

Mumetal single or double shields can reduce magnetic stray fields down to the milligauss level. An excellent review on mumetal shielding is given by Wadey (1956). A few practical remarks are the following:

The number of holes in the shield, such as feed throughs, vacuum pump holes, as well as their size should be kept to a minimum. Also the positions of these holes with respect to each other and the direction of the magnetic field lines should be chosen carefully.

A shielding consisting of two separate layers is more efficient than a single layer with double thickness. From Wadey (1956) the following relations can be deduced for the shielding of a magnetic field B_{out} directed perpendicular to one and two concentric cylinders, respectively:

$$B_{out}/B_{in} = \mu_r d/2R_M\,, \tag{59a}$$

$$B_{out}/B_{in} = \mu_r d/R_M + (\mu_r d/R_M)^2\,(S/2R_M)\,. \tag{59b}$$

In this expression B_{in} stands for the magnetic field strength inside the (inner) cylinder; d is the thickness of each of the cylinder walls; S the distance between the two cylinders; R_M the average radius of the (two) cylinder(s) and μ_r the relative permeability of the mumetal ($\mu_r = 10^4$–10^5). (59 holds under the assumption of infinitely long cylinders and d, $S \ll R_M$; see also Gubser et al. (1979).) The mounting of the two cylinders should be done by means of non-magnetic materials.

When large volumes have to be shielded it should be realized that the shield has to be made sufficiently thick in order to avoid saturation of the mumetal. The thickness d of a mumetal cylinder with radius R_M used to shield a magnetic field $\boldsymbol{B}$ directed perpendicular to the cylinder axis has to be chosen such that the total flux to be shielded, when compressed in the shield, does not saturate, i.e., $d \geqslant R_M B/B_{SAT}$; B_{SAT} is the saturation value of the mumetal (usually $B_{SAT} = 5$–8 kG).

Inside the shield only non-magnetic materials can be used. So-called "non-magnetic" stainless steel is only to be trusted when the absence of remanent magnetism has been checked by means of a (milli)gaussmeter. This needs to be done after each machining process.

4.8. Choice of materials

The choice of materials for the construction of lens systems and analysers is important. Together with the residual magnetic stray fields (sect. 4.7) the materials chosen for slits, apertures, analyser electrodes and grids set a limit on the lowest attainable pass energy. Usually a low pass energy is favourable for the overall properties of the analyser (sect. 4.2.2). The problems one is likely to encounter are the following:

Contact potentials: Different metals connected to each other have a potential difference equal to the difference in work function. Depending on the metals and the condition of the surface (orientation of crystals, contamination) this contact potential can reach values of the order of 0.5 V (Hölzl and Schulte 1979). These variations in potential can be very localized (patch fields) and it is therefore difficult to correct for it.

Oxidation of conductors: This causes local insulating layers. If a fraction of the beam strikes such a layer, it accumulates charge and deflects the beam. This effect usually causes slow fluctuations in signal.

Generation of secondary electrons: Charged particles entering an energy analyser with an energy different from the pass energy impinge on one of the analyser electrodes and create secondary electrons there. Special care should be taken that no secondary electrons are produced at places from where they can be accelerated to the exit slit of the analyser. Note that ions (neutrals) with energies of 100–300 eV can have a secondary emission coefficient larger than unity.

Reflection of particles: Particles with an energy other than the pass energy can reach the exit slit via one or more reflections. Especially low-energy electrons ($<$10 eV) have a large reflection coefficient; see Fowler and Fansworth (1958) and Marmet and Kerwin (1960).

In lens systems the first two points are usually the most important. For not too low energies (say $\geq$25 eV) one can use stainless steel; for lower energies gold plated stainless steel (with additional layers such as, e.g., rhenium to prevent diffusion of the gold into the stainless steel) and in particular molybdenum are good materials. Although there are no objective data on the reflectivity, secondary electron emission coefficient and surface potential uniformity of molybdenum, it is believed to be one of the best (uncoated) materials for slits, apertures and other parts to be used close to the beam.

In analysers with pass energies of the order of 1 eV thin porous coatings of gold black, soot and graphite-based substances like Acheson Colloid Dag 380 are often used to solve the problems mentioned above. Gold black is obtained when gold is evaporated in a 1 mTorr argon atmosphere (Bruining 1938). Soot layers are deposited by holding the surface above oxygen poor butane or benzene flames or

by vacuum deposition. In a comparative study Martin and Von Engel (1977) found soot layers to be superior to other coatings with respect to reflection probability and secondary emission. A disadvantage of these coatings is that they are easily wiped off; therefore they should be handled with care.

Another measure to reduce secondary emission and reflection in analysers is to apply high transmission grids at all places where particles are likely to hit a surface. Additionally these grids can be coated with soot. Behind the grid a plate on a potential sufficiently positive with respect to that of the grid is placed to avoid secondary electrons being produced at places behind the grid (Marmet and Kerwin 1960).

Secondary emission and other spurious effects can also be reduced strongly by applying two analysers in series. In the second analyser only particles with an energy close to the pass energy are present and consequently only a minor fraction of these will impinge on a surface.

Of course all materials used should be compatible with the general vacuum requirements. Information on this matter can be found in vacuum reference books such as Holland et al. (1974). Examples of 180° spherical deflection analysers used in UHV are given by Lindau and Hagström (1971), Thomas and Weinberg (1979) and Allyn et al. (1978). In case oil diffusion pumps are used care should be taken that only oils are selected (Santovac, Convalex) which, when cracked under particle bombardment, do not form electrically insulating layers.

4.9. Calibration

4.9.1. Energy calibration

In principle the absolute energy of a particle transmitted by an analyser should be calculable from analyser dimensions and deflection voltage. In practice, however, problems arise due to deflection-field imperfections at the entrance and exit of the analyser and, more importantly, due to unknown surface potentials and/or patch fields. In most cases at least one point of absolute calibration is therefore needed. As a primary standard for such calibrations one has frequently made use of autoionizing electrons, whose energy is equal to the difference between two ionization thresholds known with optical accuracy.

Having one absolute energy, further calibration of the scale is rather straightforward. For retarding analysers or for deflection-type analysers with constant pass energy and a scanning pre-retardation, all that is needed is a calibrated power supply for the retardation voltage. For analysers in the deflection-voltage scan mode, the factor between (calibrated) deflection voltage and pass energy does not depend on surface potentials and can be found by calculation, or better still, by the use of a second calibration point. Problems with deviations from this linear relationship may arise at very low energies, where the effect of patch fields becomes noticeable.

At the present time there is little need for special efforts to obtain an independent absolute energy scale since quite extensive and reliable listings are available of ejected-electron energies. The energy range of the existing data is

quite wide; roughly speaking, for the range of a few eV to 100 eV, one looks at autoionizing energies (Siegbahn et al. 1969); for 100–1000 eV at Auger-electron energies (Sevier 1972, Davis et al. 1972) and beyond that at X-ray photolines of elements with known ionization energies (Siegbahn et al. 1969).

Note that each of the above-mentioned electron ejection processes can be excited by photon impact, being the most relevant for the present discussion. If the experimental arrangement also allows the presence of an electron source with sufficiently small energy spread, then a wealth of other calibration marks becomes available. In particular, we mention negative-ion resonances, cusps and sharp thresholds both in elastic scattering and in a variety of inelastic channels (see e.g. Schulz (1973)). Most of these secondary standards rely on optically known discrete excitation energies for their accuracy.

4.9.2. Transmission calibration

In sect. 4.2.1 a quantity $C(E)$ was defined, representing the overall collection efficiency of a lens–analyser–detector combination. Obviously $C(E)$ is a function of great practical importance, both with regard to its absolute value and to its relative behaviour with energy.

If one chooses to avoid problems related to the calibration of $C(E)$, one should design a system as follows: Firstly, the source area and solid angle of acceptance are defined entirely by the geometry of a set of collimators in a field-free region. Secondly, the lens system is designed such that it has constant linear magnification and that it passes the entire solid angle at all energies. Finally, an analyser is chosen which again accepts the full solid angle and source area, and has angular

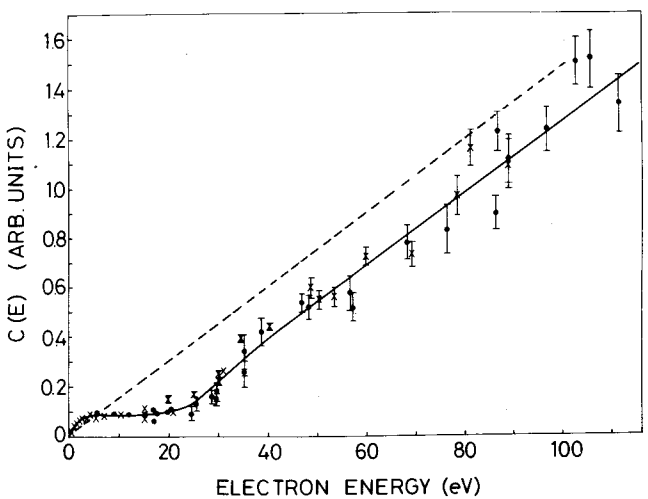

Fig. 37. Collection efficiency of a cylindrical mirror analyser, used in the "constant-relative-resolution" mode, as obtained by Woodruff et al. (1977) from application of eq. (60) (black dots and crosses). The idealized efficiency is represented by the straight dashed line through the origin.

aberration terms in its resolution much smaller than the slit width term; see sect. 4.2.1. Under those conditions, $C(E)$ contains only readily known constants apart from the detector efficiency and the energy band pass of the analyser (we suppose a continuous energy distribution is being analysed). The detector efficiency requires separate calibration (sect. 5.3), while the energy band pass depends on the mode of operation of the analyser. In the "constant-absolute-resolution" mode, i.e., at constant pass energy, the band pass is a constant, even at varying $\Delta\alpha$ and $\Delta\beta$ (since the angular aberration terms are small); in the "constant-relative-resolution" mode the band pass is simply proportional to the pass energy.

This clearly is an idealized case. In practice, one will prefer to optimize the transmission along the lines indicated in sect. 4.2.2. This means that the transmission needs to be derived from a complete ray tracing of the whole system for all energies. Even then, unknown surface charging or difficulties with the ray tracing for unusually shaped optics can lead to unreliable predictions for $C(E)$ (see e.g., fig. 37).

For these reasons, one usually resorts to empirical determination of $C(E)$. Several methods have been described in the literature, of which we briefly indicate the principle. For details we refer to the original publications.

Absolute methods

The most straightforward method (Gardner and Samson 1973, 1975) relies on accurately known photoionization cross sections; compilations of these, claiming ≈3% accuracy over most of the energy range up to a few hundred eV, are presently available (Samson 1966, Marr and West 1976). The idea is to disperse the radiation from a continuum or many-line source, measure the absolute photon flux (see ch. 5 of this book) at a series of wavelengths, and record the yield of photoelectrons from an atomic target gas, preferably at the magic angle (54.4°; see ch. 9 of this book). The factor $C(E)$ is then obtained from

$$N_{el}(E) = \sigma_{ph\,i}(h\nu)nlFC(E) \tag{60}$$

where $E = (h\nu$-ionization potential), n and l are the target gas density and target length respectively and F is the number of photons. This method is an elegant application of synchrotron radiation; however, the range of photoelectron energies that can be produced using a certain monochromator may be different from the range over which the spectrometer needs to be calibrated.

For these cases, another method exists which requires the presence of an electron source, which can be a simple gun without monochromator. The idea is much the same as the previous one, except that now use is made of known electron impact cross sections (e.g., Van der Wiel and Brion (1973)). These can be either differential elastic scattering cross sections, at impact energies equal to those for which the spectrometer needs to be calibrated, or cross sections for production of ejected electrons at high incident energies. For both processes, compilations of reasonable accuracy (5–20%) are now available. For elastic scattering cross sections we refer to the compilations of Register et al. (1979), Andrick

(1973) and De Heer et al. (1979); and for ejected-electron cross sections to the work of Opal et al. (1972).

Relative methods

So far we have dealt with methods which in principle lead to absolute calibration. The problem is simpler if only knowledge of the relative behaviour of $C(E)$ with energy is required. For instance, for calibration over a limited range of 0–10 eV, Gardner and Samson (1976) recommend the use of their tabulated relative-intensity standards. These standards refer to the intensity of a series of spectral features in photoelectron spectra of several gases taken with one-photon energy.

An interesting alternative (Gardner and Samson 1975) is to scan one photoline at different pass energy in the analyser (fig. 38(a)). It can easily be argued that the count rate versus pass energy plot is the inverse of the collection efficiency, assuming that the transmission of the analyser is determined by its geometry, and that the detector efficiency is constant. The argument is a simplification of the earlier description by Poole et al. (1973) of a similar calibration method. An example of the application of the method and a comparison of the result with that of the "cross-section" method are shown in fig. 38.

For completeness' sake, we mention a rather special method, which does not rely on any previously measured quantity. The idea was developed by Van der Wiel and Brion (1973) for a rather special electron scattering arrangement consisting of two electron analysers: a forward-scattering analyser for 3.5 keV electrons, which could be scanned over a wide range of energy losses (but small compared to 3.5 keV) with constant transmission, and a second analyser for low-energy ejected electrons. The two electron signals are measured in coincidence. The calibration of the latter analyser could be performed fully independently by requiring the coincidence count to have the same spectral behaviour as the energy-loss signal under well-defined conditions.

A few concluding remarks concern some pitfalls in the calibration problem. Firstly, when using radiation of narrow linewidth, the definition of the transmission becomes problematic. Our previous definition of $C(E)$ was based on a continuous distribution of energies at the analyser input. Line-shape problems, and the analysis of peak heights and areas, have been dealt with by Woodruff et al. (1977) (see fig. 37).

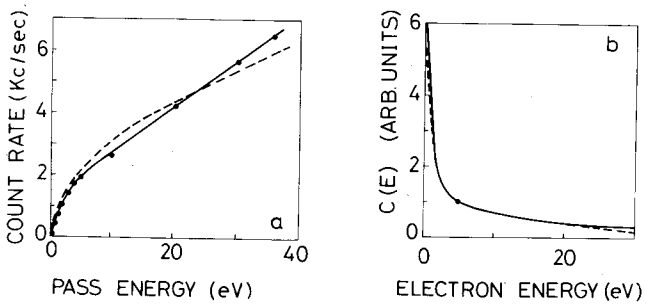

Fig. 38. (a) Intensity of one line in a photoelectron spectrum at different pass energies; dashed curve is expected behaviour (from Gardner and Samson (1975)). (b) Solid curve: inverse of experimental curve in (a), representing the collection efficiency. Dashed curve: efficiency derived from eq. (60) (ibidem).

Secondly, one should be aware of pressure dependence of the calibration, especially since one often tries to enhance the count rates by working at high target pressures. At typical analyser energies of a few eV, the cross section for an electron to be scattered out of its path, is on the order of 10^{-15} cm^2. At pressures around 10^{-1} Pa, the probability for scattering approaches unity. Moreover, resonance structure in the scattering cross section may even complicate the situation further. These and similar problems have been discussed in some detail by Gardner and Samson (1973) and by Wuilleumier et al. (1977).

5. Particle detectors

5.1. Neutral particle detectors

In this section we restrict ourselves to a brief listing of the most commonly used techniques to detect neutral particles at low energy, such as are created, e.g., in photodissociation processes. Results for the detection of faster neutrals (0.5–50 keV) as were reported by Barnett et al. (1972) are outside the scope of this section.

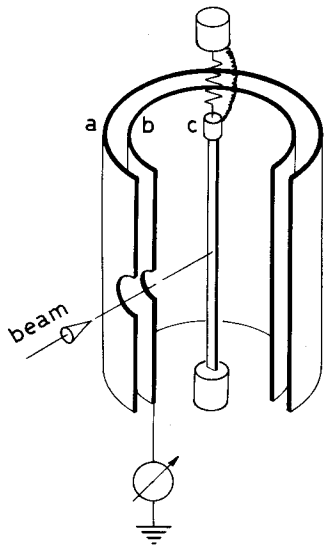

Fig. 39. Hot-wire detector for neutral particle detection (mainly alkalis) by surface ionization. (a) electrostatic screen; (b) ion collector electrode; (c) hot filament (at positive bias voltage). For efficiencies see Datz and Taylor (1954) and Hollstein and Pauly (1966).

Surface ionization

The neutrals that are most readily detected are the alkali atoms. Their ionization energy is low enough to permit surface ionization on surfaces of metals such as W, Re and others, having work functions exceeding the alkali ionization potentials. They make very efficient detectors, which are also of simple design (see fig. 39). For thermal energies and up to several electronvolts efficiencies close to unity have been measured (see caption of fig. 39). One of the few problems with these detectors is their background due to the evaporation of small amounts of contaminant alkali – mostly K – from the bulk material. This requires prolonged outgassing before a measurement.

Electron impact ionization

A universal way to detect neutrals that do not ionize on surfaces, is to ionize them by electron impact. One then measures either the total ion signal or selects different masses with, e.g., a quadrupole filter. The efficiency is low, typically 10^{-5}–10^{-4}, and much effort has been spent on improving this figure. An example of an optimized ionization detector is shown in fig. 40.

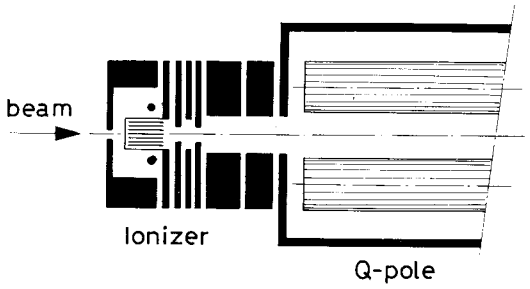

Fig. 40. Universal detector for neutral particle detection by electron impact ionization.* Electrons from the four filaments (only two are shown as black dots) traverse the gridded cage and form a plasma for increased efficiency. For thermal N_2 beams the efficiency is typically 10^{-3}. A quadrupole is used for mass selection of the ions.

Multiphoton ionization

An alternative for the previous method is the use of an intense laser to ionize neutrals. The method is universal as long as high-intensity lasers are used, which ionize by a multiphoton absorption process even without the presence of intermediate resonances. During the laser pulse efficiencies of unity are readily attained, but of course a drawback is the very low duty cycle of these pulsed lasers; at best one has pulses of 10–20 ns at repetition rates of up to 50 Hz. Due to the highly nonlinear character of the interaction, strong focussing is advantageous. Ionization therefore occurs in a small focal volume, on the order of only 0.1 mm^3.

*Design of Extranuclear Labs., Pittsburgh, Penns. 15238, USA.

When the laser wavelength can be tuned to coincide with one or more intermediate resonances, neutral detection with efficiencies of up to several percent becomes feasible on a CW basis. This method is much more specific, since it requires the neutral to have absorption lines in the visible or near-UV range, typically in the range of 350–800 nm. Detection of neutral beams and collision products with this technique was described recently by Feldman et al. (1977). With further development, one may expect to be able to perform analysis of the vibrational and rotational energy distribution of, e.g., dissociation fragments. That would certainly constitute a major advance beyond just the detection of a neutral.

Laser fluorescence

As in the resonant multiphoton technique, efficient laser fluorescence detection is possible only for neutrals having absorption lines in the visible or near UV range. Efficiencies can be unity for strong absorption lines, even though fluorescent photon detection in itself suffers from limited acceptance angles and low photomultiplier quantum yields. The reason is that thermal energy neutrals spend long enough traversing the laser beam to permit the occurrence of a large number of successive absorptions and spontaneous emissions. The limitations of the method will rapidly diminish with the continued development of powerful tunable UV lasers.

Calorimetry

Application of bolometers can up till now only be considered as a viable technique for detection of neutral beams. For detection of small numbers of collision or dissociation products, the sensitivity still is problematic. Recent developments of superconducting devices, however, show great promise for the future (Gallinaro et al. 1978).

Field ionization

The use of field-ionizing tips has been reported to permit sensitive detection of neutrals (Johnston and King 1966, Woods and Fenn 1966, McWane and Oates 1974). The idea is based on the tunnelling of atomic electrons into the tip material due to fields of several volts/Å, which can be obtained around tips of a few hundred Å radius. The ions are accelerated away from the tip into a multiplier. The method requires cryogenic techniques and ultra-high vacuum, plus the expertise to construct proper needles.

Auger emission

For neutrals in a metastable state, detection is very straightforward. The internal energy of the neutral, if high enough, can readily be used to eject an electron from a solid surface. In such an Auger de-excitation process the neutral returns to the ground state and the ejected electron is detected in the normal way.

5.2. Charged particle detectors

Detection of single electrons and ions is usually performed using one of three principles:

- secondary-electron multiplication;
- conversion into light by impact on a scintillator or a fluorescent screen, followed by a photon detector;
- electron–hole multiplication in a surface-barrier material or counting diode.

The first is by far the most widely used principle, and will thus receive most of the attention in this section. The second is rapidly becoming more popular for multichannel detection schemes employing the relatively easy technique of optical read-out (see sect. 5.3). The third is applied rarely, except in cases where high acceleration voltages (>50 keV) are already part of the experimental requirements, e.g., in the spin analyser (sect. 6). For a bakeable detector using a counting diode, see Kirschner and Müller (1976).

Secondary-electron multiplication was applied initially in discrete-dynode structures (fig. 41); the burst of secondary electrons created by the impact of the projectile on the first dynode, is focussed from one dynode to the next and thus gets multiplied. Materials often used are BeCu or AgMg, which have rather high secondary emission coefficients but are also easily contaminated by exposure to air or to hydrocarbon impurities in normal vacuum systems. This is one of the reasons, besides its large volume and often poor timing characteristics, that this type of multiplier has now generally been superseded by the continuous dynode structure. Only for extreme conditions of very high count rates (>10^5 counts/s) they still find application. A particularly suitable type is that shown in fig. 41, a

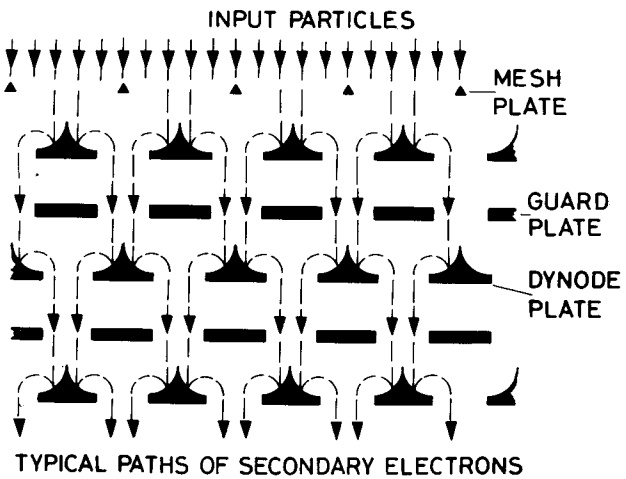

Fig. 41. Schematic of Johnston MM-1 "focussed-mesh" BeCu multiplier. The multiplier features stable gain, due to low secondary emission coefficient per dynode. Time spread between different paths through the system of 21 dynodes is kept within reasonable limits (10 ns) due to focussing action of the cusp-like structures.

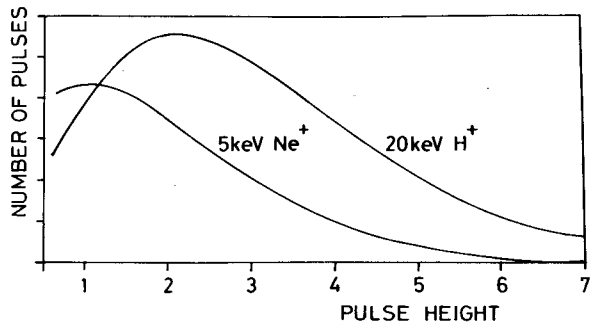

Fig. 42. Pulse-height distribution of Johnston MM-1 multiplier for impact of light ions. The detection efficiency can be judged by estimating the relative area of pulse-heights below the lower thresholds.

multiplier which combines a high count-rate capability with a large sensitive area (5 cm diameter). Figure 42 shows typical pulse-height spectra from which the efficiency can be judged. Absolute efficiencies for ion impact have been reported recently by Peart and Harrison (1981).

The accepted detector for most applications has now become the continuous dynode multiplier; the channel electron multiplier ("channeltron", fig. 43(a)) or the micro-channel plate electron multiplier ("channel plate", fig. 43(b)). They feature small size, ease of operation, high and rather stable gain, narrow pulse width and minimal power requirements.

Channeltrons and channel plates are basically similar devices. Both consist of glass channels coated with resistive material, usually vanadium glass or metallic lead. The end contacts of the channel provide a standing current along the walls which set up a field to accelerate secondary electrons from one impact to the next (fig. 43).

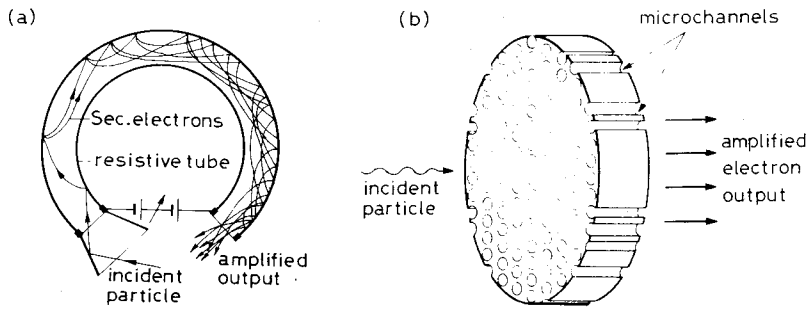

Fig. 43. Continuous dynode multipliers. (a) Channel electron multiplier: channeltron; the entrance funnel is available in several shapes, either circular or rectangular. The inside of the channel is coated with resistive material, which sets up the field necessary for secondary electron multiplication. Curved shape in order to suppress ion feedback. (b) Channel plate electron multiplier: channel plate; array of ~10^5 small channels, each with resistive coating. Often used in cascade of two, with channels at small bias angle, to obtain sufficient gain without ion-feedback problems.

The difference is the length and diameter of the channel: for channeltrons the length is between one and several cm, usually in curved form, at a diameter of one or two mm; the channel plates consist of a closely packed array of thousands of micro-channels, having 0.5–2 mm length and 20–50 μm diameter. The typical channeltron has largely sufficient gain for single-pulse counting: 10^6–10^8. For a single channel plate, the gain is only 10^3 to 10^4, such that a sandwich of two channel plates is usually employed for single-pulse counting.

Towards the output end of a channeltron or of the second of a set of channel plates, the electron density becomes high enough to cause ionization of the background gas. The ions tend to travel in the direction of the input end, where they may strike the surface and start a new avalanche. To suppress this after-pulsing, channeltrons often have curved channels, while channel plates have their channels at a small bias angle with respect to the surface normal, to allow a "chevron" mounting of the two plates.

All secondary-electron multipliers produce output pulses with a certain spread in charge or height. This is due to the statistical nature of the multiplication process. For most applications this is not a problem since the only requirement is that the major fraction of the pulses exceeds a certain discriminator level. However, in position-sensitive detection systems (see sect. 5.3) the charge of a given output pulse from a micro-channel plate is divided up over two amplifiers and a ratio of the two fractions has to be calculated to find the position coordinate. The electronics for this calculation accepts only a wide but limited window of pulse heights. For this application it is therefore advantageous to have a strongly peaked pulse height distribution. This distribution is exponential for non-saturated operation of the channel plate, but can be greatly improved by operating in the saturated mode. This is realized by increasing the gain per plate, in a chevron mounting, to values around 10^4. Then saturation occurs in the second plate and pulse-height distributions as shown in fig. 44 can be obtained.

The small dimensions of the channels result in excellent time response. Pulse widths are of the order of 1 ns, and with constant-fraction discrimination (sect. 7) resolutions of less than 100 ps are feasible. The maximum count rates that can be handled by channeltrons depends on the resistance of the channel coating and on the gain required. The high-resistance (10^{11} Ω) coatings do not permit higher rates than typically 10^4/s, due to charge depletion at the output end. With the lower-resistance type detectors (10^9 Ω) this limit is pushed to 10^6/s, provided sufficient electronic gain is available to get even small pulses to exceed the discriminator threshold.

In channel plates, with their 10^{14} Ω resistance of the individual channels, the charge restoration time after it has been used for amplification, is roughly 1 s. This dictates a limit of the average maximum count rate of $\sim 10^4$/s cm^2. For higher count rates the pulse-height spectrum deteriorates into a count-rate-dependent exponential distribution, resulting in nonlinear response.

Background count rates for channel plates are typically on the order of 1 count/s per cm^2 of plate area. For channeltrons the corresponding number is between 0.1 and 1 count/s. Measurements of the detection efficiency for incident electrons were performed on single-channel multipliers in the range of 1–50 keV.

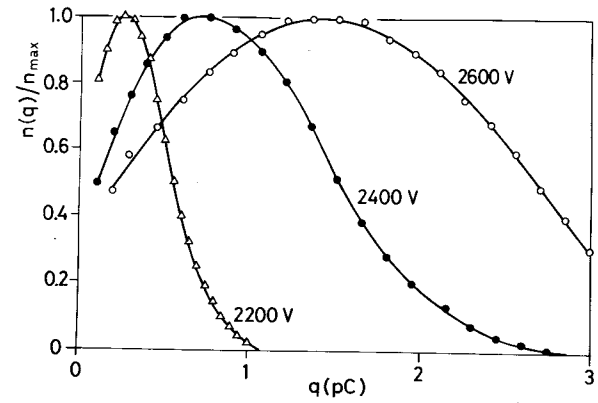

Fig. 44. Pulse-height distribution of cascaded channel plates, for different total voltage across the cascade (Wijnaendts van Resandt et al. 1978). The peak in the distribution is due to saturation of the charge available at the exit of the channel for production of an output pulse.

The results depend upon size of the multiplier funnel used and the angle of the incoming electrons. In the range of 1–50 keV the usefulness of these multipliers for electron detection has been demonstrated; efficiencies vary from approximately 95% at the lower energies to 40% at the higher energies. A typical result of recent measurements for electron impact is shown in fig. 45. One can reasonably assume that similar numbers apply for the channel plate.

As for detection of ions, recent measurements of the channeltron efficiency for hydrogen, argon and xenon ions in the 0.1–4 keV range were reported by Fields et al. (1977). The measurements indicate that ions of varying mass all reach plateau detection efficiencies in the 50% range for energies in excess of 2 keV. In the

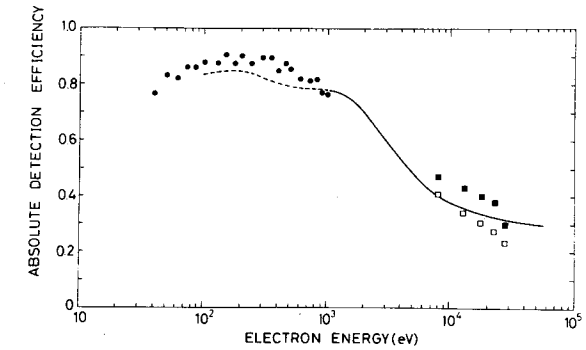

Fig. 45. Detection efficiency of channeltron-type detectors for electrons at different impact energies. Channeltrons: black dots: absolute measurements from Østgaard-Olsen (1979); dashed curve: absolute measurements from Wassmer (1974); solid curve: relative measurements from Archuleta and DeForest (1971), normalized to 0.78 at 1 keV. Channelplates: open and closed squares: absolute measurements from Wijnaendts van Resandt (1980); open squares: electrons impinge on plate at normal incidence (13° with respect to channel surface); closed squares: electrons impinge at an angle of 83.5° with the plate (6.5° with respect to the channel surface).

range below 2 keV, large variations of efficiency with ion mass are encountered. For an energy of 0.5 keV, the detection efficiency is 30% for hydrogen and 40% for xenon.

It should also be noted that the efficiency for detection of neutrals is quite close to that for ions down to energies of a few hundred eV. This has been established, e.g., by Wijnaedts van Resandt et al. (1977).

Efficiencies for photon detection are discussed in ch. 5 of this book.

A recent review of the characteristics of continuous dynode multipliers is that of Leskovar (1978). A special type of continuous dynode multiplier is the parallel-plate multiplier developed by Kanayama et al. (1969) and by Nillson et al. (1972).

5.3. *Position-sensitive detection*

With the advent of the micro-channel plate, position-sensitive particle counters can now be constructed for use in low-energy physics. A number of possible detection schemes is discussed, followed by some applications. We quote extensively from a review of this subject given recently by Wijnaendts van Resandt and Los (1979).

After the amplification by the channel plate the charge cloud initiated by the impinging particle must be registered together with its position. A number of methods exist for the extraction of this information from the detector. These methods can be divided into two groups:

Integrating or analogue methods, where the charge from the channel plates is integrated on some sort of target, for example, the silicon target vidicon.* After accumulation the silicon target is read out by means of a scanning electron beam. Up to now no immediate integration of the charges from the channel plate by the silicon target appears to have been reported. So far there is always a photon step between the channel-plate output and the silicon target. In order words: the channel plate is followed by a scintillator, fiber optics and the silicon target vidicon. This optical step considerably reduces the positional resolution and also introduces a significant background (dark current). An interesting application of this method in the field of mass spectrometry is that of Tuithof et al. (1975). Here a single channel plate is used in conjunction with a vidicon to record a wide range of ion masses in a flash-pyrolysis experiment. Application in an electron spectrometer was reported by Fellner–Feldegg et al. (1974). New developments along these lines are self-scanned diode arrays† and the utilization of charge coupled devices for the combined charge storage and read-out process.

Single event methods. At the moment the technique where each event is registered together with its position seems to have less background and linearity problems. However, these systems are not yet commercially available and require an on-line computer for the digital accumulation of the positional distribution. The

*"OMA" by Princeton Applied Research Corp., Princeton, N.J. 08540, USA.
†"DARSS" by Tractor Northern Inc., Middleton WI 53562. USA.

most simple version of the single event method would be to construct a multi-anode to collect the charges from the channel plates. Then each anode element has to be connected to a preamplifier and followed by a counter. A computer could then read out the counters and construct the positional distribution. However, it has already been mentioned that the maximum count rate of a detector is typically 10 kHz/cm^2 and at this relatively low count rate it is unlikely that more than one anode is active at the same time. Therefore a natural development is a system, which requires less preamplifier/counter systems and which consequently only will work for one particle at the time. Many of such systems have been described in the literature. There are several electronic methods of coding the positional information onto the charge pulse and there is, at the moment, one physical method. An electronic method is the resistive anode (Lampton and Paresce (1974) and Parkes et al. (1974)). For example in the case of a one-dimensional read-out system this consists of a resistance strip, which forms an R–C line. The R–C line has the property that the decay time of the charge pulse depends on the position of excitation of the R–C line (Mathieson et al. 1974). High resolutions (~50 μm) have been obtained with these systems. One channel plate manufacturer delivers the complete assembly of two channel plates and a resistive anode collector.* A disadvantage of the resistance method is that the pulses can become quite broad in time (0.5–5 μs) which makes the system quite sensitive for pulse pile-up, especially at relatively high count rates (≳2 kHz).

Another electronic dissection method is to have a set of discrete anodes, all connected to each other by means of a capacitor. The principle is given in fig. 46 for one- and two-dimensional read-out systems. The major advantages of the capacitance systems are that the anode configuration can be made to fit the spatial application (such as rings, lines, segments, etc.) and that the charge division takes place during the relatively short rise time of the charge pulse (≈10–100 ns). This shorter response time allows the detector to be used at somewhat higher frequencies (≈10–50 kHz).

Owing to the charge spreading between the last channel plate and the collector more than one anode may be excited. A detailed analysis (Gott et al. 1970) has shown that one detects the position of the "center of gravity" of the charge cloud and, in principle, resolutions better than the distance between the anodes can be obtained. It is found that, if the distance between the channel plate and the collector is equal to two times the size of the anode strips the voltage can be adjusted, so that the charge cloud spreads between two to three anodes. In this way the anode structure cannot be seen in the positional distribution.

A system as shown in fig. 46a, containing two 70 mm diameter channel plates, is employed by Novak et al. (1980) in an experiment on photodissociation of molecular ions. Van Hoof and Van der Wiel (1980) use a ring-shaped array of 40 anode segments for simultaneous detection of the azimuthal distribution of photoelectrons transmitted through a CMA (fig. 36).

*Galileo Electro-Optics Corp., Galileo Park, Sturbridge, Ma 01518, USA.

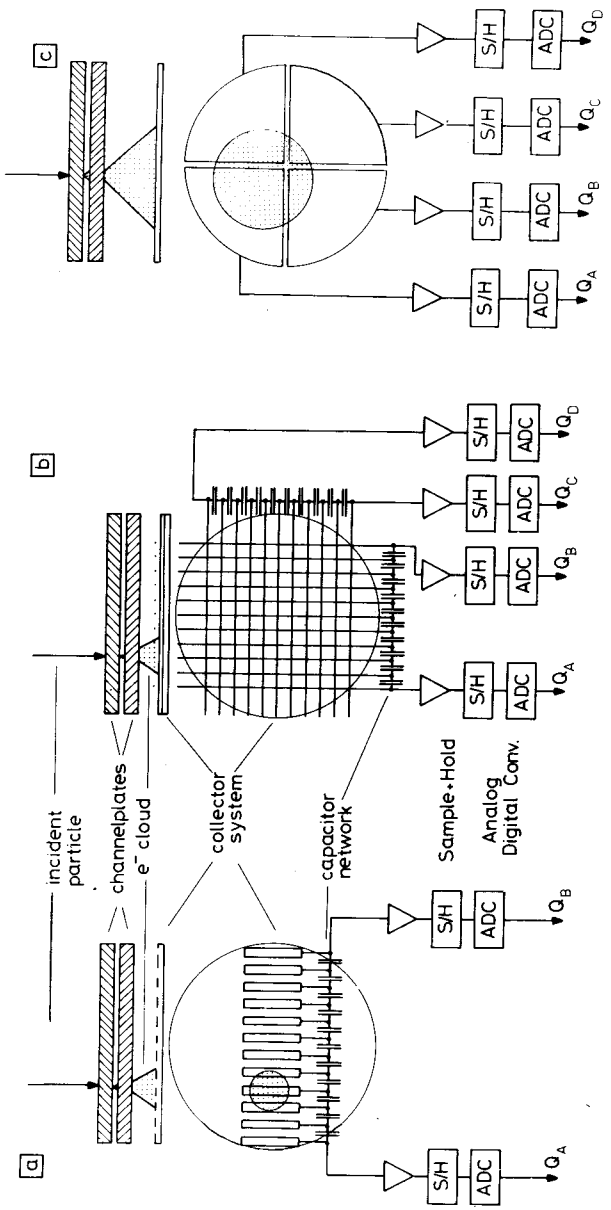

Fig. 46. Position-sensitive detection schemes for single events: (a) multianode strip one-dimensional detector with capacitor string and associated electronics; (b) a multiwire two-dimensional detector; (c) a four-quadrant two-dimensional detector. For each pulse, on-line processing of the numbers $Q_A - Q_D$ is performed by a minicomputer or microprocessor to extract the positional information.

Finally, it is possible to connect the anodes to a delay line as is done for example in multiwire proportional chambers (Gabriel et al. 1978). This method is not yet in general use with channel plates, probably because of the relatively large physical size of the common delay lines with respect to the channel plates. Systems which use delay lines should be especially suited for high count rates.

A physical dissection method which has been developed is the 4-quadrant charge-sharing detector. This detector is schematically depicted in fig. 46(c). The anode is shaped into four quadrants and owing to the relatively large distance between the last channel plate and the 4-quadrant collector the charge from a single event is shared by the four quadrants and the ratio of the charges on each quadrant is a measure for its position. This detector gives two-dimensional information and has a nonlinear response. The advantage of the physical charge sharing is that it is a noise free and potentially fast method. A recent theoretical analysis shows that it is capable of excellent positional resolution (Mathieson 1979).

The principle of fig. 46(c) has been used successfully in a small-angle ion–atom scattering experiment (Wijnaendts van Resandt et al. 1976). In a full angular scattering range of 0.3° a resolution of 0.01° was obtained. For a differential scattering experiment over a wider angular range (1–10°), a multiwire detector according to fig. 46(b) was constructed recently (De Vreugd et al. 1980). The wire array consists of two planes, each made up of 50 Be–Cu wires (0.1 mn thick); the channel plates are 50 mm in diameter.

6. *Spin-polarized electrons*

In many photoionization processes in which circularly polarized light is used the electrons are spin-polarized; i.e., the magnetic moment of the free electron has a preferred orientation in space. Examples of these types of processes are the following:

– Single photon ionization of atoms: Fano (1969), Heinzmann et al. (1970, 1975, 1976, 1979), Cherepkov (1973).

– Multiphoton ionization of atoms: Granneman et al. (1976, 1977) and Teague et al. (1976).

– Photoemission from solids: Alder et al. (1973), Sattler and Siegmann (1972), Siegmann (1975), Pierce et al. (1975) and Reyes and Helman (1977). A feasibility study on spin and energy analysed photoemission is given by Pierce et al. (1979); an actual experiment of this type has been performed by Kisker et al. (1982).

For a general review of the production and properties of spin-polarized electrons, see Kessler (1976).

Because synchrotron radiation is elliptically polarized it has a degree of circular polarization unequal to zero and consequently experiments like the ones mentioned above are possible. However, in this case these experiments are not limited to a few photon wavelengths in the visible part of the spectrum, but they can be done in the continuous spectrum of photon wavelengths available with synchrotron radiation, i.e., ranging from the visible to the X-ray region.

For that reason we will briefly treat the transport of spin-polarized electrons and the measurement of the degree of spin polarization. At the end of this section some attention is paid to spin-polarized atoms.

6.1. Transport of spin-polarized electrons

Before going into details on the transport of spin-polarized electrons we first give a few definitions: The degree of spin polarization P of an ensemble of electrons, defined with respect to a suitably chosen quantization axis, is given by:

$$P = (N\uparrow - N\downarrow)/(N\uparrow + N\downarrow), \tag{61}$$

in which $N\uparrow$ and $N\downarrow$ are the numbers of electrons with "spin-up" and "spin-down", respectively. A beam is longitudinally polarized when the polarization vector is oriented along the direction of propagation of the beam. The polarization is transverse in case it is oriented perpendicular to it. Spin analysers (sect. 6.2) require a transverse polarization along a well-defined axis.

Once the polarized electrons are produced it is important to transport them to the analyser with good control of the spin orientation. During transport it may be necessary to rotate the polarization vector such that it suits the polarization analyser.

The influence of electric and magnetic fields on the orientation of the spin vector is the following (Kessler 1976):

(1) In the nonrelativistic limit electric fields do not change the orientation of the spin in space. However, due to the fact that electric fields change the trajectory of the particles, the orientation of the spin with respect to the trajectory changes. This is illustrated in fig. 47(a). It shows that a 90° spherical (energy) analyser can be used to transfer a transverse spin polarization into a longitudinal one and vice versa. For electron energies of the order of 10 keV and larger relativistic effects become important; the deflection angle required to change transverse polarization into longitudinal now becomes:

$$\Phi = \gamma\pi/2, \quad \text{in which} \quad \gamma = [1-(v/c)^2]^{-1/2}.$$

(2) In a magnetic field the electron moves in a helical orbit with the cylotron frequency ω:

$$\omega = eB/\gamma m. \tag{62}$$

The spin of the electron precesses about the field direction with a frequency ω_p equal to:

$$\omega_p = (g/2)\, eB/\gamma m, \tag{63}$$

in which $g = 2.00232$. Because the difference between ω_p and ω is small, the angle

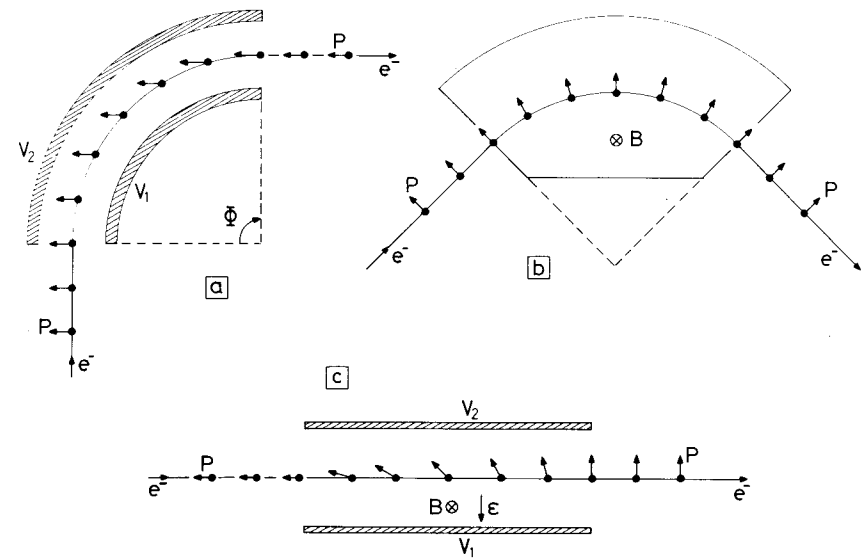

Fig. 47. Behaviour of the electron spin in various electric and magnetic field configurations. (a) A 90° electrostatic deflection field transfers a transverse polarization of a beam into a longitudinal one. (b) In a magnetic deflection field the orientation of the electron spin with respect to the electron trajectory does not change. (c) A Wien filter can also be used to transfer a transverse polarization of a beam into a longitudinal one (and vice versa).

between the velocity vector $\boldsymbol{v}$ and the spin vector $\boldsymbol{P}$ remains unchanged, provided the total number of revolutions is small. This is illustrated in fig. 47(b). Consequently transverse and longitudinal polarizations remain transverse and longitudinal, respectively.

(3) An elegant way to transfer a longitudinal polarization into a transverse one and vice versa is to apply a Wien filter with a length a length $L = \pi v_D/2\omega$; see sect. 4.2.5 and fig. 47(c), and for example Granneman et al. (1976). Of course such a Wien filter can simultaneously be used as an energy analyser; see eq. (26) and table 1.

From the analysis given above it is clear that as far as the control of spin orientation is concerned only magnetic stray fields are potentially dangerous. In case a polarized electron with energy E (expressed in eV) travels a distance l in a stray magnetic field B making an angle ζ with the electron spin vector, this spin vector precesses about $\boldsymbol{B}$ over an angle ξ equal to:

$$\xi = (e/2m)^{1/2}(Bl/E^{1/2})\sin\zeta. \tag{64}$$

From eq. (64) it can be seen that there are several ways to limit this precession: the most obvious one is to reduce the magnetic stray fields by means of Helmholtz coils and/or mumetal shielding. Besides that it is advisable to accelerate the electrons to high energies E in between the source and the detector. In principle a

third possibility is to transfer the polarization into a longitudinal one and to apply a large magnetic field along the electron trajectory; i.e., $\sin\zeta \to 0$. Because these large magnetic fields are likely to produce large stray fields in other parts of the experiment this latter method is usually not applied.

6.2. *Analysis of spin polarization*

It is inherently impossible to split a beam of unpolarized free electrons into two polarized beams with opposite spin polarization by means of macroscopic fields (Kessler 1976). In this respect (free) electrons behave fundamentally different from atoms where such a splitting leading to spin-polarized atoms is possible by for instance an inhomogeneous magnetic field (e.g., the well-known Stern–Gerlach set up). For that reason the determination of the degree of spin polarization of free electrons is inherently difficult. All methods known at the moment rely on spin dependent forces present in some selected scattering processes. When electrons are scattered by heavy atoms it can be shown that under certain conditions the coupling between the spin of the free electron and its angular momentum (LS coupling in the continuum) becomes sufficiently strong to cause an asymmetry in the scattering process for equally large positive and negative scattering angles. The most frequently used spin analyser based on this principle is the so-called Mott detector, named after Mott (1929); see fig. 48.

The electrons to be analysed are accelerated to an energy of the order of 100 keV and directed to a thin gold foil where the scattering takes place. In case the electrons are transversely polarized these spin dependent forces cause a left–right asymmetry in the intensities of scattered electrons in the plane perpendicular to the polarization vector. This asymmetry depends on the so-called Shermann number S (Shermann 1956, Holzwarth and Meister 1964), which characterizes the analysing capabilities of a certain combination of foil material, foil thickness, scattering angle and electron energy. S is defined as the degree of

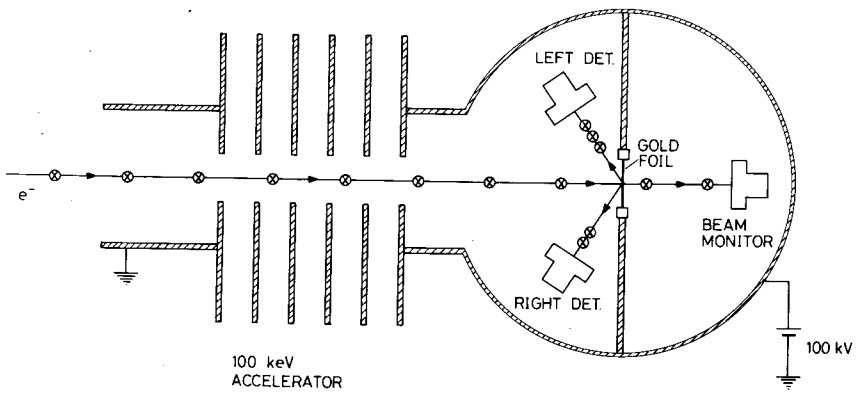

Fig. 48. The most commonly used electron spin analyser: the Mott detector (for details, see text).

spin polarization which is obtained when initially unpolarized electrons are scattered by the foil under the above specified conditions. An electron beam with a degree of spin polarization P leads to an asymmetry in the count rates equal to:

$$N_L/N_R = (1+PS)/(1-PS)\,, \tag{65}$$

in which N_L and N_R are the count rates on the left and right detectors, respectively. Of course, a high value for S is advantageous for the analyser. S increases with electron energy (up to 200 keV); however, the large angle scattering probability decreases with energy. Thicker foils lead to larger scattering intensities I; however, S decreases due to multiple scattering. It can be shown (Kessler 1976) that the optimum situation is obtained when the product S^2I has its maximum value. This leads to a design with the following characteristic parameters: foil: gold with a thickness of 150–250 μgr/cm², usually evaporated on a low Z material (e.g., 40 μgr/cm² Formvar); scattering angle: 100–125°; electron energy 80–120 keV and $S = 0.20$–0.25. It is clear that a Mott detector is a very inefficient type of detector; the efficiencies usually vary between 10^{-3} and 10^{-4}. For the determination of S for a particular experimental arrangement we refer to Van Klinken (1965, 1966) and Kessler (1976).

There are several pitfalls which can make this type of analyser hard to handle. In the first place it is important to use detectors which are able to analyse the electron energy. This means that unwanted electrons entering the detector after one or more collisions with the walls, which in most cases leads to energy loss and certainly to loss of all spin information, can be rejected. For that reason usually silicon surface barrier detectors are applied.

In the second place it is very important to determine which part of the asymmetry is due to the physical process under study and which part to geometrical effects and different detector efficiencies. This can be done in three ways:

(1) The complete set-up of foil and detectors is rotated about the direction of the incoming beam (Van Klinken 1965, 1966).

(2) The polarization of the light is changed in sign. In the visible and soft UV wavelength region this can be done by means of polarizers and quarter wave plates (Heinzmann et al. 1970, Granneman 1976).

(3) The polarization of the electrons is changed from $+P$ into $-P$ by means of a spin rotator such as for instance a Wien filter (fig. 47(c)).

In case experiments with VUV or X-ray photons are done the latter possibility seems the most practical.

An elegant, small size, set-up is described by Hodge et al. (1979). The scattered electrons are decelerated to a few keV and registered by a detector at a potential close to ground. Discrimination against unwanted electrons, which have lost energy is ensured by the retarding potential barrier.

Apart from the 100 keV Mott detectors at present several experiments are being performed to investigate the potentialities of gold and tungsten single crystals as scatterers in low-energy spin polarization analysers. The low-energy

electrons (10–200 eV) are scattered in UHV by the single crystal and produce the well-known LEED patterns. Owing to Mott scattering a transversely polarized electron beam causes an asymmetry in the intensities of equivalent LEED spots left and right of the incoming beam. One of the advantages above high-energy Mott scattering is that the scattered electrons are concentrated at certain preferred angles due to the diffraction condition. This strongly enhances the efficiency of the polarization analyser. Pierce et al. (1977) claim an efficiency of about 10^{-2}. The S-factor is expected to be at least equal in magnitude as those obtained with "normal" Mott detectors (Feder et al. 1977, Kalisvaart et al. 1978, Kirschner and Feder 1979).

It has recently been found that the spin dependence of the secondary-electron yield can be used to determine the degree of spin polarization (Pierce et al. 1981).

6.3. Spin-polarized atoms

A spin-polarized atom is an atom in which the outer electron(s) is(are) spin-polarized. Beams of spin-polarized atoms can be produced by means of inhomogeneous magnetic fields such as present in, for instance, the Stern–Gerlach arrangement. They are also produced when unpolarized atoms interact with circularly polarized radiation tuned in wavelength at one of the resonance transitions of the atom (optical pumping).

As for the transport of these atoms, their electrical neutrality makes it impossible to focus them by means of the usual electrostatic and magnetic lenses. Very weak focussing is possible when atoms are sent through strongly inhomogeneous magnetic fields (e.g., six-pole magnets, Hughes et al. (1972)).

Magnetic stray fields are much more dangerous for spin-polarized atoms than for spin-polarized (free) electrons: the precession frequency of the bound atomic electron is equal to that of the free electron while its velocity is determined by the atomic kinetic energy and thus by the atomic mass; see eq. (64).

Polarized atoms (alkalis) can in principle be detected with efficiency unity. Again Stern–Gerlach types of inhomogeneous magnetic fields are used to select spin-up or spin-down polarization. An example of such an analyser is described by Rubin et al. (1969).

7. Coincidence techniques

7.1. Principles

If two, or more, single-particle detectors observe particles originating from the same interaction center, much more detailed information on the physical process can be obtained, in case their signals contain more than just uncorrelated or random counts. A certain fraction of the counts may be time-correlated since the corresponding particles arose in one interaction event and, having well-defined passage times to their respective detector, arrive with a well-defined time difference.

As an example, consider fig. 49. A photon beam strikes a molecular target AB

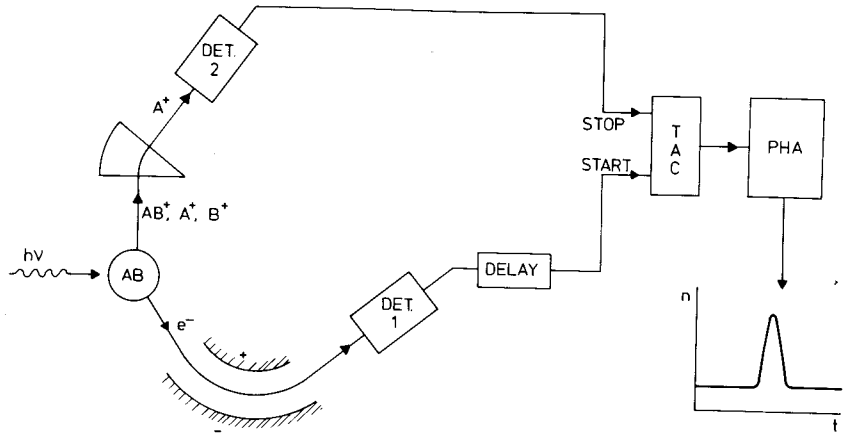

Fig. 49. Example of a photoionization experiment, with coincidence detection of two particles, ions and electrons, using the straightforward time-to-pulse height conversion scheme.

and creates both photoelectrons and photoions. Detector 1 observes a large number of photoelectrons connected with the creation of ions other than A^+, while detector 2 records many ions correlated with other photoelectrons than those having the specific angle and energy seen by 1. However, a fraction of the counts on each detector arises from events $h\nu + AB \rightarrow A^+ + B + e^-$ and therefore exhibit a specific time-correlation. Coincidence detection is the technique to distinguish the number of time-correlated events in signals 1 and 2 from that of the accidental or random "background".

Given two detector signals, how does one arrange a coincidence measurement? The most straightforward method is the application of a time-to-amplitude converter (TAC). This is an analogue device which provides a linear conversion of the time difference between a start pulse and the first-arriving stop pulse (fig. 49) into the height of an output pulse. Those pulses can then be stored conveniently in a pulse-height analyser (PHA), which accumulates a spectrum displaying the time-correlated events or true coincidences on a background of accidental coincidences (fig. 49). It should be mentioned that recently digital alternatives for the TAC have become available with resolutions close to one nanosecond; these provide directly the time-difference between two pulses as the number of periods of an internal clock, and thus the address of the count.

Figure 50 gives more details of the coincidence spectrum. The total width is that of the (adjustable) time-window τ of the TAC, while a delay may be used to compensate unwanted long time differences. The rate of accidental counts in the total window τ is given by $R_{acc} = R_{start} R_{stop} \tau$, where R_{start} and R_{stop} are the count rates on detector 1 and 2, respectively. The accidental counts are randomly distributed over the window. The spectrum of fig. 50(a) with its flat background represents the most common situation, corresponding to all those cases for which the rate of true coincidences $R_{true} \ll R_{start}$ and $R_{stop}\tau \ll 1$.

If these conditions are not satisfied, the spectrum is less simple. Firstly, if the rate of true coincidences is not a small fraction of the start rate, the background

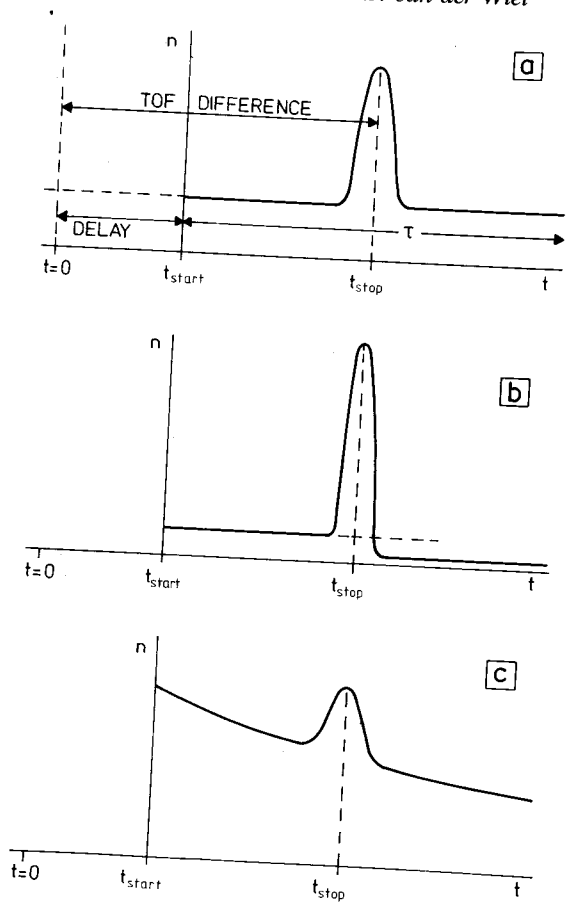

Fig. 50. Different forms of coincidence spectra. $t = 0$ indicates the time of the event in which the two particles are created. A fixed delay is used to adjust the time-window of a time-to-pulse height converter (fig. 49) to the relevant part of the time spectrum: (a) spectrum for low count rates; (b) spectrum for true coincidence rate larger than the total background rate; (c) spectrum for large stop rate (see text).

will show a step across the coincidence peak (fig. 50(b)). The reason is that random counts beyond the peak, or counts on a second peak, are likely to get lost due to a true stop pulse. Secondly, if the probability $R_{stop}\tau$ is not very small, the background has an exponential behaviour (fig. 50(c)); a "late" stop pulse may not be recorded due to the non-negligible integrated probability of all earlier stops. The situation sketched in fig. 50(c) requires that a dead-time correction be made for the height of the true peak, by a factor $\exp[R_{stop}(t_{start} - t_{stop})]$. A detailed treatment of the distorsions of TAC spectra was given recently by Coleman (1979).

It should be noted that, if $R_{start} < R_{stop}$, the dead-time problem can be alleviated by exchanging start and stop signals. Of course this requires changing the delay unit in the new stop channel to a value of about $(t_{start} + \tau)$.

Let us now consider, how is the number of true coincidences obtained and which factors affect its accuracy. A proper fit to the background on either side of the peak, allowing for complications as those of figs. 50(b) and (c), permits interpolation of the background and subtraction from the total count. It is obvious that the statistical accuracy of this measurement depends on the width of the "true" peak. The narrower the peak, the smaller the number of background counts to be subtracted. Factors determining the width, apart from inherent contributions due to lifetimes or initial velocity distribution, are:

- flight-time differences between different points of the interaction center;
- differences in trajectory length in analysers (and lenses);
- electronic jitter.

Since collision centers in practice have dimensions of the order of millimeters, the first factor contributes a spread in time-of-flight ranging from less than one nanosecond for fast electrons to several tens of nanoseconds for electrically extracted ions and up to several microseconds for thermal energy ions. It should be noted that in an extraction field the particle with the longer flight path (i.e., from the far end of the interaction center) gains more extraction velocity and can thus make up for its longer path. Using this principle, "time-focussing" systems can be designed which cancel the time-spread at the detector to first order (see sect. 4.5).

As regards the time-spread in electron analysers, at low pass energy and wide acceptance angle, this factor can easily contribute as much as 10 ns or more. For

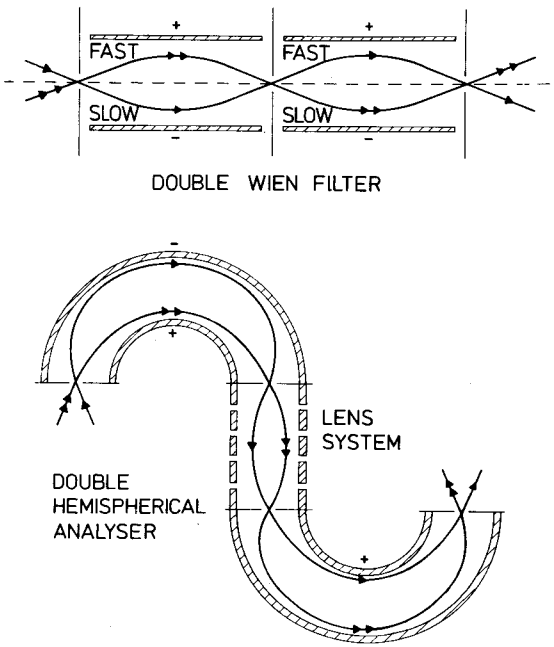

Fig. 51. Examples of double-analyser arrangements in which the time-of-flight spread is cancelled.

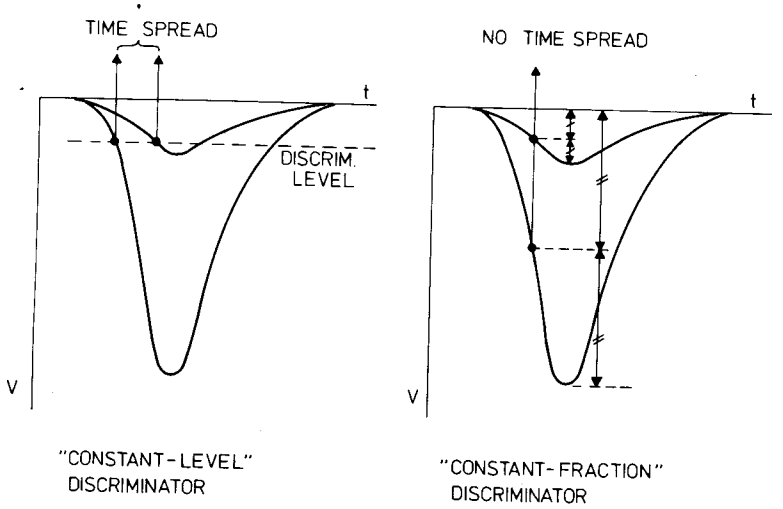

Fig. 52. Two different schemes for discrimination of detector pulses. The "constant-level" scheme introduces a time-spread depending on the pulse-height distribution. In the "constant-fraction" scheme this spread is greatly reduced. The spread cancels completely for pulses of equal shape, independent of their height.

some applications, it may be worthwhile to consider the use of two analysers in series for the purpose of cancelling this time spread. Examples of this principle are given in fig. 51.

Finally, the electronic jitter should be kept to a minimum. The main source is that arising from transit time spread in the detector and from discrimination of detector pulses with a wide range of pulse heights; see fig. 52. The simple "constant-level" discriminator introduces a time jitter of up to the width of the pulse's leading edge. For timing purposes, it is advantageous to use "constant-fraction" discriminators, i.e., timing devices which trigger at a constant fraction of the pulse height. This solves the time-spread problem to the extent to which all pulses have equal shape and a pulse maximum with a fixed time relation to the particle impact time. Time spreads of the order of nanoseconds are possible with channeltron multipliers, while for channel plates resolutions of less than 100 ps have been reported (White et al. 1979).

With these precautions, overall time-resolutions of a few nanoseconds (Cvejanovic and Read 1974, Guyon 1979) and subnanoseconds (Hink et al. 1980) have been obtained in coincidence experiments.

7.2. Data storage

In various applications, the TOF spectrum contains details of relevance for further analysis, e.g., if several peaks occur or if the shape of the true coincidence peak is representative for a lifetime of the process, or for the distribution over initial particle velocities. For those cases, one chooses to store complete TOF spectra for different settings of some experimental variable, and to perform data manipulation afterwards. Obviously, this requires a large amount of memory space. However, it frequently happens that, once the proper shape and narrow width of a true-coincidence peak have been established, one is no longer interested in its shape. All that is relevent then is the number of true coincidences as a function of some experimental variable such as photon energy, and preferably in repetitive scans of that variable. For such cases, a simple hardware solution to the data-storage problem exists (fig. 53). Two single-channel analysers (SCA) reduce the TAC output to two numbers; one SCA selects counts ($n'_{\text{true}} + n_{\text{acc}}$) in a window around t_{stop}, while the second passes an appropriate portion (n'_{acc}) of the background counts. Data accumulation is now reduced to the storage of two numbers per setting of the experimental variable. When using an "up-down" counter, to perform the subtraction ($n_{\text{true}} + n_{\text{acc}} - n'_{\text{acc}}$), one has only one number to store. However, this goes at the expense of the information on the statistical accuracy of the number n_{true} (see sect. 7.3).

When storing the two numbers, one can even adjust the window on SCA 2 to be wider than that of SCA 1, in order to equalize the accuracy of the two numbers. One of the difficulties one may encounter when using the system of fig. 53 is how to calibrate the relative widths of the two SCA's and how to avoid drifts of the width. This problem is particularly serious for cases with small true rates on a large background, the true rate then being the small difference of two large numbers.

To solve this problem, a different approach exists, which is that of using a circuit with fast "and"-gates. These are units which produce one output pulse if two pulses arrive at the two inputs simultaneously. The requirement for simultaneity is that either the two leading edges coincide within an (adjustable) time interval, or that the two pulses overlap in time for at least a minimum time width. The latter system is the most common, and for that type of circuit the time resolution is adjustable simply by varying the pulse width in one of the input channels.

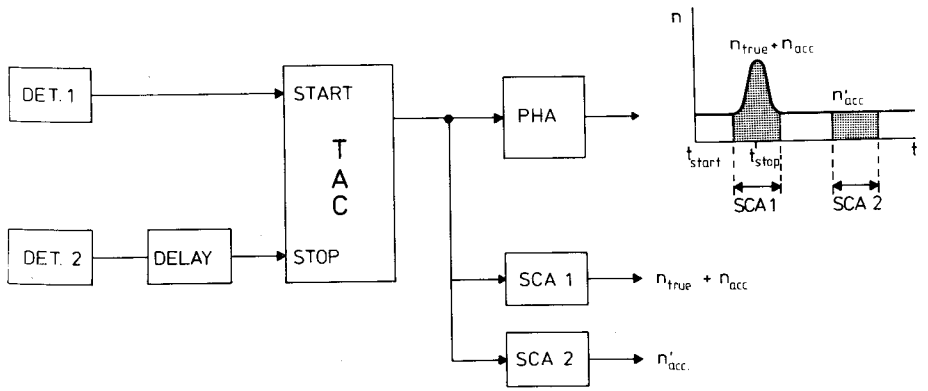

Fig. 53. Coincidence data handling system which requires storage of only two numbers, instead of a full coincidence spectrum, per setting of an experimental variable.

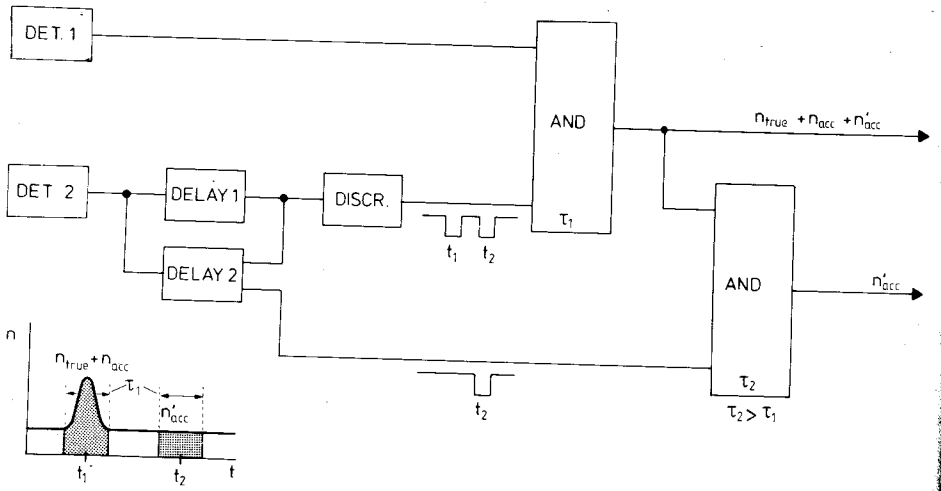

Fig. 54. Equivalent of system of fig. 53, using fast "and"-gates (see text for description).

The and-gate equivalent of the single-channel analyser circuit of fig. 53 is shown in fig. 54. The proper settings of the two delays can be established by scanning delay 1 (with delay 2 removed) to obtain a spectrum like those of fig. 50 at the upper output. The set-up works as follows: The output of the upper and-gate produces the sum of $(n_{true}+n_{acc})$ and n'_{acc}, where each number has been determined with exactly the same time resolution, since the pulses corresponding to the two delay positions passed through the same discriminator* and and-gate. The lower and-gate samples the total number of coincidences and passes only those related to delay position 2. This does not require a precise setting of the time resolution τ_2 of the lower gate; it should only be slightly larger than τ_1.

Again one has a system which requires only two registers to store its output, and to obtain the number of true counts and its statistical accuracy by simple arithmetic. The system completely solves the time-window drift problem and is capable of handling higher count rates than an SCA with its inherent dead-time.

In both systems, however, dead-time corrections become necessary for conditions under which the coincidence spectrum exhibits a measurable slope; see fig. 50(c). The corrections are similar to those given in sect. 7.1. In the SCA system they involve exponentials of the time difference $(t_{stop}-t_{start})$ for correction of the peak height, and exponentials of the time difference between the two windows for correction of the background. In the and-gate system, on the other hand, no correction is needed for the peak counts, while for the background only the window width contributes, as no stop events occur in the time between the two windows.

This is the reason the system of fig. 54 has been used extensively in the high-count-rate experiments of Van der Wiel (1973) and of Brion (1975).

*Care should be taken to avoid rate-dependent width effects for two closely-spaced pulses. Discriminator units with pulse shaping by means of coax cables are free from these effects.

A similar and-gate system for coincidence detection of three signals has been devised and used sucessfully by Backx et al. (1973). Obviously equivalents of such a system using SCA's are conceivable. The scope of this work does not allow a detailed description of these rather complicated circuits.

7.3. Statistical accuracy

In the evaluation of the statistical accuracy of a number of true coincidences, we wish to recognize the influence of various factors:

- the width w of the coincidence peak;
- the total measuring time T;
- a parameter I, on which both detector rates depend linearly, such as photon flux or target-gas pressure or products of the two.

Now the number of true and accidental coincidences can be written as (assuming the inherent detector backgrounds are small):

$$n_{true} = a\,I\,T, \tag{66}$$

$$n_{acc} = b\,w\,I^2\,T, \tag{67}$$

where a and b are constants fully determined by the physics of the process, for a given overall efficiency of the instrumental arrangement (opening angles, and analyser and detector efficiencies). The factor w in eq. (67) represents the linear dependence of the accidental rate on the window required to record the full true peak.

Experimentally n_{true} is obtained as the difference of two uncorrelated numbers: $n_{true}+n_{acc}-n'_{acc}$ for the system of fig. 53, and $n_{true}+n_{acc}+n'_{acc}-2n'_{acc} = n_{true}+n_{acc}-n'_{acc}$ for the system of fig. 54. Therefore we find for the statistical accuracy $\pm(n_{true}+2n_{acc})^{1/2}$ (since $n_{acc}=n'_{acc}$ within the statistical uncertainty) and for its relative value:

$$\Delta n_{true}/n_{true} = \pm(n_{true}+2n_{acc})^{1/2}/n_{true}\,. \tag{68}$$

Substituting eqs. (66) and (67), one easily arrives at:

$$\Delta n_{true}/n_{true} = \pm(1/a)\sqrt{1/T}\,(2bw + a/I)^{1/2}\,. \tag{69}$$

This expression shows the usual dependence on T; it also permits the evaluation of the gain in statistics for a certain reduction in w obtained by instrumental improvements (see sect. 7.2). A rather interesting point is the dependence on I: the relative accuracy improves for increasing I, up to a point where the term $2bw \gg a/I$.

This is contrary to what one would expect on the basis of the commonly used criterion of "peak-to-background" ratio (P/B). Since P/B in a coincidence spectrum like fig. 50(a) would be defined as

$$P/B = n_{true}/n_{acc} = a/bwI, \tag{70}$$

we find that P/B decreases for increasing I. So, paradoxically, a good P/B at low values of I gives worse relative accuracy than a bad P/B at high values of I. It is always advantageous, therefore, to use the maximum possible I, even at the expense of apparent peak-to-background ratio!

The limitations on the parameter I can be of quite varied nature. Practically always one will choose to work at, e.g., the maximum available photon flux and/or the maximum allowable target-gas pressure. However, one of the detectors may saturate or can no longer produce individual pulses for each incident particle. For channeltrons and channel plates saturation rates are between 10^4 and 10^5 counts s^{-1} (per cm^2 for channel plates); for some discrete-anode multipliers saturation is not the problem, but individual detector pulses will begin to merge into one another at very high rates, e.g., at 10^7 counts s^{-1} for 10 ns wide pulses.

Note added in proof

This review was submitted in December 1979, and does not cover articles published later.

Acknowledgements

The authors are indebted to Drs. J.G. Bannenberg and A.J.H. Boerboom and Profs. W. Mehlhorn and F.H. Read for fruitful discussions and useful comments on the manuscript.

This is part of the research program of the Stichting voor Fundamenteel Onderzoek der Materie (Foundation for Fundamental Research on Matter) and was made possible by financial support from the Nederlandse Organisatie voor Zuiver-Wetenschappelijk Onderzoek (Netherlands Organization for the Advancement of Pure Research).

References

Abramowitz, M. and A. Stegun, 1970, Handbook of Mathematical Functions (Dover Publ. Inc., New York).
Adams, A. and F.H. Read, 1972a, J. Phys. E: Sci. Instr. **5**, 150.
Adams, A. and F.H. Read, 1972b, J. Phys. E: Sci. Instr. **5**, 156.
Afanas'ev, V.P. and S.Ya. Yavor, 1975, Zh. Tekh. Fiz. **45**, 1137 [1976, Sov. Phys. Techn. Phys. **20**, 715].
Aksela, S., 1971, Rev. Sci. Instrum. **42**, 810.
Aksela, S., 1972, Rev. Sci. Instrum. **43**, 1350.
Aksela, S., 1973, J. Phys. E: Sci. Instr. **6**, 545.
Aksela, S., M. Karras, M. Pessa and E. Suonnen, 1970, Rev. Sci. Instrum. **41**, 351.
Alder, H., M. Campagna and H.C. Siegmann, 1973, Phys. Rev. **B8**, 2075.
Allyn, C.L., T. Gustafsson and E.W. Plummer, 1978, Rev. Sci. Instrum. **49**, 1197.
Andersen, W.H.J., 1967, Brit. J. Appl. Phys. **18**, 1573.

Andersen, W.H.J. and J.B. Le Poole, 1970, J. Phys. E: Sci. Instr. **3**, 121.
Andrick, D., 1973, Adv. At. Mol. Phys. **9**, eds., D.R. Bates and I. Esterman (Academic Press, New York) p. 207.
Archuleta, R.J. and S.E. DeForest, 1971, Rev. Sci. Instr. **42**, 89–91.
Arnow, M. and D.R. Jones, 1972, Rev. Sci. Instrum. **43**, 72.
Backx, C. and M.J. van der Wiel, 1975, J. Phys. B **8**, 3020.
Backx, C., M. Klewer and M.J. van der Wiel, 1973, Chem. Phys. Lett. **20**, 100.
Backx, C., G.R. Wight, R.R. Tol and M.J. van der Wiel, 1975, J. Phys. B **8**, 3007.
Banford, A.P., 1966, The Transport of Charged Particle Beams (Spon Ltd., London).
Barnett, C.F. and J.A. Ray, 1972, Rev. Sci. Instrum. **43**, 218.
Bederson, B. and L.J. Kieffer, 1971, Rev. Mod. Phys. **43**, 601.
Blauth, E., 1957, Z. Phys. **147**, 288.
Blauth, E.W., 1966, Dynamic Mass Spectrometers (Elsevier, Amsterdam).
Boersch, H., J. Geiger and W. Stickel, 1964, Z. Phys. **180**, 415.
Bosi, G., 1972, Rev. Sci. Instrum. **43**, 475.
Brion, C.E., 1975, Radiad. Res. **64**, 37.
Bruining, H., 1938, Philips Techn. Rev. **3**, 80.
Brunt, J.N.H., F.H. Read and G.C. King, 1977, J. Phys. E: Sci. Instr. **10**, 134.
Cacak, R.K. and J.R. Craig, 1969, Rev. Sci. Instr. **40**, 1468.
Chase, L.M., 1973, Rev. Sci. Instrum. **44**, 998.
Chen, F.F., 1976, An Introduction to Plasma Physics (Plenum Press, New York, London) p. 19.
Cherepkov, N.A., 1973, Zh. Exsp. Theor. Fiz. **65**, 933; 1974, Sov. Phys. JETP **38**, 463.
Chutjian, A., 1974, J. Chem. Phys. **61**, 4279.
Chutjian, A., 1979, Rev. Sci. Instrum. **50**, 347.
Citrin, P.H., R.W. Shaw Jr. and T.D. Thomas, 1972, Electron Spectroscopy, ed., D.A. Shirley (North-Holland, Amsterdam) p. 105.
Coleman, P.G., 1979, J. Phys. E: Sci. Instr. **12**, 590.
Collins, R.E., 1973, J. Vac. Sci. Techn. **10**, 1106.
Conrady, A.E., 1957, Applied Optics and Optical Design (Dover, New York) p. 120.
Cvejanovic, S. and F.H. Read, 1974, J. Phys. B **7**, 1841.
Datz, S. and E.H. Taylor, 1956, J. Chem. Phys. **25**, 389.
Davis, L.E., N.C. MacDonald, P.W. Palmberg, G.E. Riach and R.E. Weber, 1972, Handbook of Auger Electron Spectroscopy (Physical Electronics, Minnesota).
De Heer, F.J., R.H.J. Jansen and W. van der Kaay, 1979, J. Phys. B **12**, 979.
De Jagher, P.C., H.J. Hopman and J.B. Vrijdaghs, 1974, J. Phys. E: Sci. Instr. **7**, 486.
Delage, A. and J.D. Carette, 1971, Can. J. Phys. **49**, 2118.
De Vreugd, C., R.W. Wijnaendts van Resandt and J. Los, 1980, Chem. Phys. **42**, 305.
Di Chio, D., S.V. Natali and C.E. Kuyatt, 1974a, Rev. Sci. Instrum. **45**, 559.
Di Chio, D., S.V. Natali, C.E. Kuyatt and A. Galejs, 1974b, Rev. Sci. Instrum. **45**, 566.
Draper, J.E. and C. Lee, 1977, Rev. Sci. Instrum. **48**, 852.
Duckworth, H.E. and S.N. Ghoshal, 1963, in: Mass Spectroscopy, ed., C.A. McDowell (McGraw-Hill, New York) p. 201.
Eagen, C.F. and E.N. Sickafus, 1977, Rev. Sci. Instrum. **48**, 1269.
Eastman, D.E., J.J. Donelon, N.C. Hien and F.J. Himpsel, 1980, Nucl. Instrum. Methods, **172**, 329.
Edelmann, F. and K. Ulmer, 1965, Z. Angew. Phys. **18**, 308.
El-Kareh, A.B. and M.A. Sturans, 1971a, J. Appl. Phys. **42**, 1870.
El-Kareh, A.B. and M.A. Sturans, 1971b, J. Appl. Phys. **42**, 4902.
Enge, H.A., 1959, Rev. Sci. Instrum. **30**, 248.
Enge, H.A., 1961, Rev. Sci. Instrum. **32**, 662.
Ewald, H. and H. Liebl, 1955, Z. Naturforsch. **10a**, 872.
Fadley, C.S., R.N. Healey, J.M. Hollander and C.E. Miner, 1972, in: Electron Spectroscopy, ed., D.A. Shirley (North-Holland, Amsterdam, London) p. 121.
Fano, U., 1969, Phys. Rev. **178**, 131.
Farmer, J.B., 1963, in: Mass Spectroscopy, ed., C.A. McDowell (McGraw-Hill, New York) p. 7.
Feder, R., N. Müller and D. Wolf, 1977, Z. Phys. B **28**, 265.

Feldman, D.L., R.K. Lengel and R.N. Zare, 1977, Chem. Phys. Lett. **52**, 413.
Fellner-Feldegg, H., U. Gelius, B. Wannberg, A.G. Nillson, E. Basilier and K. Siegbahn, 1974, J. Electr. Spectr. **5**, 643.
Fert, C. and P. Durandeau, 1967, Magnetic Electron Lenses, in: Focusing of Charged Particles I, ed., A. Septier (Academic Press, New York) p. 309.
Fields, S.A., J.L. Burch and W.A. Oran, 1977, Rev. Sci. Instrum. **48**, 1676.
Firester, A.H., 1966, Rev. Sci. Instrum. **37**, 1264.
Fowler, H.A. and H.E. Farnsworth, 1958, Phys. Rev. **111**, 103.
Froitzheim, H. and H. Ibach, 1974, Z. Phys. **269**, 17.
Gabriel, A., F. Dauvergne and G. Rosenbaum, 1978, Nucl. Instr. Methods **152**, 191.
Galeys, A. and C.E. Kuyatt, 1978, J. Vac. Sci. Techn. **15**, 865.
Galeys, A. and P.H. Rose, 1967, Optics in Electrostatic Accelerator Tubes, in: Focusing of Charged Particles II, ed., A. Septier (Academic Press, New York) p. 314.
Gallinaro, G., G. Roba and R. Tatarek, 1978, J. Phys. E: Sci. Instr. **11**, 7.
Gardner, J.L. and J.A.R. Samson, 1973, J. Electron Spectrosc. **2**, 267.
Gardner, J.L. and J.A.R. Samson, 1975, J. Electron Spectrosc. **6**, 53.
Gardner, J.L. and J.A.R. Samson, 1976, J. Electron Spectrosc. **8**, 469.
Gelius, U., E. Basilier, S. Svensson, T. Bergmark and K. Siegbahn, 1973, J. Electron Spectrosc. **2**, 405.
Glaser, W., 1952, Grundlagen der Elektronen Optik (Springer, Berlin).
Glavish, H.F., 1972, Nucl. Instr. Methods **99**, 109.
Golden, D.E., N.G. Koepnick and L. Fornari, 1972, Rev. Sci. Instrum. **43**, 1249.
Goto, K. and K. Ishikawa, 1972, Rev. Sci. Instrum. **43**, 427.
Gott, R., W. Parkes and K.A. Pounds, 1970, IEEE Trans. Nucl. Sci. **17**, 367.
Granneman, E.H.A., 1976, Thesis, Amsterdam.
Granneman, E.H.A., M. Klewer and M.J. van der Wiel, 1976, J. Phys B: Atom. Molec. Phys. **9**, 2819.
Granneman, E.H.A., M. Klewer, G. Nienhuis and M.J. van der Wiel, 1977, J. Phys. B: Atom. Molec. Phys. **10**, 1625.
Green, T.S. and G.A. Proca, 1970, Rev. Sci. Instrum. **41**, 1409.
Grivet, P., 1965, Electron Optics (Pergamon, London).
Gubser, D.U., S.A. Wolf and J.E. Cox, 1979, Rev. Sci. Instrum. **50**, 751.
Guyon, P.-M., 1979, The Physics of Electronic and Atomic Collisions, eds., N. Oda and K. Takayanagi (North-Holland, Amsterdam).
Hanszen, K.J. and R. Lauer, 1967, Electrostatic Lenses, in: Focusing of Charged Particles I, ed., A. Septier (Academic Press, New York) p. 251.
Harris, F.M., P.J. Bassett and M. Prutton, 1975, J. Phys. E: Sci. Instr. **8**, 11.
Harris, L.A., 1974, J. Vac. Sci. Techn. **11**, 23.
Harrower, G.A., 1955, Rev. Sci. Instrum. **26**, 850.
Harting, E. and F.H. Read, 1976, Electrostatic Lenses (Elsevier, Amsterdam).
Hawkes, P.W., 1967, Lens Aberrations, in: Focusing of Charged Particles I, ed., A. Septier (Academic Press, New York) p. 411.
Hawkes, P.W., 1970, Quadrupoles in Electron Lens Design (Academic Press, New York).
Heddle, D.W.O., 1971a, J. Phys. E: Sci. Instr. **4**, 981.
Heddle, D.W.O., 1971b, J. Phys. E: Sci. Instr. **4**, 589.
Heinzmann, U., J. Kessler and J. Lorenz, 1970, Z. Phys. **240**, 42.
Heinzmann, U., H. Heuer and J. Kessler, 1975, Phys. Rev. Lett. **34**, 441.
Heinzmann, U., H. Heuer and J. Kessler, 1976, Phys. Rev. Lett. **36**, 1444.
Heinzmann, U., F. Schäfers, K. Thimm, A. Wolcke and J. Kessler, 1979, XIth Int. Conf. Phys. Electr. At. Coll., Kyoto, Abstr. of Contr. Papers, eds. K. Takayanagi and N. Oda (Soc. At. Coll. Res. Japan) p. 20.
Herzog, R., 1935, Z. Phys. **97**, 596.
Herzog, R., 1940, Z. Phys. **41**, 18.
Hink, J., K. Brunner and A. Wolf, 1980, J. Phys. E: Sci. Instr. **13**, 882.
Hodge, L.A., T.J. Moravec, F.B. Dunning and G.K. Walters, 1979, Rev. Sci. Instrum. **50**, 5.
Holland, L., W. Steckelmacher and J. Yarwood, 1974, Vacuum Manual (Spon, London).

Hollstein, M. and H. Pauly, 1966, Z. Phys. **196**, 364.
Hölzl, J. and F.K. Schulte, 1979, in: Solid Surface Physics (Springer-Verlag, Berlin) p. 86.
Holzwarth, G. and H.J. Meister, 1964, Nucl. Phys. **59**, 56.
Hopman, H.J., B. Jurgens, J.H.A. van Wakeren and H.G. Ficke, 1977, J. Phys. E: Sci. Instr. **10**, 287.
Hughes, A.L. and V. Rojansky, 1929, Phys. Rev. **34**, 284.
Hughes, V.W., R.L. Long, M.S. Lubell, M. Posner and W. Raith, 1972, Phys. Rev. **A5**, 195.
Hutchital, D.A. and J.D. Rigden, 1972a, in: Electron Spectroscopy, ed., D.A. Shirley (North-Holland, Amsterdam) p. 79.
Hutchital, D.A. and J.D. Rigden, 1972b, J. Appl. Phys. **43**, 2291.
Imhof, R.E., A. Adams and G.C. King, 1976, J. Phys. E: Sci. Instr. **9**, 138.
Johnston, W.D. and J.G. King, 1966, Rev. Sci. Instrum. **37**, 475.
Johnstone, A.D., 1972, Rev. Sci. Instrum. **43**, 1030.
Jost, K., 1979, J. Phys. E: Sci. Instr. **12**, 1001.
Kalisvaart, M., M.R. O'Neill, T.W., Riddle, F.B. Dunning and G.K. Walters, 1978, Phys. Rev. **B17**, 1570.
Kaminishi, K. and S. Nawata, 1981, Rev. Sci. Instrum. **52**, 447.
Kanayama, M., T. Konno and S. Kiyono, 1969, Rev. Sci. Instrum. **40**, 129.
Karataev, V.I., B.A. Mamyrin and D.V. Shmikk, 1972, Sov. Phys.-Techn. Phys. **16**, 1177.
Kemeny, P.C., A.D. Lachlan, F.L. Battye, R.T. Poole, R.C.G. Leckey, J. Liesegang and J.G. Jenkin, 1973, Rev. Sci. Instrum. **44**, 1197.
Kennerly, R.E., Rev. Sci. Instrum. **48**, 1682.
Kessler, J., 1976, Polarized Electrons (Springer, Berlin).
Kessler, J. and H. Lindner, 1964, Z. Angew. Phys. **18**, 7.
Kirschner, J. and R. Feder, 1979, Phys. Rev. Lett. **42**, 1008.
Kirschner, J. and N. Müller, 1976, Appl. Phys. **11**, 179.
Kisker, E., R. Clauberg and W. Gudat, 1982, Rev. Sci. Instrum. **53**, 1137.
Klemperer, O., 1953, Electron Optics (Cambridge Univ. Press, London).
Kurepa, M.V., M.D. Tasić and J.M. Kurepa, 1974, J. Phys. E: Sci. Instr. **7**, 940.
Kuyatt, C.E., 1967, Electron Optics Lectures, unpublished.
Kuyatt, C.E., 1968, in: Methods of Experimental Physics, vol. 7A, eds., B. Bederson and W.L. Fite (Academic Press, New York) p. 1.
Kuyatt, C.E., S. Natali and D. Di Chio, 1972, Rev. Sci. Instrum. **43**, 84.
Kuyatt, C.E. and E.W. Plummer, 1972, Rev. Sci. Instrum. **43**, 108.
Kuyatt, C.E. and J.A. Simpson, 1967, Rev. Sci. Instrum. **38**, 103.
Lampton, M. and F. Paresce, 1974, Rev. Sci. Instrum. **45**, 1098.
Land, J.E. and W. Raith, 1973, Phys. Rev. Lett. **30**, 193.
Langendam, P.J.K., 1978, Thesis, University of Amsterdam.
Lee, J.D., 1972, Rev. Sci. Instrum. **43**, 1291.
Lee, J.D., 1973, Rev. Sci. Instrum. **44**, 893.
Leskovar, B., 1978, Workshop on X-ray Instrumentation for Synchr. Rad. Res., SSRL Report 78/04 (Stanford University).
Liebl, H., 1978, Ion Optics for Surface Analysis, in: Proc. Int. Conf. on Low-Energy Ion Beams, eds., K.G. Stephans, I.H. Wilson and J.C. Moruzzi (Inst. Phys. Conf. Series nr. 38, Bristol) p. 266.
Lindau, I. and S.B.M. Hagström, 1971, J. Phys. E: Sci. Instr. **4**, 936.
Lindau, I., J.C. Helmer and J. Uebbing, 1973, Rev. Sci. Instrum. **44**, 265.
Liouville, J., 1838, J. Math. **3**, 349.
Littlefield, R.G. and G.S. Harmon, 1978, Rev. Sci. Instrum. **49**, 1257.
Lucci, A.U., 1970, Nucl. Instr. Methods, **80**, 197.
Marmet, P. and L. Kerwin, 1960, Can. J. Phys. **38**, 787.
Marr, G.V. and J.B. West, 1976, Proc. R. Soc. London. Ser. A, **349**, 397.
Mathieson, E., 1979, J. Phys. E: Sci. Instr. **12**, 183.
Mathieson, E., K.D. Evans, W. Parkes and P.F. Christie, 1974, Nucl. Instr. Methods. **121**, 139.
Martin, N.L.S. and A. Von Engel, 1977, J. Phys. D: Appl. Phys. **10**, 863.
McWane, J.W. and D.E. Oates, 1974, Rev. Sci. Instrum. **45**, 1145.

Mehlhorn, W., 1960, Z. Phys. **160**, 247.
Moore, J.H., M.A. Coplan, T.L. Skillman and E.D. Brooks, 1978, Rev. Sci. Instrum. **49**, 463.
Mott, N.F., 1929, Proc. R. Soc. **A124**, 425.
Mulvey, T. and M.J. Wallington, 1973, Rep. Prog. Phys. **36**, 347.
Natali, S., D. Di Chio, E. Uva and C.E. Kuyatt, 1972, Rev. Sci. Instrum. **43**, 80.
Nillson, Ö., R. Jadrny and K. Siegbahn, 1972, Electron Spectroscopy, ed., D.A. Shirley (North-Holland, Amsterdam, London) p. 141.
Nöller, H.G., H.D. Polaschegg and H. Schillalies, 1974, J. Electron. Spectr. **5**, 705.
Novak, P., H.H. Holsboer, W.P.J. Heubers, R.W. Wijnaendts van Resandt and J. Los, 1980, Int. J. Mass Spectrom. Ion Phys. **34**, 375.
Østgaard-Olsen, J., 1979, J. Phys. E, **12**, 1106.
Opal, C.B., E.C. Beaty and W.K. Peterson, 1972, At. Data **4**, 209.
Palmberg, P.W., 1974, J. Electron Spectrosc. **5**, 591.
Paolini, F.R. and G.C. Theodoridis, 1967, Rev. Sci. Instrum. **38**, 579.
Parkes, W., D.D. Evans and E. Mathieson, 1974, Nucl. Instr. Methods **121**, 151.
Pauty, F., G. Matula and P.J. Vernier, 1974, Rev. Sci. Instrum. **45**, 1203.
Peart, B. and M.F.A. Harrison, 1981, J. Phys. E.: Sci. Instr. **14**, 1374.
Pierce, D.T., F. Meier and P. Zürcher, 1975, Phys. Lett. **51A**, 465.
Pierce, D.T., R.J. Celotta and W.N. Unertl, 1977, Proc. 7th Int. Vac. Congr. and 3rd Int. Conf. Solid Surfaces (eds. and Publ. R. Dobrozemsky, F. Rüdenauer, F.P. Viehböck and A. Breth, Vienna) p. 1297.
Pierce, D.T., C.E. Kuyatt and R.J. Celotta, 1979, Rev. Sci. Instrum. **50**, 1467.
Pierce, D.T., S.M. Girvin, J. Unguris and R.J. Celotta, 1981, Rev. Sci. Instrum. **52**, 1437.
Pierce, J.R., 1949, Theory and Design of Electrons Beams, 2nd ed (Van Nostrand, New York) ch. 9.
Polaschegg, H.D., 1974, Appl. Phys. **4**, 63.
Polaschegg, H.D., 1976, Appl. Phys. **9**, 223.
Poole, R.T., R.C.G. Leckey, J.G. Jenkin and J. Liesegang, 1972, J. Electron Spectrosc. **1**, 371.
Poole, R.T., R.C.G. Leckey, J. Liesegang and J.G. Jenkin, 1973, J. Phys. E **6**, 226.
Poulin, A. and D. Roy, 1978, J. Phys. E: Sci. Instr. **11**, 35.
Proca, G.A. and T.S. Green, 1970, Rev. Sci. Instrum. **41**, 1778.
Proca, G.A. and C. Rüdinger, 1973, Rev. Sci. Instrum. **44**, 1381.
Purcell, E.M., 1938, Phys. Rev. **54**, 818.
Read, F.H., 1969a, J. Phys. E: Sci. Instr. **2**, 165.
Read, F.H., 1969b, J. Phys. E: Sci. Instr. **2**, 679.
Read, F.H., 1970, J. Phys. E: Sci. Instr. **3**, 127.
Read, F.H., A. Adams and J.R. Soto-Montiel, 1970, J. Phys. E: Sci. Instr. **4**, 625.
Regenstreif, E., 1967, Focusing with quadrupole doublets and triplets, in: Focusing of Charged Particles I, ed., A. Septier (Academic Press, New York) p. 353.
Register, D.F., S. Trajmar and S.K. Srivastava, 1979, ICPEAC Book of Abstracts (Kyoto) p. 104.
Renfro, G.M. and H.J. Fischbeck, 1975, Rev. Sci. Instrum. **46**, 620.
Reyes, J. and J.S. Helman, 1977, Phys. Rev. **B10**, 4283.
Risley, J.S., 1972, Rev. Sci. Instrum. **43**, 95.
Roy, D., 1972, Rev. Sci. Instrum. **43**, 535.
Roy, D. and J.D. Carette, 1971a, Can. J. Phys. **49**, 2138.
Roy, D. and J.D. Carette, 1971b, J. Appl. Phys. **42**, 3601.
Roy, D. and J.D. Carette, 1971c, Rev. Sci. Instrum. **42**, 776.
Roy, D. and J.D. Carette, 1977, in: Electron Spectroscopy for Surface Analysis, ed., H. Ibach (Springer, Berlin) p. 13.
Roy, D., A. Delage and J.D. Carette, 1975, J. Phys. E: Sci. Instr. **8**, 109.
Rubin, K., B. Bederson, M. Goldstein and R.E. Collins, 1969, Phys. Rev. **182**, 201.
Rudd, M.E., 1972, in: Low Energy Electron Spectroscopy, ed., K.D. Sevier (Wiley Interscience, New York) p. 17.
Rudd, M.E. and J.R. Craig, 1968, Rev. Sci. Instrum. **39**, 1372.
Samson, J.A.R., 1966, Adv. At. Mol. Phys. Vol. 2 (Academic Press, New York) p. 177.

Sanzone, G., 1970, Rev. Sci. Instrum. **41**, 741.
Sar-El, H.Z., 1967, Rev. Sci. Instrum. **38**, 1210.
Sar-El, H.Z., 1970, Rev. Sci. Instrum. **41**, 561.
Sattler, K. and H.C. Siegmann, 1972, Phys. Rev. Lett. **29**, 1565.
Schmitz, W. and W. Mehlhorn, 1972, J. Phys. E: Sci. Instr. **5**, 64.
Schulz, G.J., 1973, Rev. Mod. Phys. **45**, 378.
Septier, A., 1967, Focusing of Charged Particles I and II (Academic Press, New York).
Sevier, K.D., 1972, Low Energy Electron Spectroscopy (Wiley Interscience, New York).
Sherman, N., 1956, Phys. Rev. **103**, 1601.
Siegbahn, K., 1965, Alpha, Beta and Gamma Ray Spectroscopy (North-Holland, Amsterdam) p. 79.
Siegbahn, K. and co-workers, 1969, ESCA Applied to Free Molecules, North-Holland Publ. Comp. (Amsterdam).
Siegmann, H.C., 1975, Phys. Rep. **17**, 37.
Silbar, R.R., 1970, Nucl. Instr. Methods, **87**, 221.
Simpson, J.A., 1961, Rev. Sci. Instrum. **32**, 1283.
Simpson, J.A., 1964, Rev. Sci. Instrum. **35**, 1698.
Simpson, J.A. and L. Marton, 1961, Rev. Sci. Instrum. **32**, 802.
Smeenk, R.G., R.M. Tromp, H.H. Kersten, A.J.H. Boerboom and F.W. Saris, 1982, Nucl. Instr. Methods, **195**, 581.
Smith, N.V. P.K. Larsen and M.M. Traum, 1977, Rev. Sci. Instrum. **48**, 454.
Staib, P., 1972a, J. Phys. E: Sci. Instr. **5**, 484.
Staib, P., 1972b, Vacuum **22**, 481.
Staib, P. and U. Dinklage, 1977, J. Phys. E: Sci. Instr. **10**, 914.
Stamatovic, A. and G. Schulz, 1970, Rev. Sci. Instrum. **41**, 423.
Steckelmacher, W., 1973, J. Phys. E: Sci. Instr. **6**, 1061.
Steckelmacher, W. and M.W. Lucas, 1979, J. Phys. E: Sci. Instr. **12**, 961.
Tam, W.C. and S.F. Wong, 1979, Rev. Sci. Instrum. **50**, 302.
Taylor, N.J., 1969, Rev. Sci. Instrum. **40**, 792.
Teague, M.R., P. Lambropoulos, D. Goodmanson and D.W. Norcross, 1976, Phys. Rev. **A14**, 1057.
Thomas, G.E. and W.H. Weinberg, 1979, Rev. Sci. Instrum. **50**, 497.
Toburen, L.H. and W.E. Wilson, 1975, Rev. Sci. Instrum. **46**, 851.
Tuithof, H.H., A.J.H. Boerboom and H.L.C. Meuzelaar, 1975, Int. J. Mass Spectrom. Ion Phys. **17**. 299.
Van der Wiel, M.J., 1973, The Physics of Electronic and Atomic Collisions, eds., B.C. Cobić and M.V. Kurepa (Beograd) p. 417.
Van der Wiel, M.J. and C.E. Brion, 1973, J. Electron Spectrosc. **1**, 443.
Van Hoof, H.A. and M.J. Van der Wiel, 1980, J. Phys. E: Sci. Instr. **13**, 409.
Van Klinken, J., 1965, Thesis Groningen.
Van Klinken, J., 1966, Nucl. Phys. **75**, 161.
Van Veen, A., A.G.J. De Wit, G.A. Van de Schootbrugge and J.M. Fluit, 1979, J. Phys. E: Sci. Instr. **12**, 861.
Van Wingerden, B., Ph.E. Van der Leeuw, F.J. De Heer and M.J. Van der Wiel, 1979, J. Phys. B. **12**, 1559.
Vašina, P. and L. Frank, 1979, J. Phys. E: Sci. Instr. **12**, 744.
Wadey, W.G., 1956, Rev. Sci. Instrum. **27**, 910.
Wannberg, B., 1973, Nucl. Instr. Methods, **107**, 549.
Wannberg, B., U. Gelius and K. Siegbahn, 1974, J. Phys. E: Sci. Instr. **7**, 149.
Wannberg, B., G. Engdahl and A. Sköllermo, 1976, J. Electron Spectrosc. **9**, 111.
Wassmer, E., 1974, Zulassungsarbeit Univ. Freiburg.
Weeks, S.P., J.E. Rowe, S.B. Christman and E.E. Chaban, 1979, Rev. Sci. Instrum. **50**, 1249.
Wei, P.S.P., A.Y. Cho and C.W. Caldwell, 1969, Rev. Sci. Instrum. **40**, 1075.
White, M.G., R.A. Rosenberg, G. Gabor, E.D. Poliakoff, G. Thornton, S.H. Southworth and D.A. Shirley, 1979, Rev. Sci. Instrum. **50**, 1268.
Wiley, W.C. and I.H. McLaren, 1955, Rev. Sci. Instrum. **26**, 1150.

Wollnik, H., 1976, Nucl. Instr. Methods, **137**, 169.
Wollnik, H. and H. Ewald, 1965, Nucl. Instr. Methods **36**, 93.
Woodruff, P.R., L. Torop and J.B. West, 1977, J. Electron Spectrosc. **12**. 133.
Woods, R.O. and J.B. Fenn, 1966, Rev. Sci. Instrum. **37**, 917.
Wijnaendts van Resandt, R.W. and J. Los, 1979, The Physics of Electronic and Atomic Collisions, eds., N. Oda and K. Takayanagi (North-Holland, Amsterdam).
Wijnaendts van Resandt, R.W., R.L. Champion and J. Los, 1976, Chem. Phys. **17**, 297.
Wijnaendts van Resandt, R.W., R.L. Champion and J. Los, 1977, Chem. Phys. **20**, 107.
Wuilleumier, F., M.Y. Adam, P. Dhez, N. Sandner, V. Schmidt and W. Mehlhorn, 1977, Phys. Rev. A **16**, 646.
Zashkvara, V.V., M.I. Korsunskii and O.S. Kosmachev, 1966, Zh. Tekh. Fiz. **36**, 132; 1966, Sov. Phys. Techn. Phys. **11**, 96.
Zashkvara, V.V., M.I. Korsunskii, V.P. Lavrov and V.S. Red'kin, 1971, Zh. Tekh. Fiz. **41**, 187; 1971, Sov. Phys. Techn. Phys. **16**, 141.
Zeman, H.D., K. Jost and S. Gilad, 1971, Rev. Sci. Instrum. **42**, 485.

CHAPTER 7

INTERACTION OF RADIATION WITH CONDENSED MATTER

F. BASSANI
Scuola Normale Superiore, I-56100 Pisa, Italy

M. ALTARELLI
Max-Planck-Institut für Festkörperforschung, D-7000 Stuttgart 80, FRG

Contents

Contents continued overleaf

Work supported in part by the Italian CNR through the PULS project of GNSM.

Handbook on Synchrotron Radiation, Vol. 1, edited by E.E. Koch